UNIVERSIDAD DE CHILE
FACULTAD DE CIENCIAS QUÍMICAS Y FARMACÉUTICAS

EFFECTS OF PRECONDITIONED MESENCHYMAL STEM CELLS SECRETOME INTRANASAL ADMINISTRATION ON PERINATAL ASPHYXIA-INDUCED MITOCHONDRIAL DYSFUNCTION AND CELL DEATH IN RAT HIPPOCAMPUS: ROLE OF NRF2 ACTIVATION

TESIS PARA OPTAR AL GRADO DE DOCTOR

MARTA ZAMORANO CATALDO

PROFESOR GUÍA:

PAOLA MORALES R.
MARIO HERRERA-MARSCHITZ
FERNANDO EZQUER

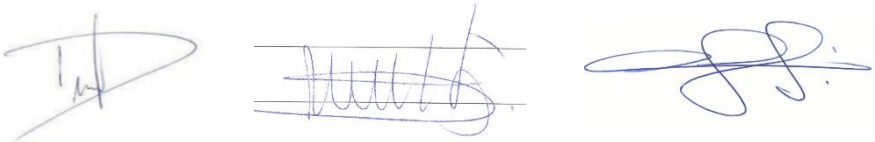

MIEMBROS DE LA COMISIÓN:

PABLO CAVIEDES
SERGIO LAVANDERO
NELSON OSSES

SANTIAGO DE CHILE
2024

ABSTRACT

Perinatal asphyxia (PA) is a severe condition that can lead to long-lasting neurological impairments affecting the surviving newborns. This thesis aims to investigate the effects of PA on mitochondrial dynamics in the rat hippocampus at early (P1) and late (P7) neonatal stages and to explore the potential therapeutic benefits of intranasal mesenchymal stem cell secretome (MSC-S) administration. It is hypothesised that PA increases mitochondrial fission, inducing delayed cell death in the rat hippocampus, and that these alterations can be prevented by neonatal intranasal administration of secretome derived from preconditioned human mesenchymal stem cells via Nrf2 pathway activation.

The study provides evidence for a transient activation of the Nrf2 pathway following MSC-S administration on a rat model of PA. Nevertheless, the precise role of Nrf2 activation in the effect of MSC-S remains to be fully elucidated. PA-induced changes in mitochondrial dynamics proteins, with increased fission proteins Drp1 at P1 and Fis1 at P7, and increased fusion protein S-OPA1 isoform at P1 and L-OPA at P7. Furthermore, PA decreased mitochondrial density and mass by decreasing the D-Loop region expression of mitochondrial DNA at P1 but not at P7. Expansion microscopy analysis revealed decreased mitochondria density in the CA1 and dentate gyrus (DG) regions of PA-exposed animals at P1, with smaller mitochondria in the DG than in CA1. Sex-specific differences were identified in response to PA. Female PA-rats exhibited altered OPA1 expression at P1 and P7, suggesting a potential upregulation of mitochondrial fission at P1 and increased fusion at P7, whose impact on mitochondrial bioenergetics requires further studies.

Treatment with MSC-S derived from preconditioned human MSC normalised fission proteins to control levels, but did not modify the effect of PA on OPA1 levels, either at P1 or at P7, nor on mitochondrial density. These findings contribute to our understanding of the pathophysiology of PA and emphasise the importance of considering sex as a biological variable. Future research should focus on unravelling the molecular mechanisms behind these sex-specific differences.

Index

Figures index

A.1. Abbreviations

PA - *Perinatal Asphyxia*

WHO - *World Health Organization*

HI - *Hypoxic-ischemia*

HIE - *Hypoxic-ischemic encephalopathy*

ROS - *Reactive oxygen species*

RNS - *Reactive nitrogen species*

MOMP - *Mitochondrial outer membrane permeabilisation*

AIF - *Apoptosis-inducing factor*

TCA - *Tricarboxylic acid cycle*

ETC - *Electron transport chain*

OXPHOS - *Oxidative phosphorylation*

ΔΨm - *Mitochondrial membrane potential*

mfn1/2 - *Mitofusins 1 and 2*

OPA1 - *Optical atrophy 1*

Drp1 - *Dynamin-related protein 1*

Mff - *Mitochondrial fission factor*

AMPK - *AMP-activated protein kinase*

PGC-1a - *Peroxisome proliferator-activated receptor γ co-activator 1-a*

TFAM - *Transcription factor A, mitochondrial*

MRI - *Magnetic resonance imaging*

NOS - *Nitric oxide synthase*

NOX - *NADPH oxidase*

SOD - *Superoxide dismutase*

MSCs - *Mesenchymal stem cells*

MSC-S - *Mesenchymal stem cell secretome*

Nrf2 - *Nuclear factor erythroid 2 related factor 2*

ARE - *Antioxidant response element*

Keap1 - *Kelch-like ECH-associated protein 1*

DFX - *Deferoxamine*

ASO - *Antisense oligonucleotide*

TUNEL - *Terminal deoxynucleotidyl transferase dUTP nick end labeling*

qPCR - *Quantitative polymerase chain reaction*

MDA - *Malondialdehyde*

RT-qPCR - *Reverse transcription quantitative PCR*

WB - *Western blot*

IHQ - *Immunohistochemistry*

ExM - *Expansion microscopy*

DAPI - *4',6-diamidino-2-phenylindole*

HRP - *Horseradish peroxidase*

i.c.v. - *Intracerebroventricular*

GSSG/GSH - *Oxidized/reduced glutathione ratio*

CA1 - *Cornu Ammonis area 1*

DG - *Dentate gyrus*

Chapter 1: Introduction

A.2. Perinatal Asphyxia (PA)

PA is an obstetric complication, implying impaired gas exchange, progressive hypoxemia, hypercapnia, and acidosis at the time of delivery [1], it is defined by the World Health Organization (WHO) as "the failure to establish breathing at birth"[2]. The associated signs include an Apgar score of <5 at 5 and 10 minutes, foetal umbilical artery pH <7.0, brain injury seen on brain magnetic resonance imaging (MRI) or MR spectroscopy, consistent with acute hypoxia-ischemia (HI) and presence of multisystem organ failure, consistent with hypoxic-ischemic encephalopathy (HIE) [3], [4]. PA is associated with 30-35% of neonatal deaths and is one of the primary causes of neonatal mortality globally [4], [5].

The causes of PA are varied, and it must consider foetal and maternal factors such as preeclampsia, intrauterine growth restriction, placental abruption, and labour induction or malpresentation [6]. Depending on its severity, PA can generate permanent neurological impairments, including long-term motor, sensory, cognitive, and memory disabilities, affecting around one million infants per year worldwide [7]. The consequences of PA also depend upon the maturity of the brain at the time of the insult. In the 3rd trimester, the most common injury associated with PA affects the white matter. At term, damage of grey matter predominates, affecting basal ganglia, hippocampus, thalamus, and neocortex [8]. The hippocampus is one relevant target, associated with cognitive and memory impairments, recurrently reported following perinatal metabolic insults [9], [10].

A.2.1. Perinatal Asphyxia: Pathophysiology

Interruption of oxygen availability results in decreased oxidative phosphorylation and ATP availability, interrupting the proton gradient and shifting to anaerobic pyruvate-dependent metabolism resulting in lactate accumulation and acidosis [11]. This failure of the ATP-dependent ionic transport by the Na^+/K^+ pumps generates an intracellular accumulation of Na^+, Ca^{+2}, and Cl^- [12], [13]. Intracellular Ca^{+2} accumulation activates lipases, proteases, and endonucleases, inducing cell damage. In addition, interruption of membrane ionic transport increases extracellular glutamate levels, interruption of glutamate clearance by astrocytes and neuronal depolarization and overactivation of extrasynaptic glutamate receptors, increasing calcium conductance. Thus, a severe ionic imbalance leads to cell swelling and subsequent cell death, depending upon the lasting of the oxygen interruption [12], [14] (Fig.1).

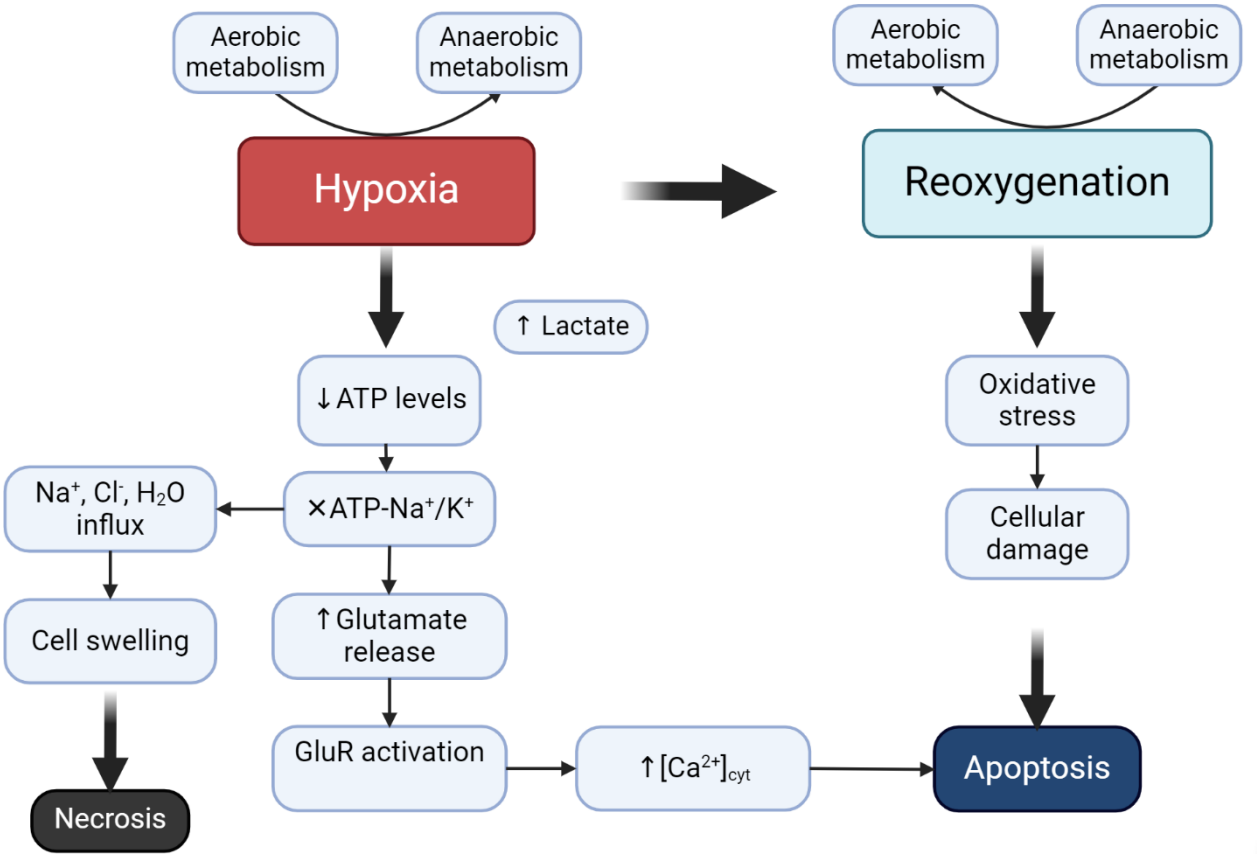

Figure 1: Schematic representation of the effects of hypoxia and reoxygenation. Hypoxia leads to a shift from aerobic to anaerobic metabolism, resulting in decreased ATP levels, increased lactate production, cell swelling, necrosis, and activation of glutamate release and calcium signalling pathways that can ultimately cause apoptosis. Otherwise, reoxygenation enables aerobic metabolism but can also lead to oxidative stress and cellular damage, potentially culminating in apoptosis as well (made in Biorender).

Resuscitation upon reoxygenation induces a secondary energy crisis due to increased oxidative stress, induction of pro-inflammatory cascades, and excitatory amino acid accumulation, resulting in over-activation of AMPA and NMDA receptors, increasing Ca^{+2} conductance and nitric oxide synthase (NOS) activity. Intracellular Ca^{+2} accumulation, mitochondrial swelling, and membrane permeabilisation promote apoptosis, generating a secondary brain injury that can last hours or days [15] (Fig.1). The ability of mitochondria to buffer intracellular calcium in the neonatal brain is not fully developed compared to that in the adult brain [16]. Furthermore, there is a third phase of injury, associated with inflammation and epigenetic modifications, which can last weeks and even years [17].

A.3. Mitochondria in Perinatal Asphyxia

Mitochondria are known for their capacity to produce energy for the cell. Mitochondria also regulate apoptosis, calcium, and cell signalling [18], [19]. In the mitochondrial matrix, the tricarboxylic acid cycle (TCA) generates NADH and FADH2 electron carriers,

donating electrons to the mitochondria electron transport chain (ETC), pumping protons from the matrix into the intermembrane space, increasing membrane potential ($\Delta\Psi m$), generating ATP [20]. Mitochondria also help to maintain membrane potential, protein folding, cell transport, lipids biosynthesis, modulating cytoplasmic calcium concentration, which is essential for neurotransmitter synthesis and release, neurogenesis, neuronal plasticity, and excitotoxicity [20].

During reoxygenation reactive oxygen species (ROS) production rises, increasing oxidative stress. A leakage of superoxide radical ($O_2^{\cdot-}$) from complex I and III activates nNOS, yielding peroxynitrite ($ONOO^-$) [12], altering the ETC, promoting further ROS and RNS formation [17], and NADPH oxidase (NOX) activation. Superoxide dismutase (SOD) catalyses the reaction of $O_2^{\cdot-}$ to form H_2O_2, which is decomposed to water and oxygen by a catalase-mediated reaction. H_2O_2 reacts, in a non-enzymatic reaction with Fe^{2+}, the known Fenton reaction, yielding $^{\cdot}OH^-$, which generates lipid peroxidation, DNA damage, and protein oxidation [16]. The neonatal brain is more vulnerable to oxidative stress than the adult brain, because of its low antioxidant capacity, increased unsaturated fatty acid content, and high free iron levels [8], [17]. Malondialdehyde levels, produced by polyunsaturated fatty acids peroxidation, increase in plasma and cerebrospinal fluid in PA versus non-PA-affected newborns [21]. Human newborns dying of hypoxic-ischaemic encephalopathy, also show high levels of oxidative stress [21]. In neonates, an increase of pro-apoptotic Bax proteins, initiates mitochondrial outer membrane permeabilisation (MOMP), unlike in the adult brain, where the mitochondrial permeability transition pore occurs at the opening of the inner and outer membrane. MOMP formation and increased ROS levels result in cytochrome C, apoptosis-inducing factor (AIF), Smac/Diablo, and endonuclease G release into the cytoplasm, triggering intrinsic apoptotic pathways [8], [12].

A.4. Mitochondrial Dynamics

To respond to energy demands by cellular processes, including cell cycle, immunity, apoptosis, and quality control [16], [22], mitochondria continuously adjust their shape, distribution, and size, undergoing coordinated cycles of GTPases-dependent fission/ fusion events, collectively referred to as 'mitochondrial dynamics' [23].

Mitochondrial fusion refers to the union of two or more mitochondria. Mitochondrial fusion has a buffering role in exchanging matrix content [24]. Indeed, the promotion of mitochondrial fusion has shown to be neuroprotective [25], [26]. Mitofusins 1/2 (Mfn1 and Mfn2) mediate the fusion of the outer mitochondrial membrane (OMM) [27], and protein optical atrophy 1 (OPA1) mediates the fusion of the inner mitochondrial membrane (IMM) [28]. The correct function of OPA1 is modulated by proteolytic cleavage, achieved by the AAA-protease Yme1L and protease OMA1, which generates long (L-OPA1, insoluble) and short (S-OPA1, soluble) OPA1 products as a result of different cellular stimuli

[28], [29]. Under basal conditions, there is an equilibrium between the short and long forms of OPA1 [30]. OPA1 also plays a crucial role in the structure and maintenance of mitochondrial cristae [31].

Mitochondrial fission allows the division of one mitochondrion into two smaller mitochondria, regulated by the recruitment of Dynamin-related protein 1 (Drp1) from cytoplasm to mitochondria surface as a consequence of cellular responses [32]. GTPase activity of Drp1 is inhibited by phosphorylation of Ser 637 via protein kinase A (PKA). Drp1 is phosphorylated at Ser 616 by cdk1, cdk5, PKCγ, and ERK1/2 [33] and de-phosphorylated by calcineurin and protein phosphatase 2A (PP2A). Phosphorylated Drp1 is translocated into the mitochondrion, interacting with adapters like mitochondrial fission factor (Mff) [34], forming a GTP-driven constriction ring around the mitochondrion to perform fission [35]. It was thought that Mammalian Mitochondrial fission 1 protein (Fis1) played a role in encouraging mitochondrial fission, like its yeast counterpart, which recruits Drp1 to mitochondria [30]. However, it has been reported that human Fis1 operates independently of Drp1 and is not crucial for fission [36]. Recent research suggests that Fis1 hinders the activity of fusion GTPases OPA1 and Mfn1/2 [36], implying that blocking fusion alone is enough to induce fragmentation of the mitochondrial network, mimicking fission activation [37] (Fig.2).

The fission-fusion equilibrium is essential for development and neuronal function. OPA1 and Drp1 deficiencies result in genetic defects and lethal malformations [16]. In neurons, fission plays a role in the transport of mitochondria along axons projecting towards areas of high energy demands [38].

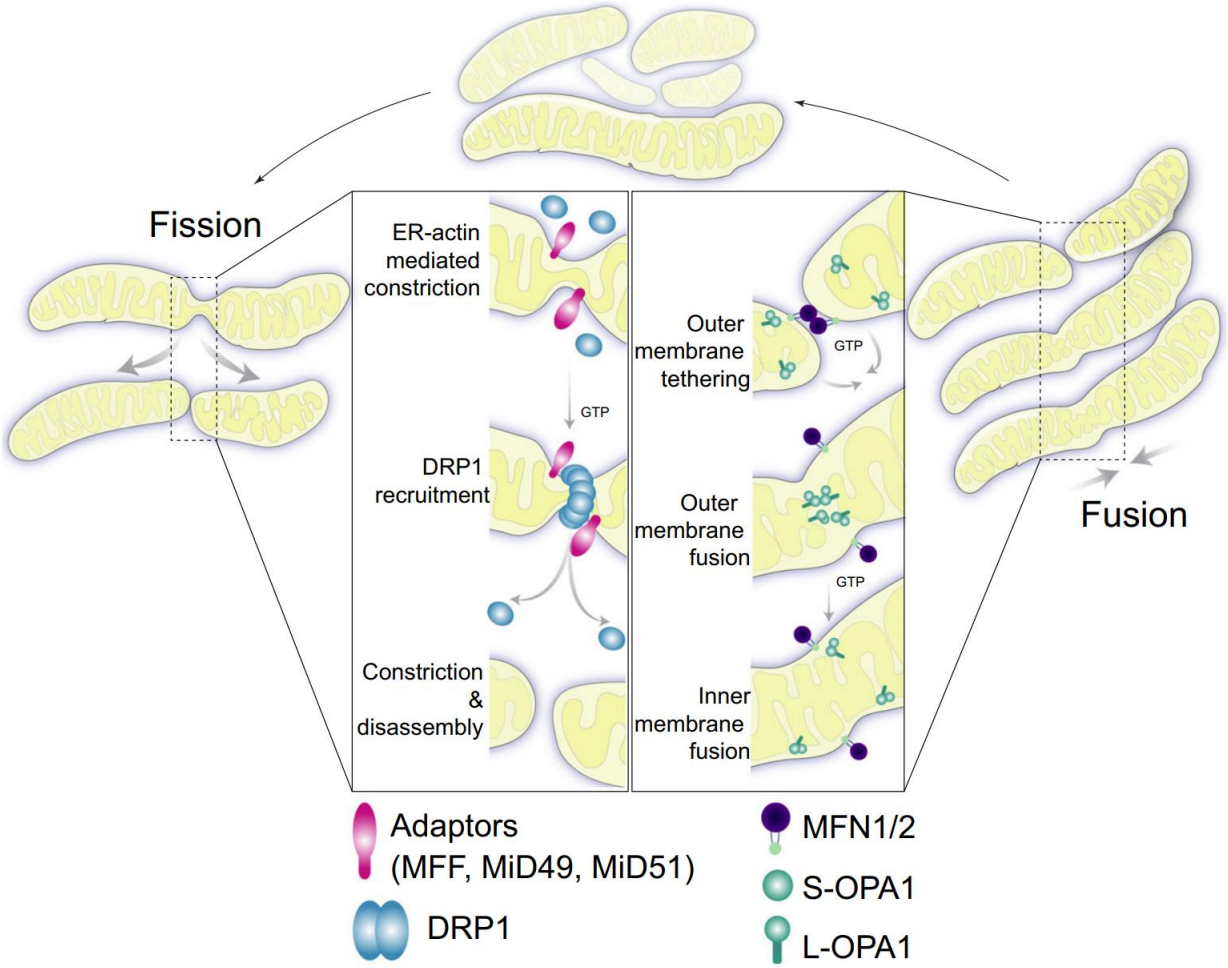

Figure 2: Fusion and fission machinery. Fission involves ER-actin-mediated constriction, outer membrane tethering by GTP proteins, DRP1 recruitment, and eventual constriction and disassembly. Fusion involves outer membrane fusion mediated by MFN1/2 and GTP proteins, followed by inner membrane fusion. Adaptor proteins like MFF, MiD49, MiD51 and membrane-bound proteins like S-OPA1 and L-OPA1 play crucial roles in the regulation of these dynamic processes that maintain mitochondrial morphology and function [22].

Healthy mitochondria require a balance between the removal of deficient/damaged mitochondria (mitophagy) and the generation of new mitochondria (mitochondrial biogenesis) [39]. Mitochondrial biogenesis is essential for the growth and retrieval of the mitochondrial network, providing adaptability to conditions of high energy demands [17]. This process is mediated by activating the peroxisome proliferator-activated receptor γ co-activator 1-α (PGC1- α), orchestrating coordinated synthesis and importing proteins and lipids from mitochondrial and nuclear DNA [40]. Moreover, mitochondrial biogenesis functions as an energy sensor. When an energy imbalance occurs, AMPK triggers the activation of PGC1-α, increasing mitochondrial biogenesis [16]. Conversely, this process is downregulated by a high nutritional load [20]. In neurons, generation of new

mitochondria plays a pivotal role in post-injury recovery. Hence, mitochondrial biogenesis is crucial for synaptogenesis and brain development [39].

Mitophagy denotes a specialised degradation pathway for damaged mitochondria, the autophagolysosomal pathway, which is primarily mediated by PTEN PINK1/Parkin [17]. Upon $\Delta\Psi m$ decrease, PINK1 accumulates on the outer mitochondrial membrane, promoting the recruitment of the E3 ubiquitin ligase Parkin. Additionally, adaptor proteins (SQSTM/p62, optineurin, NDP-52, among others) promote autophagosome formation and subsequent lysosomal fusion [17].

An increase in fragmented neuronal mitochondria and damage of the inner membrane is a common feature of several brain pathologies, including Alzheimer's, Parkinson's, Huntington's, and Amyotrophic Lateral Sclerosis [41], [42]. This leads to the idea that fission inhibitors may play a role in therapeutic alternatives to neurodegenerative disorders [43].

As mitochondria fission and fusion are antagonistic processes, a malfunction in one of them can exacerbate the other. For instance, impairments in fusion processes, such as ubiquitin-mediated degradation of Mfn2 or inhibition of Mfn1 by phosphorylation, increase mitochondrial fission and apoptosis [44]. Furthermore, increased Drp1 levels induced by glutamate toxicity or ischemia can lead to a decrease of $\Delta\Psi m$, energy production, and an increase in mtDNA defects and cell death [38]. Conversely, it has been shown that reducing or inhibiting Drp1 confers neuroprotection, both *in vitro* and *in vivo* [38].

In the acute phase of hypoxia, within the first 4 hours, there is an upregulation of mitochondrial fusion, while fission is suppressed. This initial response is thought to be a protective mechanism, ensuring sustained energy production, and preventing cellular damage. However, during the later phase, between 12 to 24 hours post-insult, mitochondrial fusion and membrane potentials diminish, mitochondrial fission becomes more pronounced. Concurrently, there is an increased release of cytochrome c from the mitochondria into the cytosol. These alterations in mitochondrial dynamics contribute to the activation of apoptotic pathways and exacerbate cellular injury in the setting of prolonged hypoxia [45], [46].

Several key alterations in mitochondrial function and dynamics have been observed in the context of neonatal hypoxic-ischemic (HI) injury. A decrease in mitochondrial ETC complex activity has been reported in the cerebral cortex and hippocampus, observed at both 2- and 18 hours post-injury in a P7 rat model of HI. Furthermore, sex-dependent differences have been observed, indicating a decrease in mitochondrial mass and membrane potential exclusively in female subjects at 18 hours post insult [47].

Female rats exhibit significantly higher levels of antioxidant defence compared to males. This contrast becomes pronounced in the context of HI, male rats showing elevated oxidative stress levels and impaired mitochondrial respiration in a rat model of HI injury at P7 [48]. In the same model, there was a marked increase in fragmented mitochondria and neuronal death. Interestingly, sex-specific differences in the outcome emerged, with

female brains exhibiting lower neuronal death rates and higher levels of mitophagy, suggesting a neuroprotective mechanism involving segregation and subsequent degradation of damaged mitochondria [49].

In mice subjected to HI insult at P9, mitochondrial fusion protein OPA1 increases, yielding short inactive forms (S-OPA1), which are associated with increased mitochondrial fission. This appears to be mediated by the zinc-metalloprotease Oma1, which is implicated in impaired fusion processes [50].

Moreover, mitochondrial biogenesis is upregulated in response to HI at P7, peaking between 6 to 24 hours post-insult. This increase in biogenesis is characterised by elevated mitochondrial DNA expression, increased protein synthesis, and enhanced activity of transcriptional regulators, such as TFAM and NRF1, with no significant changes observed in PGC-1α levels [51].

Furthermore, prenatal hypoxia leads to increased mitochondrial biogenesis in the hippocampus eight days post-insult, accompanied by a rise in damaged mitochondria. Overactivation of the PGC-1α pathway improves the outcomes, reducing damaged mitochondria and promoting biogenesis via the PGC-1α/NRF1/TFAM axis [52].

Finally, in a model of mild perinatal hypoxia at birth, it was found that hypoxia induced disruption of the brain-blood barrier, an increment of lactate levels right after the insult, along with an increase in mitochondrial oxygen consumption up to P7 and increased buffering capacity up to P14 [53]. Nevertheless, the status of mitochondrial dynamics in a model of global hypoxia at birth has not yet been elucidated.

A.5. Pharmacological Strategies

Currently, the only established treatment for the long-term damaging effects induced by PA is hypothermia, usually a decrease to 33-35ºC for 72 hours. Hypothermia reduces death and disabilities in term infants with moderate to severe encephalopathies due to PA [54]. Several pharmacological treatments have been proposed for PA, some of them entering clinical trial phases [55], including administration of antioxidants (N-acetyl-L-cysteine, polyphenols, melatonin, allopurinol); NMDA and AMPA antagonists (topiramate, memantine); gases (xenon, argon); matrix metalloproteinase inhibitors (Doxycyclin); erythropoietin; cannabinoids, and stem cells [56]. Among these treatments, mesenchymal stem cells (MSCs) have already been tested for neonatal hypoxic-ischemic injury, together with hypothermia [57], [58]. Consensus on hypothermia protocol has not been achieved yet, making it evident that research on novel therapeutic alternatives is required.

A.6. Mesenchymal Stem Cells

Mesenchymal stem cells are undifferentiated multipotent cells that can proliferate and self-renew [59]. MSCs have therapeutic potential due to their ability to migrate to the focus of injury, a process known as homing [60]. In addition, MSCs can differentiate into multiple cell types, replacing damaged tissue, and also capable of being easily isolated from adult tissue [59]. Furthermore, the paracrine action of MSCs has been recognised as its main therapeutic action. Indeed, MSCs have the capacity to secrete a broad array of bioactive factors into the extracellular space, called secretome [61]. MSCs secretomes (MSC-S) contain many active biomolecules, such as cytokines, growth factors, lipid messengers, mRNAs, and miRNAs [62]. Secretome can be divided into two fractions, a soluble fraction composed of cytokines, chemokines and growth factors, and a vesicular fraction, composed of different types of vesicles involved in the delivery of miRNA and proteins [63].

A.6.1. Mesenchymal Stem Cells: Secretome

The use of MSC-S offers several advantages over the traditional use of MSC therapies. It resolves safety considerations associated with the administration of living proliferative cells with the capacity to migrate, which has been associated with tumorigenesis [64]. Moreover, the manufacturing, storage, and handling of MSC-S are simplified, since secretomes can be lyophilised, reducing logistical challenges [65]. The production costs are advantageous as MSC-S can be produced in large quantities by reutilising cells. MSC-S can be evaluated for safety, dosage, and potency, like conventional drugs [61].

Additionally, it has been described that in vitro preconditioning of MSCs improves their therapeutic efficacy [66]. For instance, adipose tissue-derived MSCs, when preconditioned with pro-inflammatory cytokines (TNF-α and IFN-γ), increased their pro-regenerative, anti-inflammatory, and antioxidative properties [67]. Similarly, preconditioning MSCs with deferoxamine (DFX), an iron chelator with antioxidant properties that mimic hypoxia, improved the secretion of pro-angiogenic, anti-inflammatory, and neuroprotective factors [68].

MSC-S exhibits a multitarget therapeutic approach due to the presence of various bioactive molecules [64]. Emerging evidence suggests a link between the effects of MSC-S and the nuclear factor erythroid 2 related factor 2 (Nrf2) pathway, studied in different models such as sepsis [69], pulmonary fibrosis [70], fat grafts [71], ageing [72], depression like-behaviour [73], acute kidney injury [74], and alcoholism [75].

Results of our laboratory demonstrate that the intranasal administration of secretome derived from DFX-preconditioned MSCs in rats, 2 hours after PA, reduced hippocampal oxidative stress and increased nuclear Nrf2 protein levels in hippocampus at P7 [76].

A.7. Nrf2 Pathway

Nrf2 is a transcription factor, the primary activator of the antioxidant response element (ARE). Under basal conditions, it is found in the cytoplasm, bound to the Kelch-like ECH-associated protein 1 (Keap1), an adapter for the ubiquitin ligase Cul3/Rbx1 that mediates the proteasomal degradation of Nrf2 via ubiquitination, maintaining Nrf2 at low levels [77]. This transcriptional factor is critical to cells for the regulation of the redox balance, inducing antioxidant and detoxifying enzymes [78]. Oxidative stress promotes the activation of Nrf2 by oxidation of cysteine residues within Keap1, leading to a conformational change that allows the division of the complex. Once Nrf2 is free, it translocates to the nucleus, forming a complex with the small Maf protein, binding to AREs promoters (Fig.3). Some of the targets of Nrf2 include proteins of phase II detoxification, enzymes involved in antioxidant and anti-inflammatory responses, and enzymes from the pentose phosphate and nucleotide synthesis pathways [79].

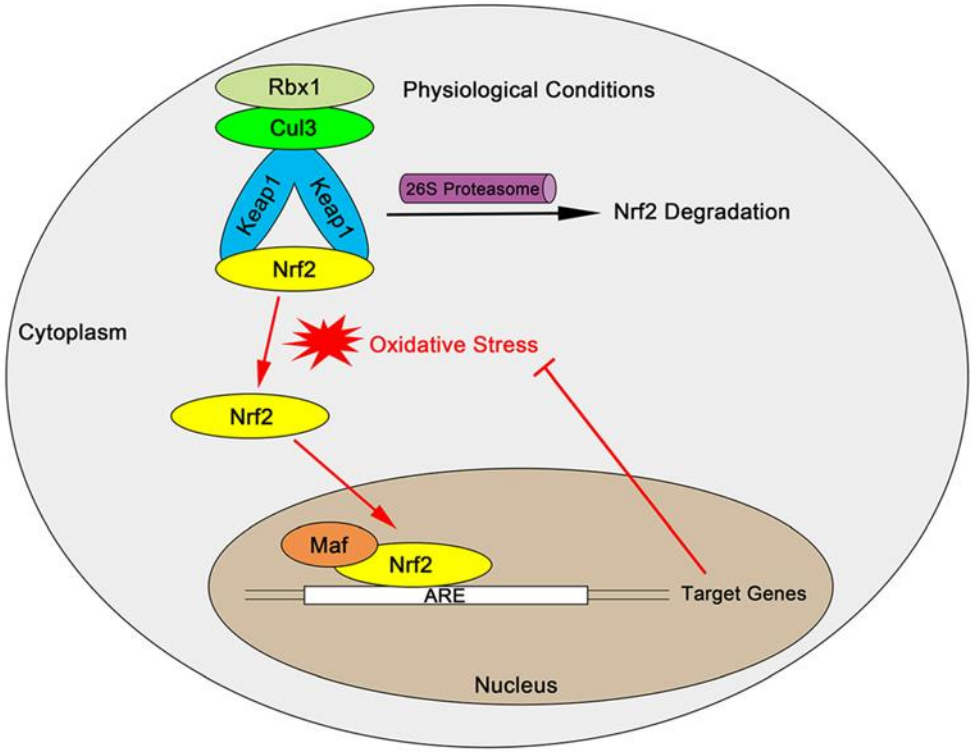

Figure 3: Nrf2 under physiological conditions and oxidative stress. In the cytoplasm, Nrf2 is normally bound to Keap1, leading to its degradation via proteasome. Under physiological conditions, this process maintains low levels of Nrf2. Under oxidative stress, Nrf2 dissociates from Keap1 and accumulates in the cytoplasm, then translocates to the nucleus, where it binds to small Maf proteins and the antioxidant response element (ARE) to activate the transcription of target genes involved in cellular defence against oxidative stress [78].

A.7.1. Nrf2 Pathway: Mitochondria

The Nrf2 pathway is a regulator of mitochondrial function, including bioenergetics, redox homeostasis, and quality control [80]. Nrf2 enhances mitochondrial respiration and ATP production by increasing the availability of substrates like NADH, FADH2, and acetyl-CoA through its effects on fatty acid oxidation, the TCA cycle, and other metabolic pathways [80], [81]. It also regulates mitochondrial biogenesis by upregulating the expression of nuclear respiratory factors and the transcriptional coactivator PGC-1α [81]. Additionally, Nrf2 contributes to mitochondrial quality control by promoting mitophagy through the upregulation of PINK1 and the autophagy substrate p62 facilitating the recognition and clearance of dysfunctional mitochondria [82].

The Nrf2 pathway plays a pivotal role in regulating mitochondrial ROS production and redox homeostasis. Nrf2 reduces mitochondrial oxidative stress by inducing the expression of antioxidant enzymes, such as those involved in glutathione synthesis and regeneration, thereby maintaining the mitochondrial redox balance [81]. Nrf2 deficiency leads to increased mitochondrial ROS generation, primarily due to impaired mitochondrial respiration and limited substrate availability for the electron transport chain [83]. Nrf2 also modulates the expression of NADPH oxidase isoforms, which are major sources of cytosolic ROS. NOX2 expression is upregulated in Nrf2 deficiency, while NOX4 is upregulated upon Nrf2 activation [83]. This regulation of ROS production from both mitochondrial and cytosolic sources highlights the crucial role of Nrf2 in maintaining cellular redox balance.

Moreover, Nrf2 activation confers resistance to mitochondrial permeability transition pore opening, preserving mitochondrial integrity under stress conditions [82], [83]. Given the dysregulation of Nrf2 in mitochondria-related disorders and the protective effects of Nrf2 activators in various disease models, the Nrf2 pathway has emerged as a promising therapeutic target for mitigating mitochondrial dysfunction and associated pathologies [84].

Additionally, the activation of Nrf2 pathway by dimethyl fumarate (DMF) shows an increase in the average mitochondrial length, through the degradation of the fission protein Drp1 [85]. Therefore, there is an association between the activation of Nrf2 pathway and mitochondrial dynamics.

In summary:

PA leads to severe consequences for brain neonates, being the hippocampus one of the most affected brain regions, known for its vulnerability to metabolic insults. PA induces a cascade of detrimental events, including oxidative stress, mitochondrial dysfunction, and delayed cell death in the neonatal brain. Mitochondrial dynamics, the delicate balance between fission and fusion processes, play a pivotal role in regulating cellular energy homeostasis and apoptosis. While mitochondrial dynamics have been studied in neurodegenerative diseases and HI conditions, the investigation specifically addressing PA is limited, in particular with models mimicking labour complications.

Currently, therapeutic hypothermia is the only established treatment for PA, emphasising the need for novel approaches. Treatments with MSC-S have shown to be promising. Recent findings from our laboratory demonstrated that intranasal administration of secretome derived from preconditioned MSCs reduced oxidative stress and increased nuclear Nrf2 levels in asphyxia-exposed animals. Evidence suggests that the Nrf2 pathway is a key mechanism of MSC therapeutic effects, regulating cellular redox homeostasis, mitochondrial biogenesis, and mitophagy. However, its impact on mitochondrial dynamics remains underexplored.

Chapter 2: Hypothesis and Aims

A.8. Hypothesis:

Perinatal asphyxia increases mitochondrial fission, inducing delayed cell death in rat hippocampus. These alterations are prevented by neonatal intranasal administration of secretome derived from preconditioned human mesenchymal stem cells via Nrf2 pathway activation.

A.9. General Aim:

To determine the effects of perinatal asphyxia on mitochondrial dynamics and delayed cell death in rat hippocampus, investigating whether neonatal intranasal administration of secretome derived from preconditioned human mesenchymal stem cells prevents these alterations via Nrf2 pathway activation.

A.10. Specific Aims:

[SA1] To determine whether the therapeutic effect exerted by intranasal administration of secretome derived from preconditioned human mesenchymal stem cells after PA depends on Nrf2 pathway activation in the rat hippocampus.

-To study the Nrf2 activation pathway, monitoring protein and mRNA levels of Nrf2 effectors after intranasal MSC-S administration at P1, P7 and P14 by WB, qPCR and IHQ.

[SA2] To determine the effects of PA and MSC-S on mitochondrial dynamics, oxidative stress, and cell death in rat hippocampus at P1, P7 and P14.

-To study the effects of PA and intranasal MSC-S administration on cell death and oxidative stress at P1, P7 and P14 by TUNEL, WB and MDA.

-To study the effects of PA and intranasal MSC-S administration on mitochondrial respiratory metabolism and mitochondrial dynamics at P1 and P7 by WB, and IHQ.

Chapter 3: Methodology

Animals and induction of perinatal asphyxia (PA).
Wistar rats from the Molecular & Clinical Pharmacology Programme animal station, ICBM, Faculty of Medicine, University of Chile, Santiago, Chile, were used in all experiments. Animals were kept in a temperature and humidity-controlled environment with a 12/12-hour light/dark cycle, fed *ad libitum*. When not used for the experiments, qualified personnel monitored the animals' well-being permanently, following the ARRIVE guidelines for reporting animal studies (www.nc3rs.org.uk/ARRIVE). A Local Committee approved animal procedures for Experiments with Laboratory Animals of the University of Chile (Protocol-CBA# 20426 FMUCH).
On the last day of gestation, pregnant rats (G22) were euthanised as previously reported, performing a caesarean section rapidly to remove the uterine horns [23]. Some pups were excised from the uterine horns immediately after hysterectomy, providing caesarean-delivered controls, while the remaining foetuses, still in their uterine horns, were transferred to a bath at 37°C for 21 minutes to induce severe asphyxia. Following 21 minutes of asphyxia, the pups were removed from the uterine horns and stimulated to breathe on a temperature-controlled pad at 37ºC. Two hours after birth, control and asphyxia-exposed animals were treated with either MSC-S or saline via intranasal administration. Animals were euthanised at postnatal day 1 (P1), P7 or P14 by decapitation, and the hippocampus was dissected for protein or RNA/DNA extraction. For immunofluorescence, the animals were transcardially perfused with 0.1M phosphate-buffered saline (PBS) followed by 4% paraformaldehyde (PFA). Following perfusion, the whole brains were carefully extracted and postfixed in PFA solution for 48 hours.

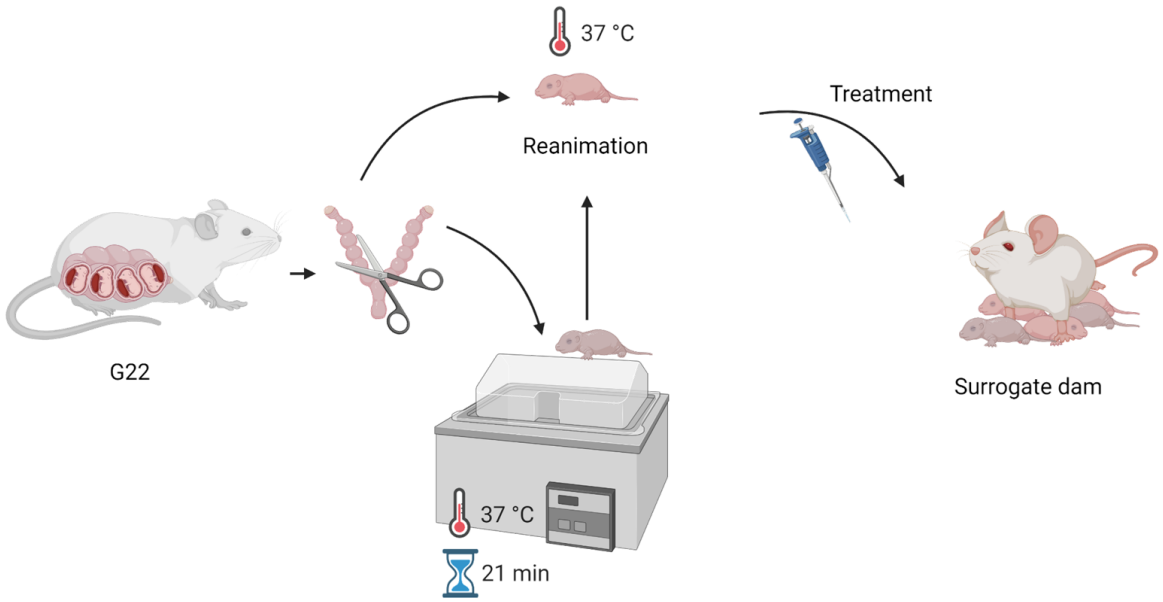

Figure 4: Perinatal asphyxia model (Biorender).

Human adipose tissue derived-MSC preconditioning, purification of MSC-derived secretome, and intranasal administration.

These procedures were performed at the associated laboratory (Dr. F. Ezquer, Universidad del Desarrollo-Clínica Alemana). Human MSCs were isolated from subcutaneous adipose tissue samples obtained with written informed consent from a healthy donor undergoing cosmetic liposuction at Clínica Alemana, Santiago, Chile. The entire procedure was conducted under protocols approved by the Faculty of Medicine Ethics Committee at Clínica Alemana-Universidad del Desarrollo, Santiago, Chile (Protocol 2020-30), following the WHO Guiding Principles on Human Cell, Tissue and Organ Transplantation. MSCs were isolated and characterised according to [75]. MSCs at 70% confluence were preconditioned by incubation in α-MEM medium supplemented with 10% foetal bovine serum and 400 µM deferoxamine (DFX) for 48 hours [68]. Secretome from MSCs (MSC-S) was obtained by harvesting the culture media according to [68]. A proteomics characterisation of the secretome has been reported in [86]. The MSC-S was obtained from DFX-preconditioned MSCs derived from one donor and kept frozen at -80 °C pending further experiments. A total volume of 16 µL, containing 6 µg of secretome (derived from $2x10^5$ preconditioned-MSCs), was administered intranasally two hours post delivery, as follows: 1 µL of secretome solution was administered every 5 min, alternating between the right and left nostril, totalling eight doses for each nostril. As a control, 16 µL of saline solution (0.9% NaCl) was administered as previously described [76].

Experimental groups.

The following groups of animals were considered (n=4-8 for each group): (a) Control animals: Rats delivered by a caesarean section but not exposed to PA, treated with vehicle (C.Vhc) or with secretome (C.MSC-S). (b) Rats exposed to 21 min of PA, were treated with vehicle (A.Vhc) or secretome (A.MSC-S).

Lactate in blood.

The Edge™ blood lactate monitoring system was used to evaluate lactate concentration. A whole blood drop from the tail of the animal was placed on the test strip, and the result was reported on the display of the device after 45 seconds.

Western Blot (WB).

Hippocampal protein extraction was performed using RIPA buffer (150 mM NaCl, 1% Triton X-100, 0.5% sodium deoxycholate, 0.1% SDS, and 50 mM Tris pH 8, with a phosphatase and protease inhibitor cocktail) and protein concentration was quantified by the bicinchoninic acid (BCA) protocol (Thermofisher, cat. 23227). Protein electrophoresis was performed using SDS polyacrylamide gel, with 6% stacking and 12% separating gel. Protein samples (50 µg) were mixed with a loading buffer (40% glycerol, 8% SDS, 8% β-mercaptoethanol, 0.02% bromophenol blue, and 250 mM Tris HCl buffer pH 6.8) and then heated at 100°C for 5 min. Electrophoresis was performed at constant 100V, electrotransferred onto a 0.2 µm pore nitrocellulose membrane (BIO-RAD) at 2.5A for 10 min in a

Trans-Blot® TurboTM. Protein transference to the membrane was evaluated using Ponceau red staining (0.1% Ponceau red, 0.1% acetic acid). Then, the membrane was blocked with 5% non-fat milk (Bio-Rad, cat. 1706404) diluted in Tris-Base Saline (TBS) 0.05 % Tween-20 (TBS-T) at room temperature (RT) for 60 min. Primary antibodies were: NQO1 (1:750, cat. 3187S, Cell Signaling), HO1 (1:1000, cat. 43966S, Cell Signaling), GSR (1:1000, cat. ab124995, Abcam), Drp1 (1:1000, cat. sc-271583, Santa Cruz), pDrp1 S616 (1:1000, cat. PA5-64821, Invitrogen), pDrp1 S637 (1:1000, cat. ab193216, Abcam), Fis1 (1:1000, cat. PA5-22142 ,Thermo Scientific), OPA1 (1:250, cat. sc-30573, Santa Cruz) and β-Actin (1:10000, cat. #251003, Synaptic Systems), diluted in TBS-T. Membranes were incubated overnight with the respective antibody in agitation at 4°C. After that, membranes were washed with TBS-T three times for 10 min at RT with constant shaking, then incubated with the corresponding horseradish peroxidase (HRP) conjugated secondary antibody (Thermo Scientific Pierce, USA), diluted 1:5000 in TBS-T, at RT and constant shaking, for one hour. Membranes were revealed using PierceTM Enhanced chemiluminescence Western Blotting Detection kit for HRP (Thermo Fisher Scientific, Inc., cat. 32209). Finally, ChemiScope 3400 (ClinX Sciences Instruments Co, Ltd) was used to capture the chemiluminescence. Images were processed by Image J 1.52f software (National Institutes of Health, USA). The values are normalised to their respective β-actin and their control.

DNA/RNA extraction and retro-transcription (RT).

Extraction of RNA and DNA was performed with TRIzol (Invitrogen, cat. 15596026) according to the manufacturer's instructions. For reverse transcription, 1 µg of total RNA was treated with DNAase I (Invitrogen, cat. 18068-015). MMLV (Invitrogen, cat. 28025-013) and Oligo dT (Promega, cat. C1101) were used for retro-transcription from RNA to cDNA. Finally, cDNA was diluted to 25ng/ul and DNA to 10ng/µL.

*Quantitative polymerase chain reaction (**qPCR**)*.

Amplification was conducted in a final volume of 25 µL, using Brilliant II SYBR Green qPCR Master Mix (Agilent Technologies, cat. 600828) with a qPCR Mx3000p (Stratagene, La Jolla, CA, USA). The expression was normalised with β-actin or 18S gene and determined using the 2−ΔΔCT method (see Table 1).

Table 1. qPCR primers

Gene	Primer Forward 5′→ 3′	Primer Reverse 5′→ 3′	Amplicon size (bp)
β actin	AAGTCCCTCACCCTCCCAAAAG	AAGCAATGCTGTCACCTTCCC	125
NQO1	CTCGCCTCATGCGTTTTTG	CCCCTAATCTGACCTCGTTCAT	70
HO1	ACAGGGTGACAGAAGAGGCTAA	CTGTGAGGGACTCTGGTCTTTG	107
Gclc	CTGAGGCAAGATACCTTTATGACC	GTAGCTATCTATTGAGTCATACCGAGAC	227
Prdx	GGCGTGTTGAAAAATGATGAG	GTCCCACAGGTAGGTCGTTG	103
GSR	TCTCACCCCAGTTGCGAT	CTCGTGGTCACAGCGTGATA	228
Nrf2	CACATCCAGACAGACACCAGT	CTACAAATGGGAATGTCTCTGC	121
18S	GGGAGGTAGTGACGAAAAATAACAAT	TTGCCCTCCAATGGATCCT	101

D-loop	GGTTCTTACTTCAGGGCCATC	GATTAGACCCGTTACCATCGAGAT	102
TFAM	GATGAGTCAGCTCAGGGGAAA	ACGGATGAGATCACTTCGCC	174
PGC1α	TGGAGTGACATAGAGTGTGC	GGGCTCATTGTTGTACTGGT	180

Lipid Peroxidation (MDA).

MDA quantification was assessed by homogenising the hippocampi according to the manufacturer's guidelines (MAK085, Sigma Aldrich), followed by measurement of absorbance at 532 nm using a Biotek Synergy HT spectrophotometer.

GSSG/GSH ratio.

The samples were homogenised in PBS 0.1 M pH 7.5, supplemented with 5 mM EDTA disodium salt, and deproteinised with metaphosphoric acid (5%). Glutathione disulfide (GSSG) in the sample was converted into GSH by glutathione reductase in the presence of NADPH. Total glutathione concentration involves the oxidation of GSH by 5,5′-dithiobis (2-nitrobenzoic acid) (DTNB) to form a yellow derivate which was measured at 412 nm.

Design of the antisense oligonucleotide (ASO) for Nrf2.

The design of the Nrf2 antisense oligonucleotide was kindly carried out by Dr Yedy Israel, using the presence of the motif (5'→3') GGGA or GGGGA in the mRNA sequence of rat Nrf2, as described by [87]. The Nrf2 used sequence was: Rattus norvegicus strain mixed chromosome 3, Rnor_6.0, NCBI reference sequence; NC_005102.4. Since the DNA sequence of Nrf2 from 5' to 3' was used, it was converted to the RNA sequence from 5' to 3', then to RNA from 3' to 5', and finally to the DNA sequence from 5' to 3', resulting in two ASOs: (i) ASO-NF #1; 5′- AAGTTC CAACT CCCCC ATTCA-3′ (n=21 nucleotides), and (ii) ASO-NF#4; 5′- GGTTT AGCTT CCCCC TTAAT A -3′ (n=21 nucleotides). The corresponding scrambled sequences (SCR) were: (i) SCR-NF #1; 5′- AGGACC TTACA CACCC CATTT-3′ (n=21 nucleotides), and (ii) SCR-NF #4, 5′- TTCTG TCATG TGTCC AAACT C -3′ (n=21 nucleotides). The presence of secondary structures was tested for all sequences using Nucleotide Blast from NCBI and http://www.oligoevaluator.com/LoginServlet. The ASOs and SCRs were ordered with a phosphorothioate modification for improved stability from www.idtdna.com. Subsequently, Dr. Pablo Berríos tested the ASOs and SCRs in rat astrocyte cell line DI TNC1 (which expresses relatively high levels of Nrf2) using 300nM of ASOs or SCRs with Lipofectamine 2000 lipid cation. Analysis was performed 48 hours after transfection. First, the transfection efficiency was determined by coupling a fluorophore to it and performing flow cytometry, which indicated an 84.1% efficiency with transfected cells. Then, qPCR was used to determine the levels of Nrf2 mRNA using the two ASOs and their respective SCRs, indicating that only ASO-NF #1 suppressed Nrf2 expression by approximately 42% compared to SCR. Based on these results, it was concluded that only ASO-NF #1 and its respective SCR would be used in the in vivo experiment using asphyxiated rats. The ASO and SCR were administered via intracerebroventricular (ICV) injection performed 2 hours after birth, followed by intranasal

administration of MSCS or vehicle 24 hours after birth, as previously described. Subsequently, samples were extracted at P7, as described earlier.

Terminal Deoxynucleotidyl Transferase dUTP Nick End Labeling (TUNEL).

Coronal sections were processed with the in-situ apoptosis detection TUNEL kit (DeadEnd™ Fluorometric TUNEL System, Promega, cat. G3250) according to the supplier's instructions, with some modifications. The samples were washed in 0.1M PBS three times for 10 minutes, then permeabilised in 0.5% Triton X-100 in 0.1M PBS solution, for 30 minutes at RT, and rinsed three times in 0.1M PBS for 5 minutes each time. Thereafter, the samples were incubated with equilibrium buffer for 10 minutes at RT, to proceed to incubation with the deoxynucleotidyl transferase terminal (TdT) enzyme during 90 minutes at 37°C in a humidified chamber, avoiding exposure to light from this step forward. Apoptotic nuclei were marked in this reaction with green fluorescence. The reaction was stopped with 2X SSC solution for 15 minutes at RT. Then the slides were washed six times in PBS for 5 minutes each time, to proceed to the immunofluorescence protocol. As a negative control, a set of sections was incubated in the absence of TdT enzyme. To quantify apoptotic cell death, the study employed two complementary approaches. The TUNEL assay detected DNA fragmentation, a characteristic feature of apoptotic cells. Additionally, the presence of apoptotic nuclei was evaluated based on their morphological features using DAPI staining. Pyknotic nuclei, exhibiting nuclear shrinkage and increased chromatin condensation, were considered as indicators of apoptosis.

Immunofluorescence.

The brain was post-fixed in 4% PFA for 48 hours at 4°C, then immersed in 10% sucrose for one day and 30% sucrose (both sucrose solutions in 0.1M PBS, pH 7.4) pending further treatments. The samples were cryo-embedded in Tissue-Tek O.C.T. (Sakura Finetek USA, Inc.). Coronal sections (30 or 50 µm thick) of the hippocampi (between Bregma−1.40 and 2.00 mm) were obtained using a cryostat (Thermo Scientific Microm HM 525, Germany). Sections were collected in 0.1 M PBS solution, pH 7.4 and stored at 4°C. The floating tissue or adhered slices were incubated with a blocking solution (1% BSA, 10% NGS, and 0.3% Triton X-100 in 0.1M PBS) for 2 hours at RT in agitation. Then, the samples were incubated with the primary antibody: anti-TOMM20 (1:400, ST04-72, Novus Biologicals), anti-MAP2 (1:250, cat. MAB3418, Sigma-Aldrich) or anti-Nrf2 (1:100, cat. ab89443, Abcam) diluted in a blocking solution overnight at 4°C. As a negative control, the tissue was incubated in blocking solution, without primary antibody. After three rinses with 0.1M PBS 0.1% Tween for 5 minutes at RT, sections were incubated with a secondary antibody anti-rabbit-Alexa 488 or anti-mouse 647 (Thermo Fisher Scientific, IL, USA), 1:250 in blocking solution containing 1% NGS, and 0.02M 4,6-diamino-2-phenylindol (DAPI) (Thermo Fisher Scientific, cat. D1306) for nuclear labelling, for 4 hours at 4ºC in agitation, then rinsed three times for 5 minutes for further Expansion microscopy protocol or 2 hours at RT for Nrf2 or TUNEL experiments.

Expansion microscopy (ExM).

Expansion microscopy was conducted based on an already reported protocol [88]. Immunostained brain sections of 50 µm were incubated with 1 mM methacrylic acid N-hydroxy succinimidyl ester (MA-NHS) for 1 hour, as a linker molecule, and incubated for 40 min with a monomer solution (Sodium acrylate/Acrylamide/N-methylene bisacrylamide) at 4ºC. Gelation was performed by replacing the incubation monomer solution with fresh monomer complemented with 4OH-TEMPO/TEMED/APS for 2 hours at 37ºC. After gelation, the tissue was digested by incubation with 16 U/mL proteinase K at 37ºC for 16 hours in digestion buffer. To be expanded, the gels were incubated in ultrapure water for 48 hours before image capture. Once expanded, gels were immobilised in coverslips to obtain images using a confocal microscope (FV1000, Olympus, Tokyo, Japan) with a 60X objective,1.2 NA, and water immersion. Excitation with 405 and 488 nm lasers were used to collect the images.

ExM efficiency was confirmed by the acquired DAPI nuclei staining sample images calculating the experimental expansion factor, and the area ratio before and after ExM was measured. At least two photos per hippocampal region (CA1 and suprapyramidal blade of DG) were evaluated. The analysis of mitochondrial morphology was conducted using Ilastik software for pixel classification, followed by quantification using a custom-written algorithm implemented in MATLAB software (MathWorks, Natick, MA, USA). The custom algorithm was designed to segment mitochondria based on the Ilastik classification for measurement of morphological parameters such as mitochondria density, area, and circularity (with a minimum of 0 and a maximum of 1, with 1 being the most round). The segmentation accuracy was visually confirmed by overlaying the segmented objects onto the original images. Data from all images were averaged for each animal and used for statistical analysis.

Mitochondrial Membrane Potential.

The mitochondrial membrane potential (ΔΨm) was evaluated using the MITOISO1 kit (Sigma-Aldrich) according to the manufacturer's instructions for isolating mitochondria from whole brain samples, excluding the frontal pole. After quantifying the protein content, 25 µg of protein extract was mixed with 0.04 mM safranin O (SO) in a final volume of 100 µL. The initial fluorescence was measured at 495 nm excitation and 586 nm emission using a BioTek Synergy H1 reader. To induce mitochondrial depolarisation for the final fluorescence measurements, carbonyl cyanide 4-(trifluoromethoxy)phenylhydrazone (FCCP) was added to achieve a final concentration of 0.5 mM.

Statistical analysis.

Data are presented as the mean ± standard error of the mean (SEM). Normality of the data was assessed using the Shapiro-Wilk test. For normally distributed data, a two-way analysis of variance (ANOVA) was performed to evaluate the effects of the experimental conditions (control or asphyxia) and treatment (vehicle or MSC-S), followed by Tukey's post hoc test for multiple comparisons. When data did not follow a normal distribution,

the Kruskal-Wallis test was used, followed by Dunn's post-hoc test for multiple comparisons. A P-value less than 0.05 ($P<0.05$) was considered a statistically significant difference. Statistical analyses were performed using GraphPad Prism software (version 5.0, GraphPad Software Inc., San Diego, CA, USA). Details of the Statistics are further inserted into the legends for each Figure.

Chapter 3: Results

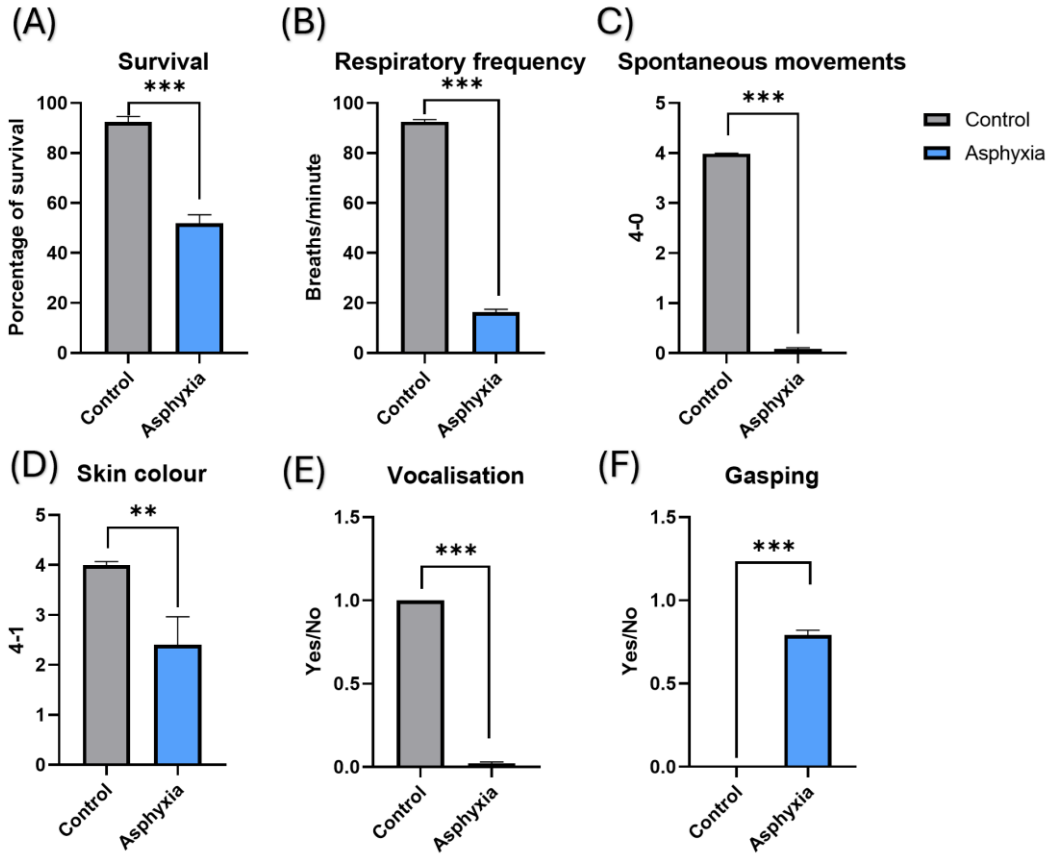

Figure 5: Apgar evaluation after 40 minutes of birth. A: Survival as a percentage. B: Respiratory frequency in breaths/minute. C: Spontaneous movements (4: movement of the 4 limbs, 0: no movement). D: Skin colour (4: pink, 3: bluish pink, 2: pinkish blue and 1: blue). E: Presence of vocalisation. F: Presence of gasping. Data are expressed as means ± SEM, C.Vhc (n=94-181), A.Vhc (n=100-191). T-test, **p<0.01, ***p <0.0001.

Apgar score was evaluated 40 minutes after caesarean in controls and 61 minutes after for asphyxia animals, calculated from the moment when the uterine horns were cut off. The survival of PA animals was decreased compared to control animals, from 92% to 51%. In addition, respiratory frequency, spontaneous movements, skin colour, vocalisation and gasping were evaluated (Fig.5). The respiratory frequency, spontaneous movements, skin colour and vocalisation were decreased in asphyxia compared to control animals (P <0.0001, P <0.0001, P= 0.0065, and P <0.0001), and gasping was increased in asphyxia animals compared to control (P <0.0001). Additionally, the parameters were divided and analysed by sex (Annex1), and no differences were found among groups.

Lactate, a pyruvate metabolite, serves as the primary energy currency during anaerobic metabolism. To validate the PA model, blood lactate levels were measured using a portable lactate acid analyser at different time points after birth (Fig.6). PA induces an increase in lactate levels compared to the control group, observed from 5 up to 60 minutes only. The 2 groups were analysed at each time. Longer times (4 hours onwards) were analysed along with the treated groups. At 4 hours lactate levels increased in A.Vhc and A.MSC-S compared to C.Vhc. Results at 24 hours showed that lactate levels stabilised at a lower level in all groups. When separating the results by sex (Annex2), both males and females showed an increase in lactate levels from 5 to 30 minutes when compared to asphyxia and control groups.

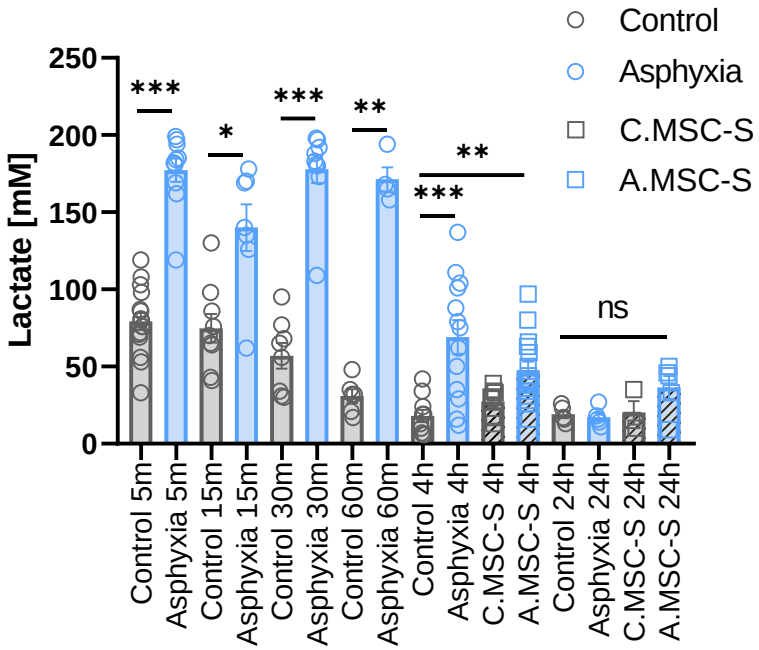

Figure 6: Lactate concentration in blood following PA and MSC-S treatment. Results are presented as mM. Data are expressed as means ± SEM, C.Vhc (n=5-16), A.Vhc (n=4-10), C.MSC-S (n=3-9), A.MSC-S (n=5-15) at different time points, from 5 minutes to 24 hours. Grey circles/grey bar: Control or C.Vhc. Blue circles/blue bar: Asphyxia or A.Vhc. Grey square/striped-grey bar: C.MSC-S. Blue square/striped-blue bar: A.MSC-S. Mann-Whitney test for 5 to 60 min was used and Kruskal-Wallis analysis, followed by Dunn's as a post-hoc test for 4 and 24 hours, *$p<0.05$, **$p<0.01$, ***$p<0.001$, ns $p>0.05$.

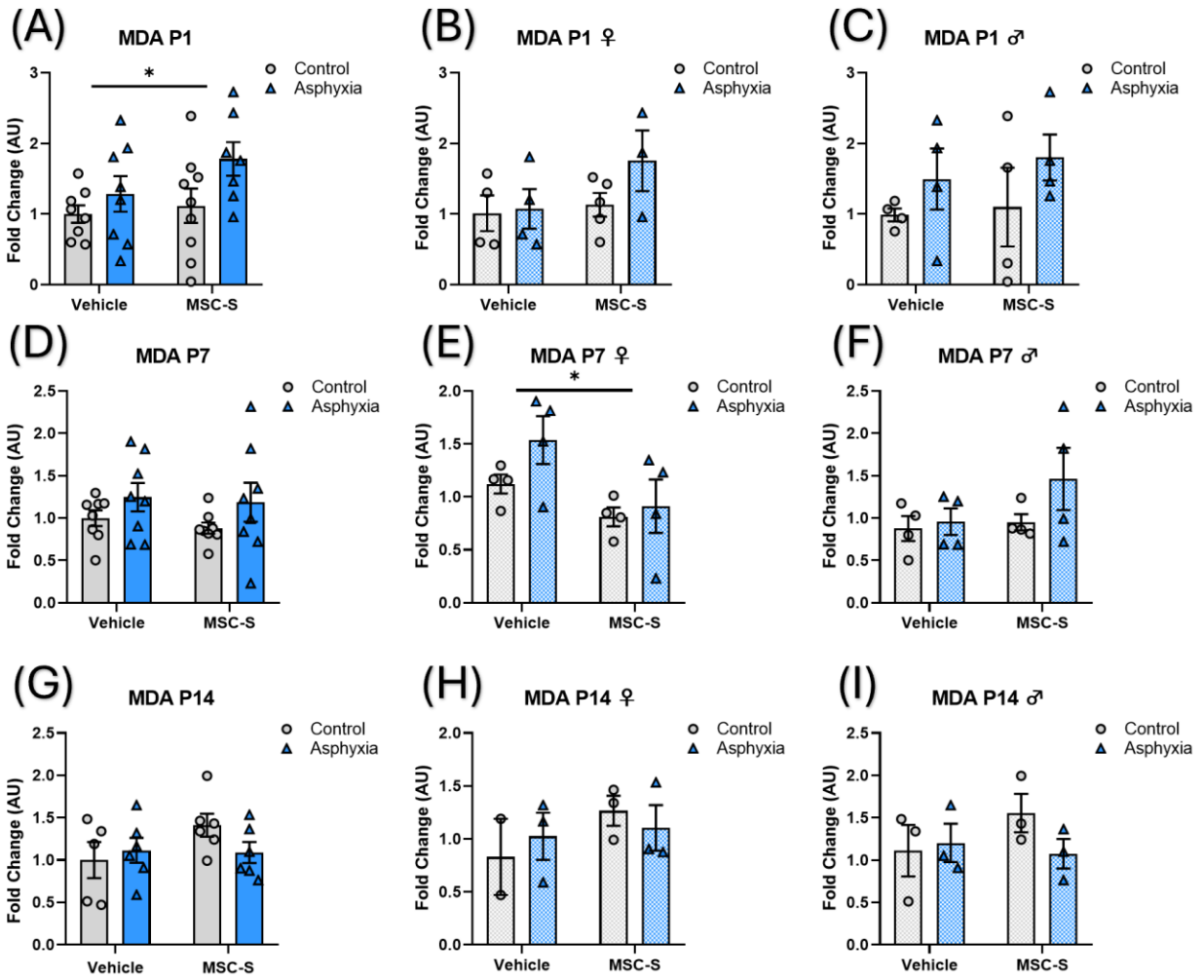

Figure 7: Oxidative stress in hippocampus at P1, P7 and P14 following PA and MSC-S treatment. MDA quantification A: at P1, D: P7 and G: P14 and B-C, E-F and H-I: segregated by sex. Results are presented as a fold of change to C.Vhc. Data are expressed as means ± SEM, normalised by control. C.Vhc (n=3-8), A.Vhc (n=3-8), C.MSC-S (n=3-8), A.MSC-S (n=3-8). Two-way ANOVA, followed by Tukey as a post-hoc test, *p<0.05.

Oxidative stress and cell death following PA.

Malondialdehyde (MDA), a product of lipid peroxidation during oxidative stress, was used as a marker for oxidative stress. Analysis of MDA levels in hippocampus at P1 showed a significant difference in the column factor (control versus asphyxia) ($F_{(1, 28)}$ = 4.530, P=0.0422), suggesting an increase in MDA levels in both asphyxia-exposed groups compared to the control groups (Fig.7A). At P7 no difference in MDA levels were detected among groups (Fig.7D). However, at P7 only the female animals showed an effect at treatment level ($F_{(1, 12)}$ = 6.681, P=0.0239), suggesting an increase in MDA levels in the A.Vhc group of females (Fig.7E). At P14, no differences in MDA levels among the groups were observed (Fig.7G-H).

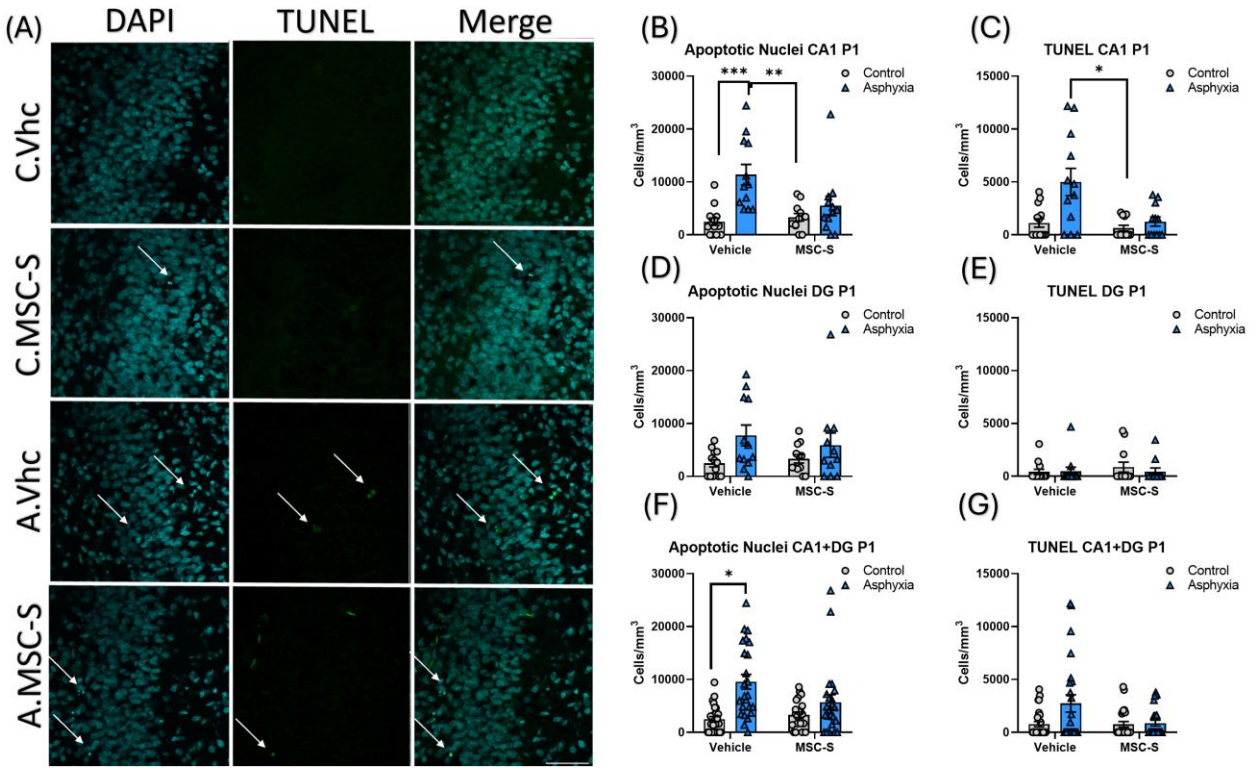

Figure 8: Apoptotic cell death in hippocampus at P1 following PA and MSC-S treatment. A: Representative image of TUNEL assay, scale bar: 50µm, arrows indicate apoptotic nuclei and TUNEL positive cells. DAPI is shown in cyan and TUNEL in green. Apoptotic nuclei expressed as positive pyknotic nuclei/mm^3 are shown in B: CA1, D: DG and F: CA1+DG. TUNEL positive cells/mm^3 are shown in C: CA1, E: DG and G: CA1+DG. Data are expressed as means ± SEM, C.Vhc (n=13-26), A.Vhc (n=12-24), C.MSC-S (n=12-24), A.MSC-S (n=11-23). Kruskal-Wallis analysis, followed by Dunn's as a post-hoc test *p<0.05, **p<0.01, ***p<0.001.

To evaluate cell death, TUNEL assay was used. In addition to TUNEL quantification, apoptotic nuclei were measured by DAPI according to apoptotic nuclear morphology (pyknotic nuclei). At P1, apoptotic cell death was increased in A.Vhc compared to C.Vhc (P=0.0002) and C.MSC-S (P=0.0071) in CA1 (Fig.8B) and A.Vhc compared to C.Vhc (P=0.0313) in CA1+DG (Fig.7F). CA1 showed an increase in TUNEL-positive cells only in CA1 analysis, in A.Vhc compared to C.MSC-S group (P= 0.0211) (Fig.8C). No differences were observed in DG region.

At P7, analysis of the CA1+DG regions revealed a notable increase in apoptotic nuclei in A.Vhc compared to both the C.Vhc (P= 0.0146) and C.MSC-S (P= 0.0481) groups (Fig.9B). Specifically focusing on the CA1 region, a difference in apoptotic nuclei was observed (P= 0.0075) (Fig.9D), with a tendency to increase in asphyxia-exposed groups. Nevertheless, this tendency did not reach statistical significance in the multiple comparisons. Similarly, the TUNEL assay showed a significant difference (P= 0.0336) (Fig.9E), indicating a tendency of increased TUNEL labelling in the asphyxia-exposed groups compared to the controls. Still, no significant changes were observed among the groups.

At P14, no significant differences were observed among the groups, whether measuring the CA1 and/or DG regions together or separately (Fig.10).

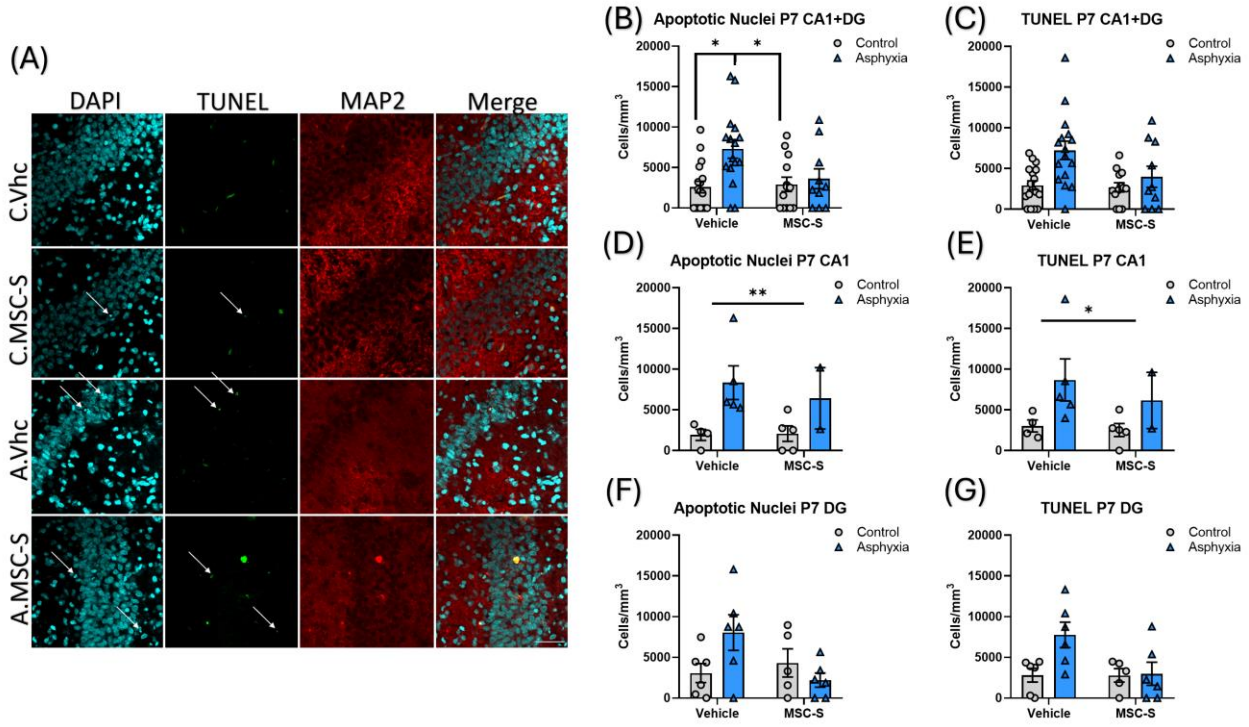

Figure 9: Apoptotic cell death in hippocampus at P7 following PA and MSC-S treatment. A: Representative image of TUNEL assay, scale bar: 50µm, arrows indicate apoptotic nuclei and TUNEL positive cells. DAPI is shown in cyan, TUNEL in green and MAP2 in red. Apoptotic nuclei expressed as positive pyknotic nuclei/mm^3 are shown in B: CA1, D: DG and F: CA1+DG. TUNEL positive cells/mm^3 are shown in C: CA1, E: DG and G: CA1+DG. Data are expressed as ± SEM, C.Vhc (n=4-16), A.Vhc (n=5-16), C.MSC-S (n=5-11), A.MSC-S (n=2-10). Kruskal-Wallis analysis, followed by Dunn's as a post-hoc test *p<0.05, **p<0.01.

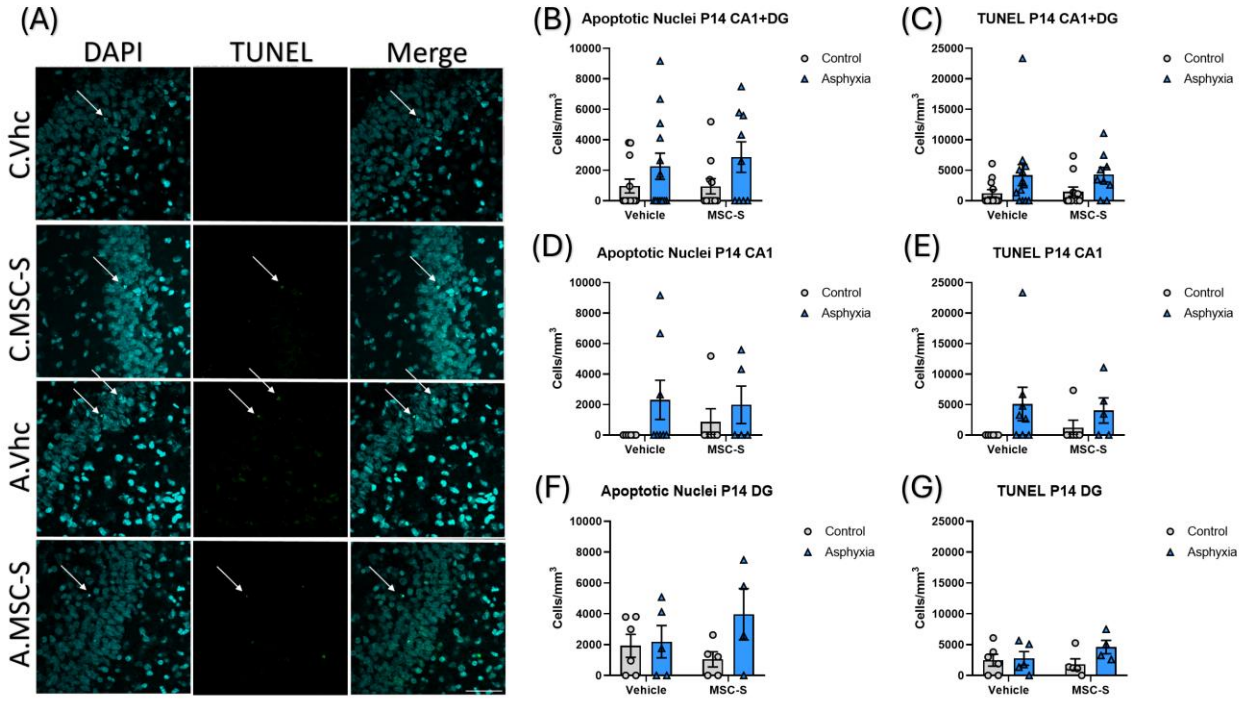

Figure 10: Apoptotic cell death in hippocampus at P14 following PA and MSC-S treatment. A: Representative image of TUNEL assay, scale bar: 50µm, arrows indicate apoptotic nuclei and TUNEL positive cells. DAPI is shown in cyan and TUNEL in green. Apoptotic nuclei expressed as positive pyknotic nuclei/mm^3 are shown in B: CA1, D: DG and F: CA1+DG. TUNEL positive cells/mm^3 quantification are shown in C: CA1, E: DG and G: CA1+DG. Data are expressed as means ± SEM, C.Vhc (n=6-16), A.Vhc (n=5-16), C.MSC-S (n=5-11), A.MSC-S (n=4-10). Kruskal-Wallis analysis, followed by Dunn's as a post-hoc test *p<0.05, **p<0.01.

Nrf2 activation [SA1].

Total and nuclear Nrf2 levels were measured in CA1 and DG zones of the hippocampus by immunofluorescence at P1, P7 and P14. At P1 and P7, no differences were observed in Nrf2 levels among the groups, or between zones (Fig.11 and Fig.12).

At P14 (Fig.13), total Nrf2 levels were increased in the A.Vhc group compared to the C.Vhc in CA1 (P=0.0425) and CA1+DG (P=0.0011). Increased levels of total Nrf2 were also observed in A.MSC-S, compared to C.Vhc in DG (P=0.0377) and CA1+DG (P=0.0010). An increase in A.Vhc and A.MSC-S, compared to C.MSC-S, were observed when analysing CA1+DG (P=0.0220 and P=0.0181). Nuclear Nrf2 levels increased in asphyxia, compared to control groups in DG (P=0.0322), and in A.MSC-S, compared to C.MSC-S in CA1+DG (P=0.0465).

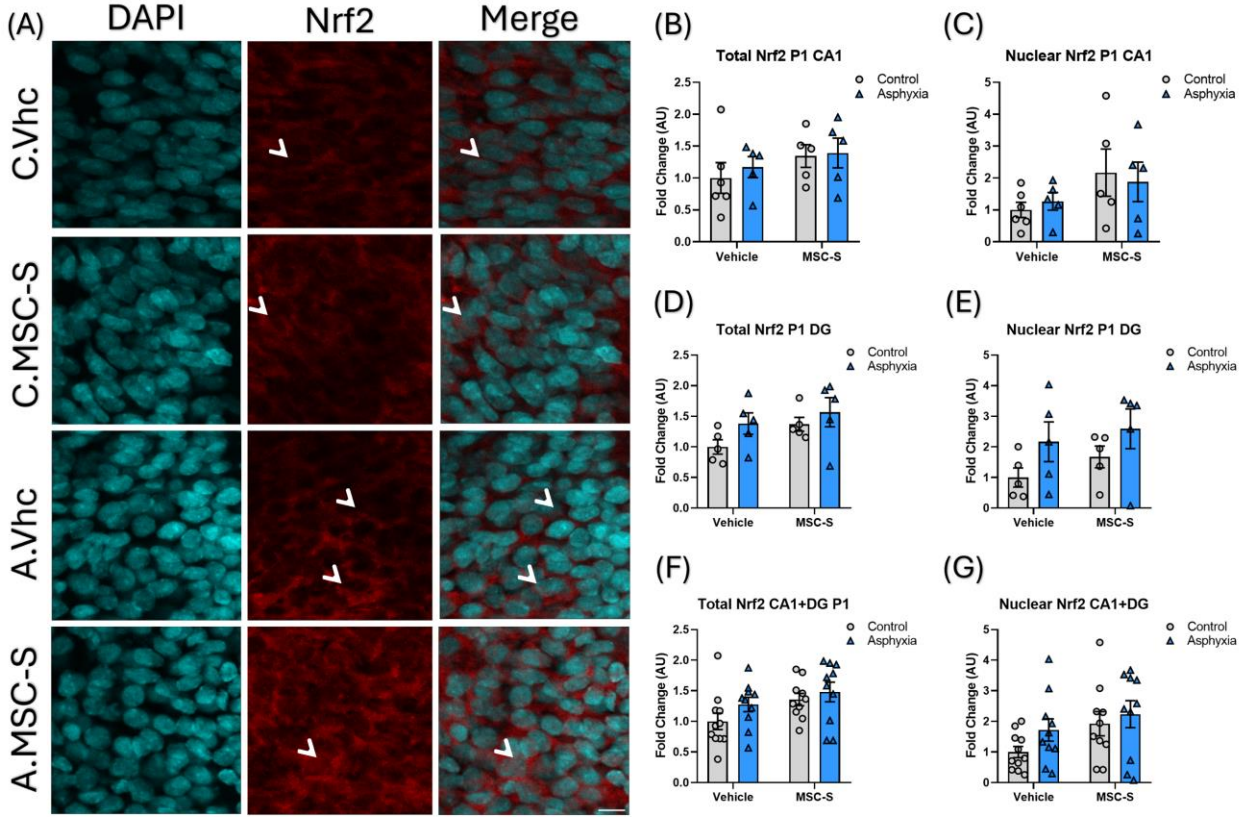

Figure 11: Nrf2 levels in hippocampus at P1 following PA and MSC-S treatment. A: Representative image of Nrf2 immunofluorescence, Nrf2 in red and DAPI in cyan, scale bar: 10µm, arrowheads indicate nuclear Nrf2. Total Nrf2 in B: CA1, D: DG and F: CA1+DG. Nuclear Nrf2 in C: CA1, E: DG and G: CA1+DG. Data are expressed as means ± SEM, normalised by control. C.Vhc (n=5-7), C.MSC-S (n=5-7), A.Vhc (n=6-7), A.MSC-S (n=5-7). Kruskal-Wallis test, followed by Dunn's post-hoc test, was used for statistical analysis, *p<0.05.

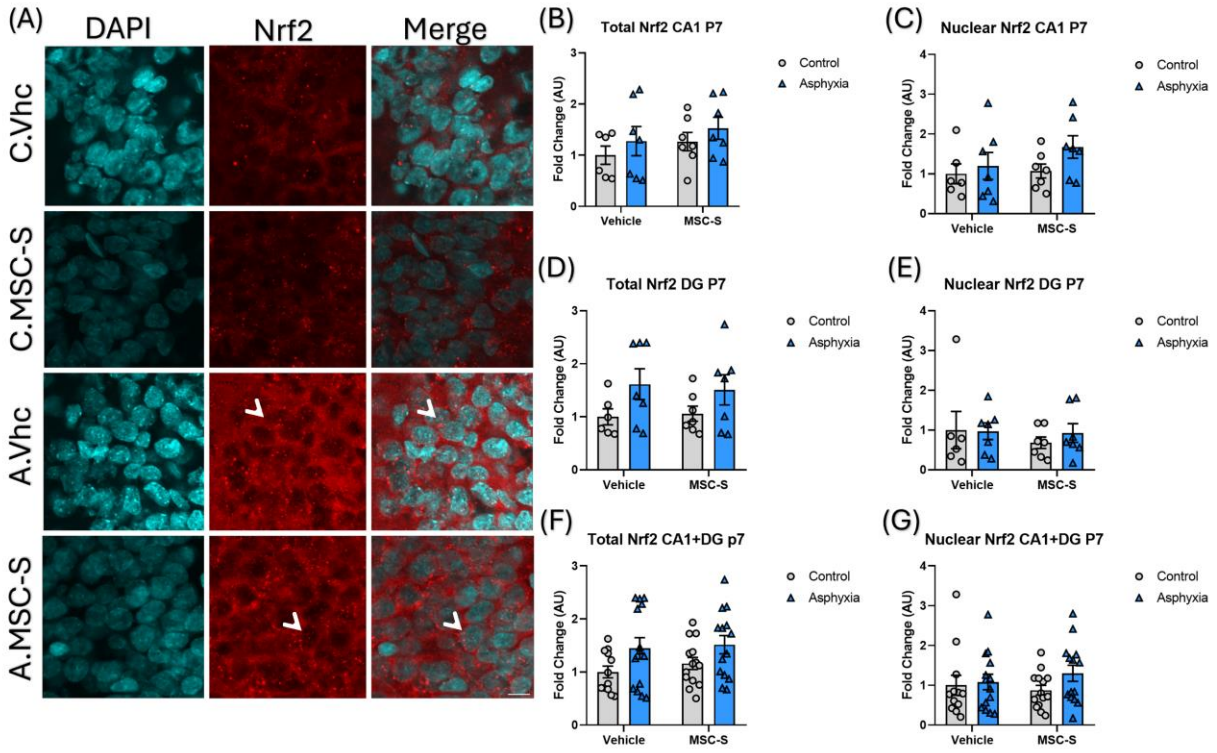

Figure 12. A: Representative image of Nrf2 immunofluorescence, Nrf2 in red and DAPI in cyan, scale bar: 10µm, arrowheads indicate nuclear Nrf2. Total Nrf2 in B: CA1, D: DG and F: CA1+DG. Nuclear Nrf2 in C: CA1, E: DG and G: CA1+DG. Data are expressed as means ± SEM, normalised by control. C.Vhc (n=5-7), C.MSC-S (n=5-7), A.Vhc (n=6-7), A.MSC-S (n=5-7). Kruskal-Wallis test, followed by Dunn's post-hoc test, was used for statistical analysis, *$p<0.05$.

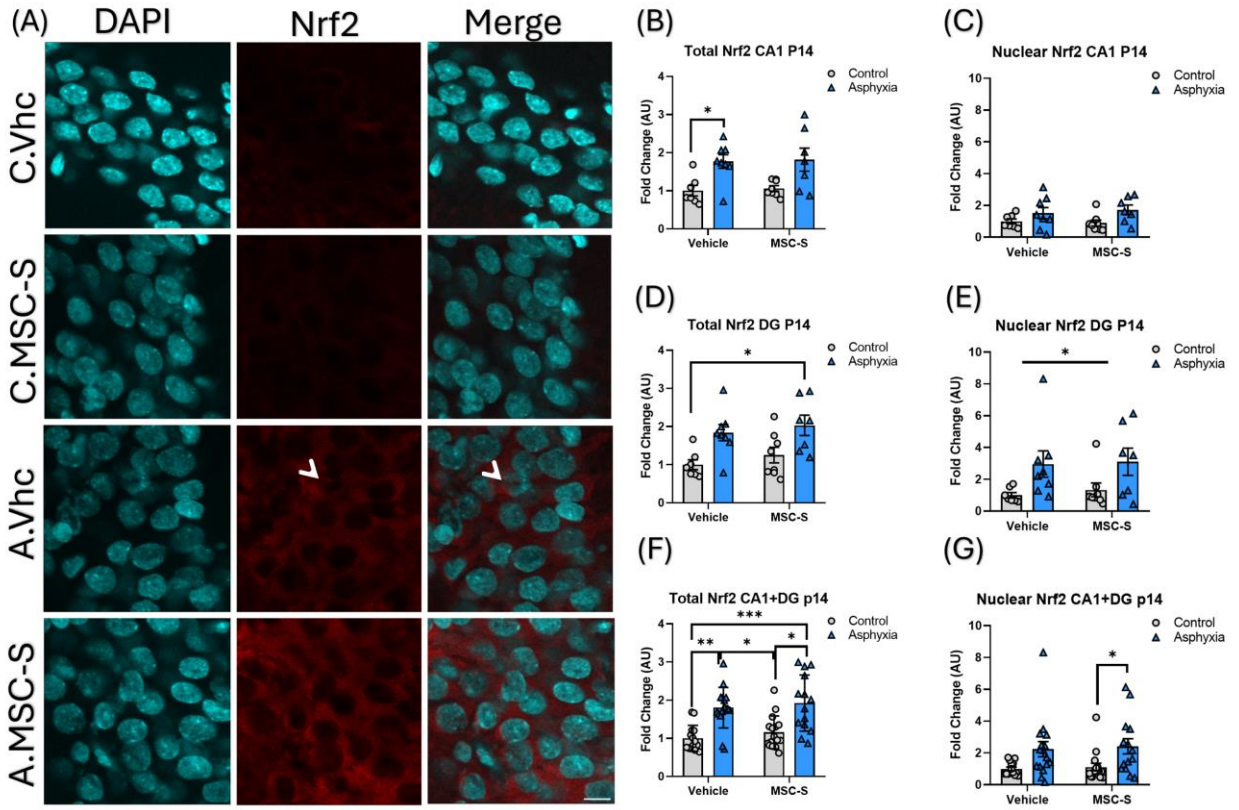

Figure 13: Nrf2 levels in hippocampus at P14 following PA and MSC-S treatment. A: Representative image of Nrf2 immunofluorescence, Nrf2 in red and DAPI in cyan, scale bar: 10µm, arrowheads indicate nuclear Nrf2. Total Nrf2 in B: CA1, D: DG and F: CA1+DG. Nuclear Nrf2 in C: CA1, E: DG and G: CA1+DG. Data are expressed as means ± SEM, normalised by control. C.Vhc (n=5-7), C.MSC-S (n=5-7), A.Vhc (n=6-7), A.MSC-S (n=5-7). Kruskal-Wallis test, followed by Dunn's post-hoc test, was used for statistical analysis, *p<0.05, **p<0.01, ***p<0.001.

mRNA levels of Nrf2 effectors at P1, P7 and P14.

Fig.14, shows Nrf2 mRNA levels and its effector genes, including Heme oxygenase1 (HO1), NAD(P)H Quinone Dehydrogenase 1 (NQO1), Glutathione reductase (GSR), Glutamate—cysteine ligase catalytic subunit (Gclc) and Peroxiredoxin (Prdx) at P1. No statistical differences among the groups were observed in Nrf2, HO1, NQO1, GSR and Gclc mRNA levels. However, MSC-S administration increased prdx2 mRNA levels, only in asphyxia-exposed rats (A.MSC-S group), compared to C.Vhc group (Fig.14F).

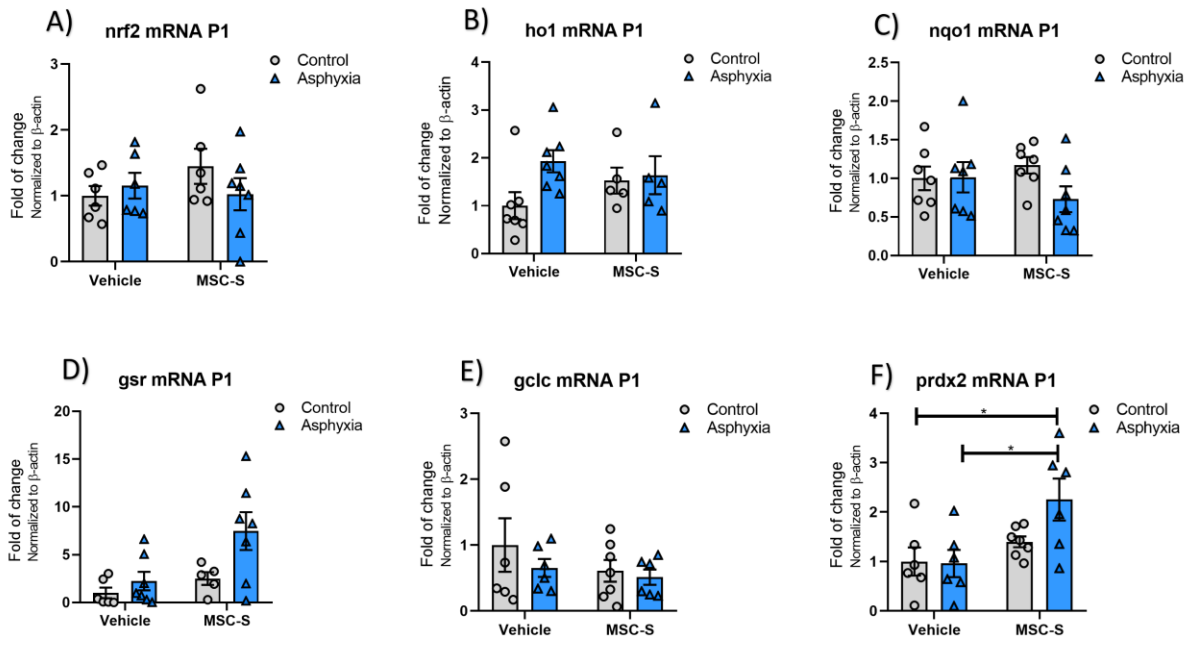

Figure 14: RT-qPCR analysis of Nrf2 gene and its effectors at P1 following PA and MSC-S treatment. mRNA levels of A: Nrf2, B: HO1, C: NQO1, D: GSR, E: Gclc and F: Prdx2. Results are presented as a fold of change relative to control levels. Data are expressed as means ± SEM. C.Vhc (n=5-7), C.MSC-S (n=5-7), A.Vhc (n=6-7), A.MSC-S (n=5-7). Two-way ANOVA, followed by Tukey as a post-hoc test, *p<0.05.

At P7, no differences in Nrf2 mRNA levels were observed among the groups (see Fig.15). There was, however, an increase in HO1 (P=0.0036) and NQO1 (P=0.0135) mRNA levels, when comparing A.MSC-S versus the C.Vhc group. GSR mRNA levels increased in the A.MSC-S group, compared to the controls (C.Vhc and C.MSC-S) (P=0.0135 and P=0.0207, respectively). Gclc mRNA levels increased in the MSC-S groups (C.MSC-S, and A.MSC-S), versus C.Vhc (P=0.0036 and P= 0.0046, respectively). prdx2 mRNA levels increased in the C.MSC-S group versus C.Vhc (P=0.0153). All Nrf2 effectors were increased after intranasal MSC-S administration, both under control and asphyxia-exposed conditions.

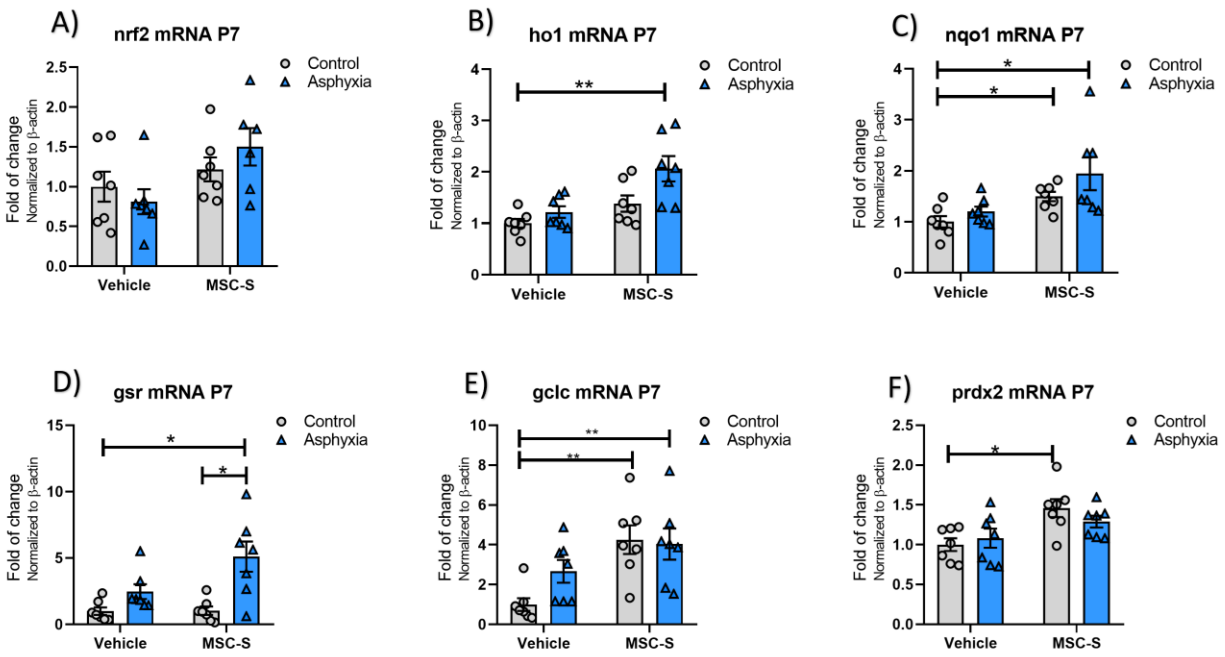

Figure 15: RT-qPCR analysis of Nrf2 gene and its effectors at P7 following PA and MSC-S treatment. mRNA levels of A: Nrf2, B: HO1, C: NQO1, D: GSR, E: Gclc and F: Prdx2. Results are presented as a fold of change relative to control levels. Data are expressed as means ± SEM, C.Vhc (n=7), C.MSC-S (n=7), A.Vhc (n=7), A.MSC-S (n=7). Two-way ANOVA, followed by Tukey as a post-hoc test, *p<0.05, **p<0.01.

At P14, GSR and Gclc mRNA levels were increased by PA, compared to that observed in the C.Vhc group (P=0.0188 and P=0.0388 respectively) (Fig.16). MSC-S administration increased Gclc mRNA levels in A.MSC-S, compared to the C.Vhc group (P=0.0388). No differences among the groups were observed for Nrf2, HO1, NQO1 and prdx2 mRNA levels.

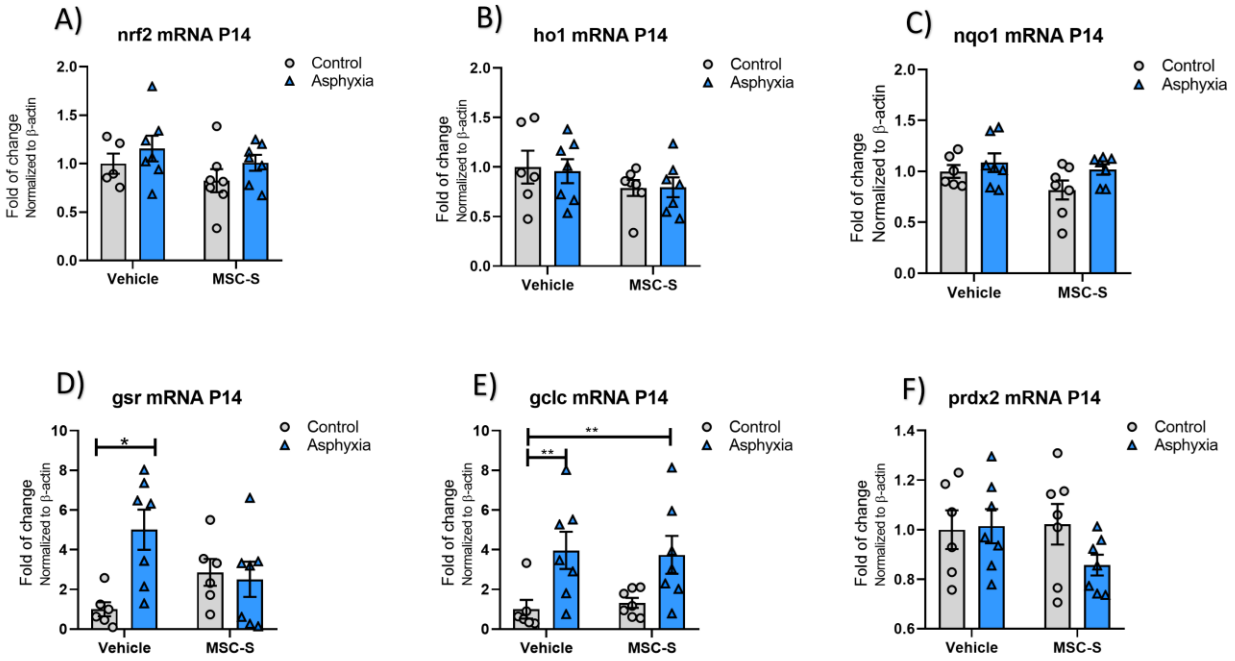

Figure 16: RT-qPCR analysis of Nrf2 gene and its effectors at P14 following PA and MSC-S treatment. mRNA levels of A: Nrf2, B: HO1, C: NQO1, D: GSR, E: Gclc and F: Prdx2. Results are presented as a fold of change relative to control levels. Data are expressed as means ± SEM, C.Vhc (n=5-6), C.MSC-S (n=6-7), A.Vhc (n=7), A.MSC-S (n=6-7). Two-way ANOVA, followed by Tukey as a post-hoc test, *p<0.05, **p<0.01.

Nrf2 effector protein levels at P1, P7 and P14

Western blot analysis of Nrf2 effector proteins, NQO1, HO1 and GSR at P1 and P7 were performed. At P1, no differences were observed among the groups (Fig.17). At P7, there was an increase in NQO1 protein levels in A.Vhc, compared to the C.Vhc group (P= 0.0256). At P7, there was an interaction effect between condition and treatment in HO1 and NQO1 GSR ($F_{(1,28)}$ = 8.018, P=0.0085), but the multiple comparisons test detected no differences. At P14, no differences were observed among the groups (Fig.19); while protein levels of GSR were decreased in A.MSC-S group, as compared to the C.Vhc group (P= 0.0274). An effect was appreciated in the A.Vhc group as well, but not reaching the statistically significant level.

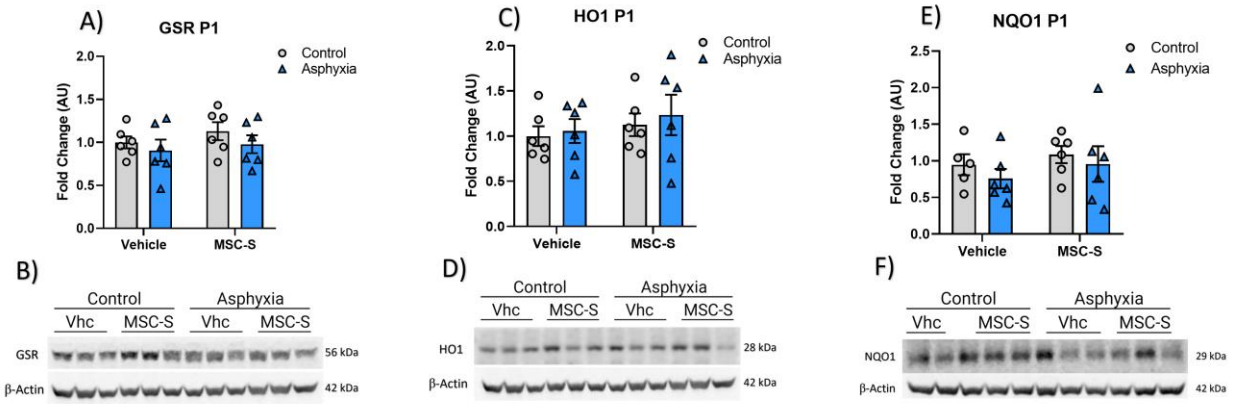

Figure 17: Western blot analysis of Nrf2 effectors at P1 following PA and MSC-S treatment. Protein levels and representative Western blot image of A-B: GSR; C-D: HO1, and E-F: NQO1. Results are presented as a fold of changes relative to control vehicle levels, normalised to β-actin as a loading control. Data are expressed as means ± SEM, C.Vhc (n=5-6), C.MSC-S (n=6), A.Vhc (n=6), A.MSC-S (n=6) Two-way ANOVA, followed by Tukey as a post-hoc test, *p<0.05.

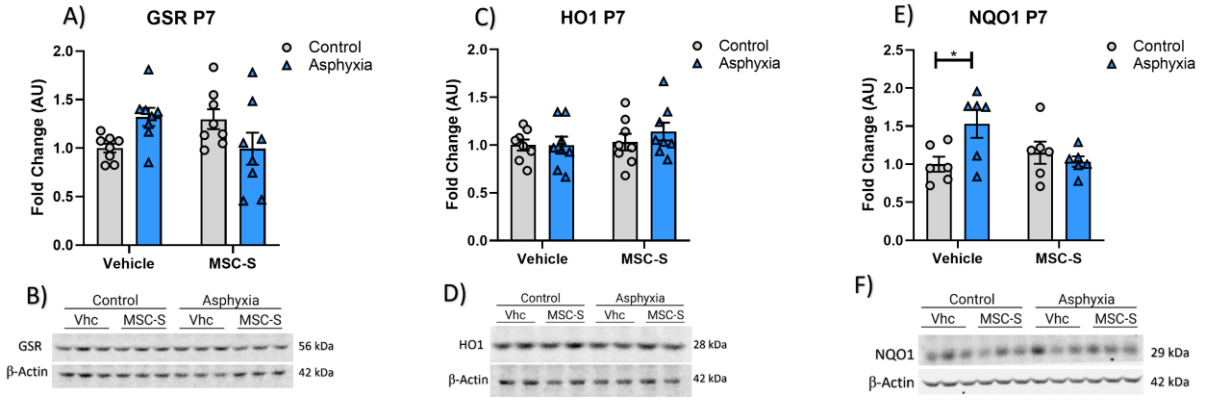

Figure 18: Western blot analysis of Nrf2 effectors at P7 following PA and MSC-S treatment. Protein levels and representative Western blot image of A-B: GSR; C-D: HO1, and E-F: NQO1. Results are presented as a fold of changes relative to control vehicle levels, normalised to β-actin as a loading control. Data are expressed as means ± SEM, C.Vhc (n=6-8), C.MSC-S (n=6-8), A.Vhc (n=6-8), A.MSC-S (n=6-8) Two-way ANOVA, followed by Tukey´s post-hoc test was used for statistical analysis, *p<0.05.

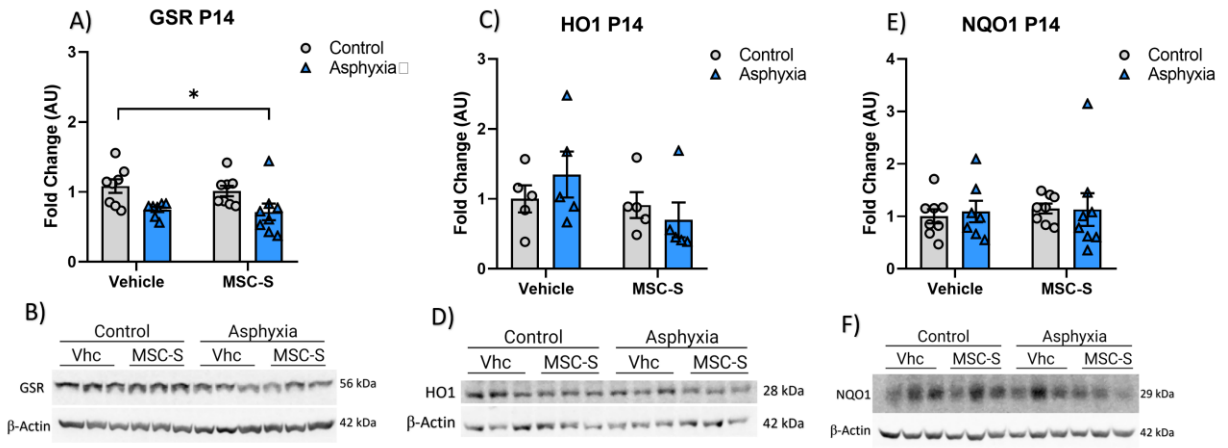

Figure 19: Western blot analysis of Nrf2 effectors at P14 following PA and MSC-S treatment. Protein levels and representative Western blot image of A-B: GSR; C-D: HO1, and E-F: NQO1. Results are presented as a fold of changes relative to control vehicle levels, normalised to β-actin as a loading control. Data are expressed as means ± SEM, C.Vhc (n=5-8), C.MSC-S (n=5-8), A.Vhc (n=5-8), A.MSC-S (n=5-8) Two-way ANOVA, followed by Tukey as a post-hoc test, *p<0.05.

Mitochondrial dynamics [SA2]

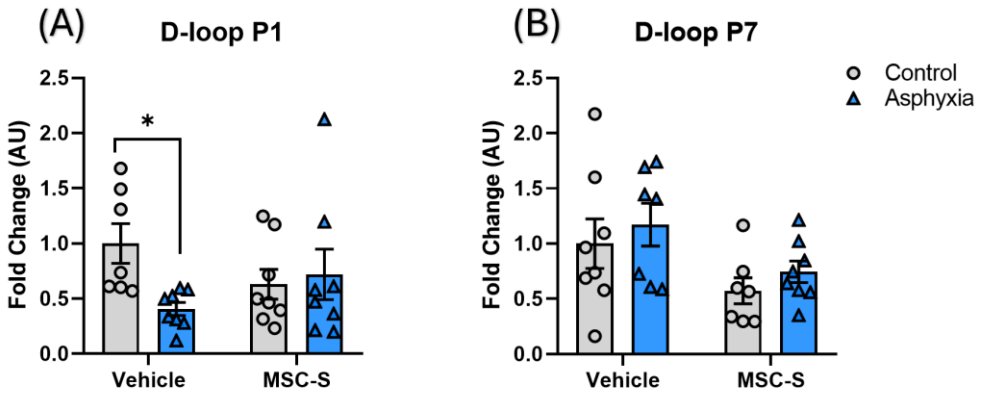

Figure 20: Mitochondrial DNA content in hippocampus at P1 and P7 following PA and MSC-S treatment. mtDNA content by qPCR amplification of the D-loop region, normalised to the 18S gene (housekeeper) in hippocampus A: at P1 or B: at P7. Data are presented as fold change relative to control levels, expressed as mean ± SEM, C.Vhc (n=6-7), C.MSC-S (n=8), A.Vhc (n=8), A.MSC-S (n=7-8). Kruskal-Wallis test, followed by Dunn's post-hoc test, was used for statistical analysis, *p<0.05. Data contain equal numbers of female and male animals (50/50 ratio).

Effect of asphyxia on mitochondrial mass.

In order to assess mitochondrial mass or quantity, the non-coding D-loop region of the mitochondrial DNA (mtDNA) was amplified by qPCR, using 18S as a normaliser at P1 and P7. The D-loop is essential for mtDNA replication and transcription, making it a suitable target for evaluating mitochondrial content. As shown in Figure 20, the D-loop quantity decreased in the A.Vhc group, compared to the C.Vhc group at P1 (P= 0.0256), suggests a decrease in the number of mitochondria in the asphyxia-exposed hippocampus. However, no differences were observed at P7 when analysing male and female together, or when the data was segregated by sex (Annex 4). Additionally, the expression of TFAM and PGC1α, key regulators of mitochondrial biogenesis, was analysed by RT-qPCR at P1 and P7, but no differences were observed among the groups (Annex 5), suggesting that alterations in mitochondrial biogenesis are not primarily driven by the observed changes in mitochondrial mass.

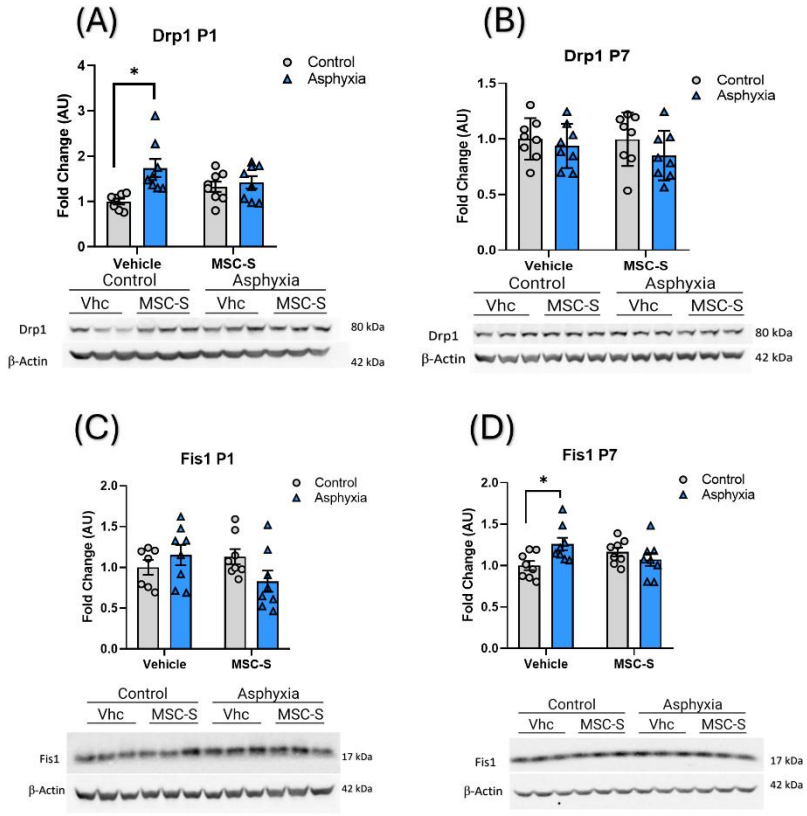

Figure 21: Fission protein levels in hippocampus at P1 and P7 following PA and MSC-S treatment. Protein levels and representative Western blot images of Drp1 and Fis1 A, C: at P1 and B, D: at P7. Data are presented as fold change relative to control levels, normalised to β-actin as the loading control, expressed as mean ± SEM, C.Vhc (n=6-7), C.MSC-S (n=8), A.Vhc (n=8), A.MSC-S (n=7-8). Two-way ANOVA followed by Tukey's post-hoc test was used for statistical analysis, *p<0.05. If sex is not indicated, data contain equal numbers of female and male rats (50/50 ratio).

Effect of asphyxia on mitochondrial fission proteins.

Mitochondrial fission proteins Drp1 and Fis1 levels were monitored by Western blot, normalised by β-actin at P1 or P7. As shown in Fig.21, there was no difference among the groups for Fis1 at P1 (Fig.21C), also when segregating the data by sex (Annex 7). However, at P7, there was an increase in Fis1 protein levels in A.Vhc compared with the C.Vhc group ($F_{(1,28)}$ = 6.996, P= 0.0132). The differences were lost in the A.MSC-S group. No differences were observed when segregating the data by sex (Annex 7).

When analysing total Drp1 levels, an increase in Drp1 levels was observed in A.Vhc compared with the C.Vhc group (P= 0.0061) (Fig.21A). When segregating by sex, an interaction was found between condition (control or asphyxia) and treatment (vehicle or MSC-S) in males ($F_{(1,11)}$ = 5.877, P=0.0337) (Annex 6). At P7, no differences among groups were observed. In addition, pDrp1 levels phosphorylated at Ser616 and Ser637 were also analysed, but no differences were observed among the groups at P1 and P7, neither in male nor in female animals (Annex8).

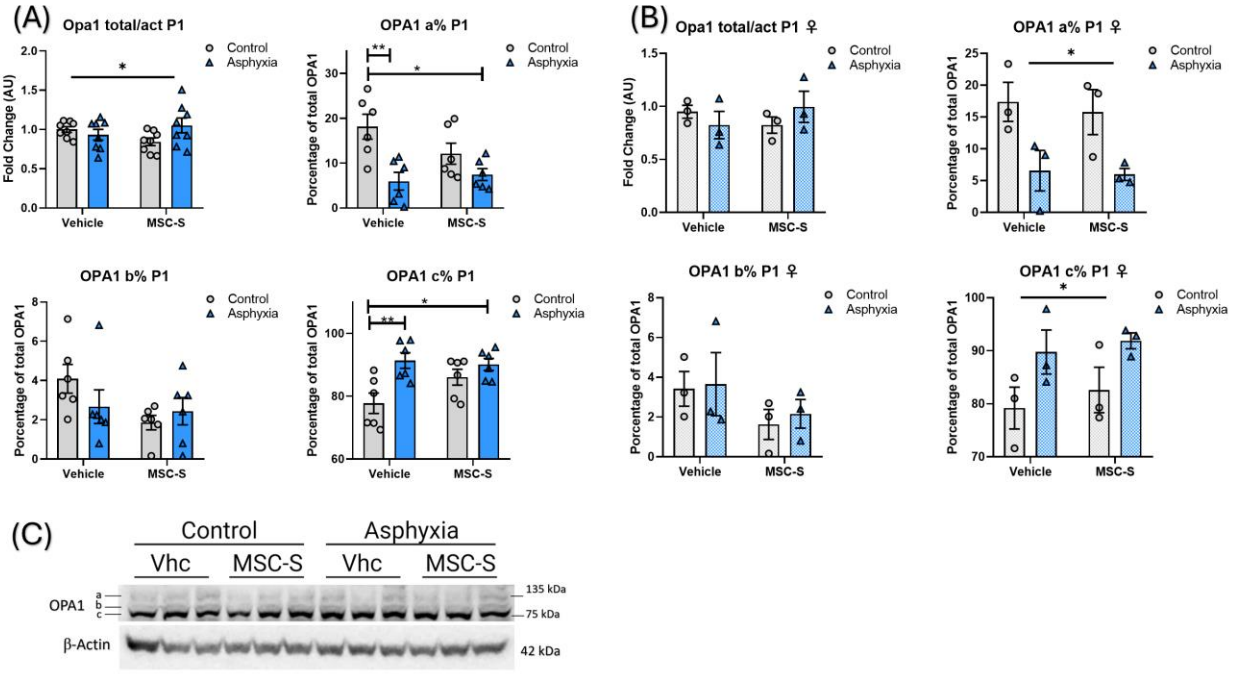

Figure 22: Fusion protein OPA1 in hippocampus at P1 following PA and MSC-S treatment. A: Total OPA1 and quantification of individual forms (a to c) at P1, and B: only female animals. C: Representative images of OPA1 Western blot membranes at P1 showing the different OPA1 forms (a to c). Data are presented as fold change relative to control levels and as a percentage of total OPA1, with β-actin as loading control, expressed as means ± SEM, C.Vhc (n=6-7), C.MSC-S (n=8), A.Vhc (n=8), A.MSC-S (n=7-8). Two-way ANOVA followed by Tukey's post-hoc test was used for statistical analysis, *p<0.05, **p<0.01. If sex is not indicated, data contain equal numbers of female and male rats (50/50 ratio).

Sex-specific changes in mitochondrial fusion proteins, at early and late neonatal stages.

OPA1 is a protein primarily found in the inner mitochondrial membrane; its primary function is to regulate mitochondrial fusion, shaping the morphology of the mitochondrial cristae. Figure 22 shows total OPA1 protein levels obtained by Western blot, normalised by β-actin. The distribution of different OPA1 cleavage patterns is expressed as the percentage of total OPA1 levels, differentiating among "a" (approx. 135 kDa), "b" (approx. 80 kDa), "c" (approx. 75 kDa), "d" (approx. kDa) or "e" (approx.. kDa) forms, according to their molecular weight, expressed differently depending upon the experimental condition and development.

At P1, there were statistically significant differences in the interaction among conditions (control or asphyxia) and treatment (vehicle or MSC-S ($F_{(1,20)}$= 4.951; P=0.0377) for total OPA1, normalised by β-actin (Fig.22).

The OPA1 "a" form levels were decreased in PA groups, either in Vhc or MSC-S treated rats, compared to the C.Vhc group (P= 0.0040 and P= 0.0118, respectively). No differences were observed in the "b" form among any of the groups. The "c" form was, however, increased in PA animals at P1 (Vhc or MSC-S treated), compared to the C.Vhc group (P= 0.0071 and P= 0.0152). When comparing among females only, OPA1 "a" protein levels were decreased in PA-exposed (A.Vhc or A.MSC-S) versus C.Vhc rats at P1 ($F_{(1,8)}$ =12.83, P=0.0072), but the "c" form was instead increased in PA animals ($F_{(1,8)}$ = 7.357, P=0.0266) (Fig.22B). No differences were observed in any of the OPA1 forms when comparing data from male animals at P1 (Annex 9).

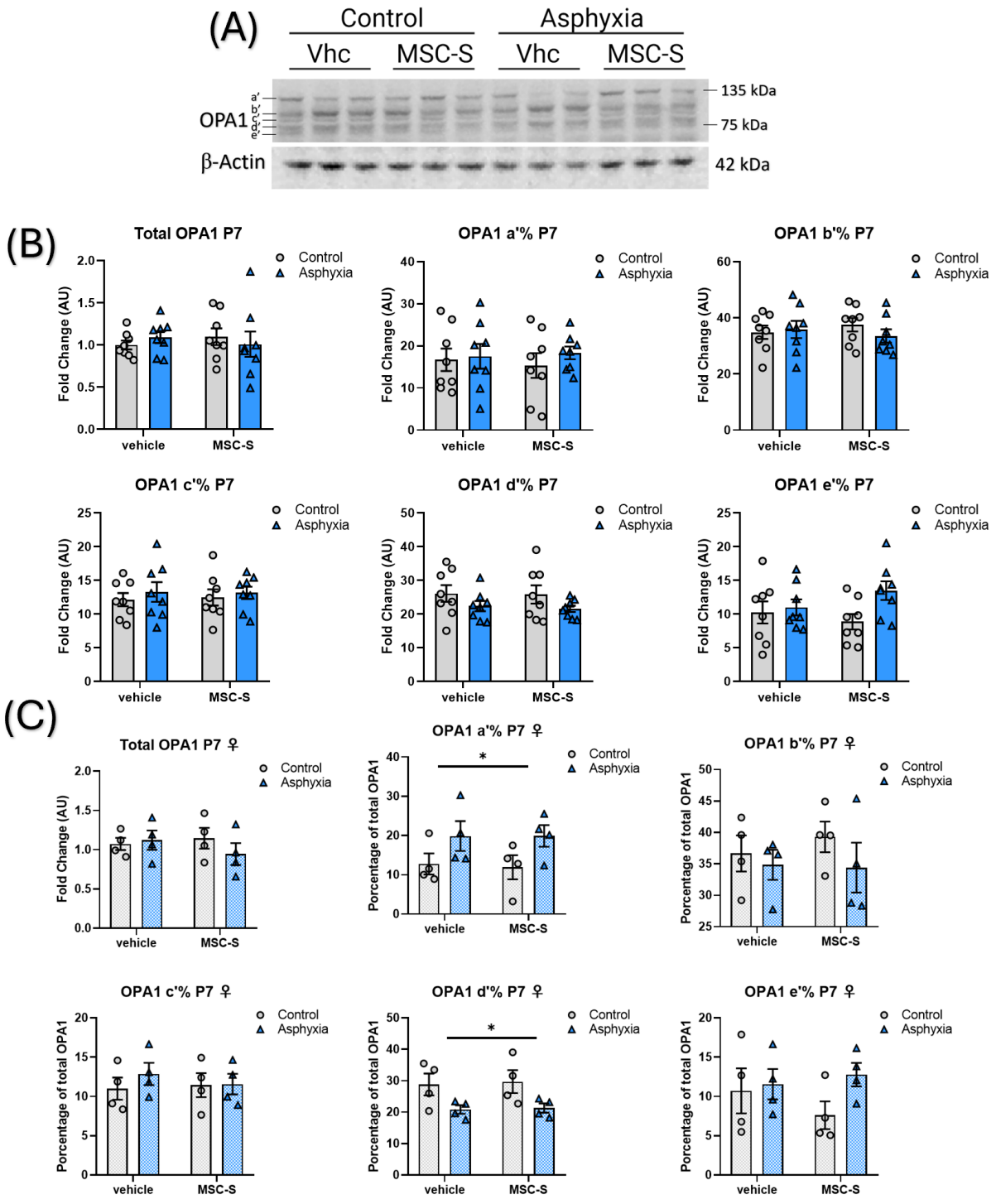

Figure 23: Fusion protein OPA1 in hippocampus at P7 following PA and MSC-S treatment. A: Representative images of OPA1 Western blot at P7 showing the different OPA1 forms (a' to e'). B: Total OPA1 and individual forms (a' to e') quantification at P7, and C: only female animals. Data are presented as fold change relative to control levels and as a percentage of total OPA1, with β-actin as the loading control, expressed as mean ± SEM, C.Vhc (n=6-7), C.MSC-S (n=8), A.Vhc (n=8), A.MSC-S (n=7-8). Two-way ANOVA followed by Tukey's post-hoc test was used for

statistical analysis, *p<0.05. If sex is not indicated, data contain equal numbers of female and male rats (50/50 ratio).

At P7, two further OPA1 forms were distinguished, but no differences were observed among the groups for total OPA1 levels or any of the forms (Fig.23). Nevertheless, when comparing among female animals, the "a" band was increased in asphyxia-exposed rats compared to the controls ($F_{(1,12)}$ = 5.917, P=0.0316) (Fig.23C). Also, there were differences in the "d" form, which was decreased in asphyxia-exposed versus control groups ($F_{(1,12)}$ = 9.144, P=0.0106).

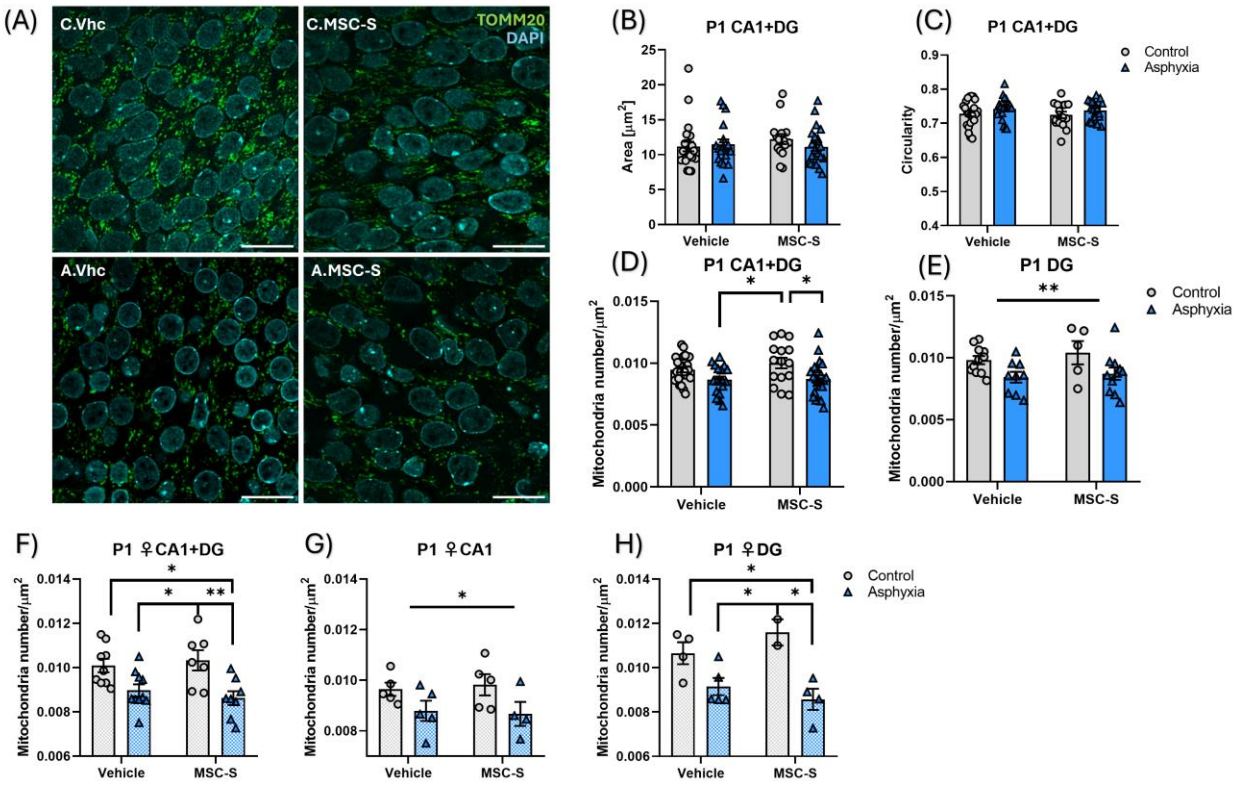

Figure 24: Mitochondrial morphology in the hippocampus at P1 following PA and MSC-S treatment. A: Representative images of mitochondria in the CA1 region of the hippocampus at P1, labelled with TOMM20 antibody (green) and DAPI (cyan). Scale bar: 10 µm. B: Mitochondrial area in µm² and C: circularity in CA1+DG. D: Mitochondria density in the CA1+DG regions and E: the DG region. F: Mitochondria density of females in CA1+DG, G: CA1 and H: DG. Data are expressed as mean ± SEM, C.Vhc (n=4-23), C.MSC-S (n=2-15), A.Vhc (n=5-18), A.MSC-S (n=4-20). Two-way ANOVA followed by Tukey's post-hoc test and Kruskal-Wallis test, followed by Dunn's post-hoc test was used for statistical analysis, *p<0.05. If sex is not indicated, data contain equal numbers of female and male rats (50/50 ratio).

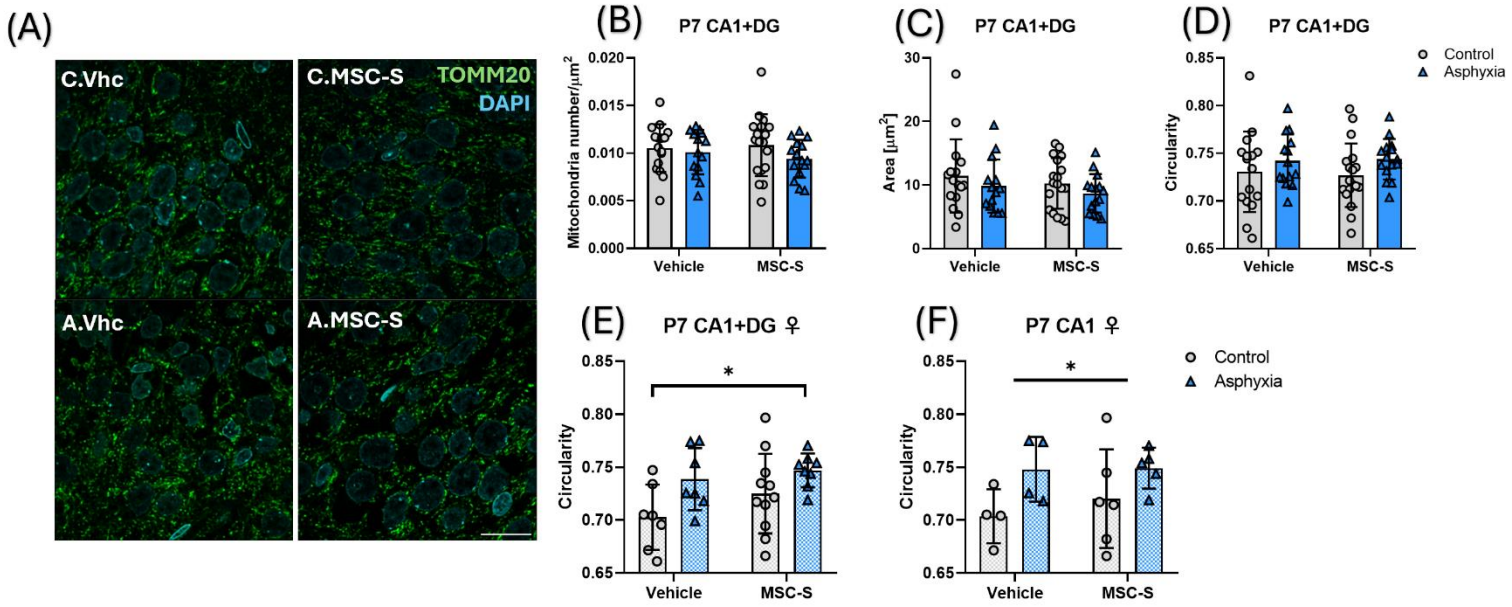

Figure 25: Mitochondrial morphology in the hippocampus at P7 following PA and MSC-S treatment. A: Representative images of mitochondria in the CA1 region of the hippocampus at P1, labelled with TOMM20 antibody (green) and DAPI (cyan). Scale bar: 10 µm. B: Mitochondrial density, C: mitochondrial area in µm², and D: circularity in CA1+DG. E: Circularity of females in CA1+DG and F: CA1. Data are expressed as mean ± SEM, C.Vhc (n=4-23), C.MSC-S (n=6-15), A.Vhc (n=4-18), A.MSC-S (n=5-20). Two-way ANOVA followed by Tukey's post-hoc test. *p<0.05. If sex is not indicated, data contain equal numbers of female and male rats (50/50 ratio).

Mitochondria morphology in hippocampus at P1 and P7.

Mitochondrial morphology was evaluated by microscopy using ExM. The tissue was expanded to visualise morphological details, and the data summarise the result of CA1 and DG, females and males unless specified. The results show a decrease in the number of mitochondria in Asphyxia-exposed animals compared to Control animals ($F_{(1, 72)}$ = 12.34, P=0.0008). Multiple comparisons revealed a difference between A.Vhc and A.MSC-S compared to C.MSC-S group (P=0.0243 and 0.0209, respectively) (Fig.24). A decrease in mitochondrial density was also seen in DG in asphyxia-exposed animals, showing differences when comparing control versus asphyxia-exposed animals ($F_{(1, 32)}$ = 9.187, P=0.0048). When segregating by sex, a decrease in mitochondrial density was observed in female A.Vhc and A.MSC-S versus C.MSC-S animals (P=0.0341 and 0.0085 respectively), and a decrease when A.MSC-S were compared with C.Vhc (P=0.0170) animals. In CA1, the females showed differences among the conditions (Control versus Asphyxia) ($F_{(1, 16)}$ = 6.287, P=0.0233), and in DG, there was a decrease in A.Vhc and A.MSC-S compared to C.MSC-S (P=0.0390 and 0.0139 respectively), and decrease in A.MSC-S compared to C.Vhc

(P= 0.0373). No differences were observed in males' mitochondrial density, neither in area nor circularity (Annex10).

At P7, the same morphological parameters were analysed. No differences were observed in morphology among the groups at P7 (Fig.25), however, when segregating the results by sex, there was an increase in mitochondrial circularity in asphyxia-exposed animals compared to control in the female data ($F_{(1, 29)} = 7.235$, P=0.0117), specifically in CA1 region ($F_{(1, 15)} = 5.410$, P=0.0345).

Differences were observed when evaluating CA1 and DG regions in C.Vhc versus A.Vhc. There was a decrease in mitochondrial area in DG versus CA1. Specifically, when comparing CA1 versus DG in C.Vhc animals (P=0.0293) and CA1 versus DG when comparing C.Vhc versus A.Vhc (P=0.0337) (Fig.24).

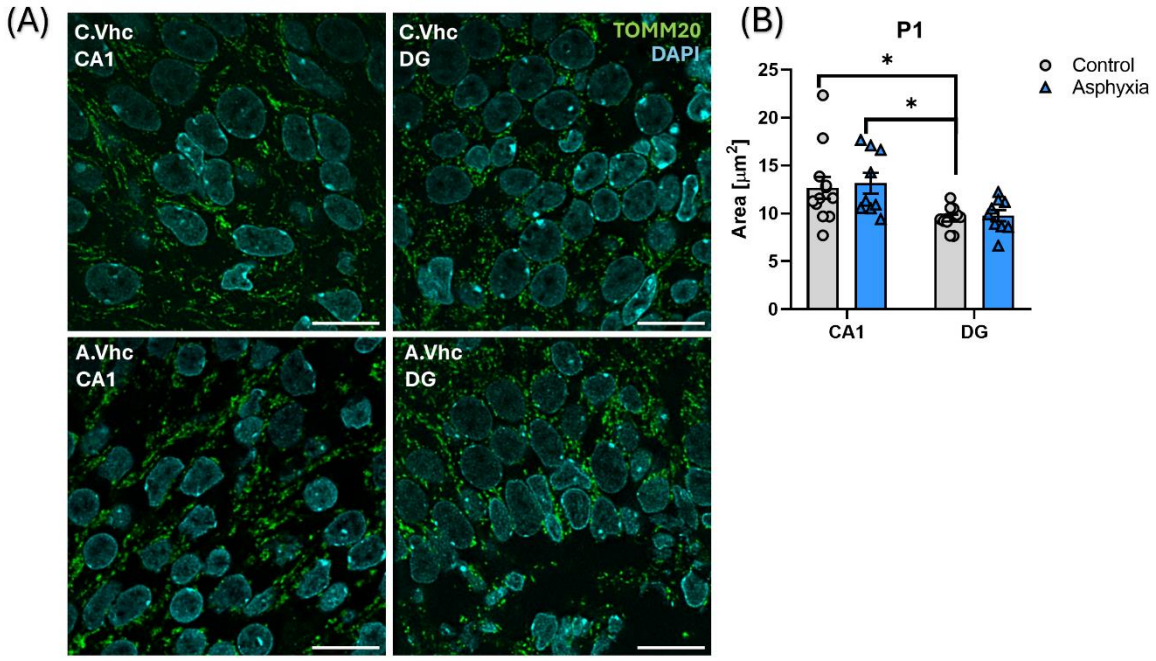

Figure 26: Comparison of mitochondria morphology between the CA1 and DG regions in the hippocampus following PA at P1. Representative images of mitochondria in the CA1 and DG region of the hippocampus at P1, labelled with TOMM20 antibody (green) and DAPI (cyan). Scale bar: 10 µm (A). Quantification of mitochondria area in µm² of C.Vhc and A.Vhc animals in CA1 and DG at P1 (B). Data are expressed as mean ± SEM, C.Vhc (n=4-12), A.Vhc (n=4-9). Two-way ANOVA followed by Tukey's post-hoc test was used for statistical analysis, *p<0.05. If sex is not indicated, data contain equal numbers of female and male rats (50/50 ratio).

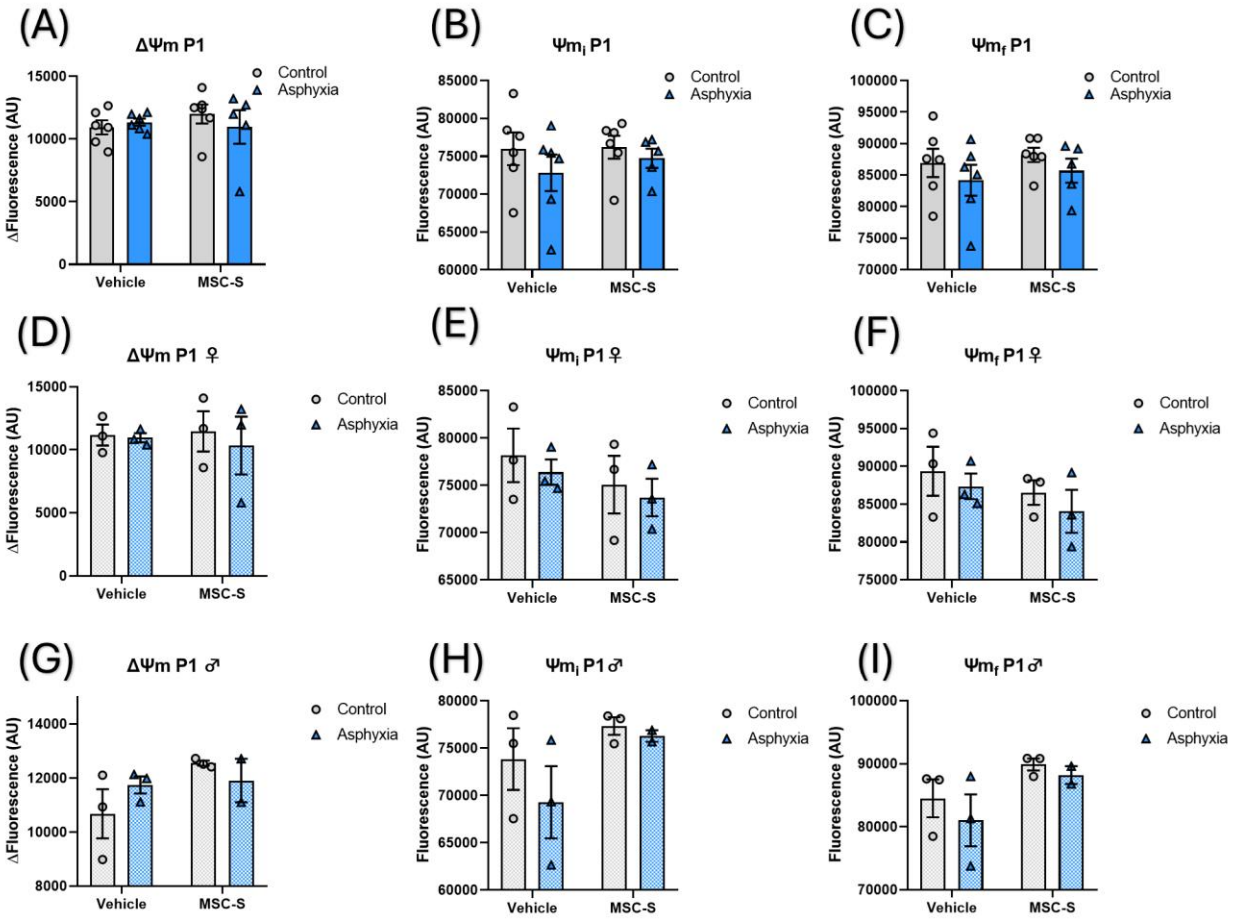

Figure 27: Mitochondrial membrane potential in brain homogenates at P1 following PA and MSC-S treatments. A: Difference between final and initial mitochondrial membrane potential at P1, D: in females and G: males. B: Initial mitochondrial membrane potential at P1, E: in females and H: males. C: Final mitochondrial membrane potential at P1, F: in females and I: males. Data are expressed as mean ± SEM, C.Vhc (n=4-12), A.Vhc (n=4-9). Two-way ANOVA followed by Tukey's post-hoc test was used for statistical analysis. If sex is not indicated, data contain equal numbers of female and male rats (50/50 ratio).

Mitochondrial Membrane Potential in brain mitochondria at P1 and P7

As a functional measurement of mitochondria, membrane potential was evaluated in brain homogenate lacking the frontal pole. The initial and final membrane potential was quantified, using FCCP for mitochondrial uncoupling. The difference between the final and initial membrane potential was also measured. Results at P1 show no difference among the groups or any sex-specific effect. (Fig.27). However, at P7 a difference was observed at the initial membrane potential, with an increase in fluorescence in A.Vhc and A.MSC-S compared to C.MSC-S (P=0.0186 and P=0.0247). A difference was also observed in the final membrane potential, showing a decrease in C.MSC-S compared to A.MSC-S animals (P=0.0425). Differences in the two-way ANOVA, column factor (control versus asphyxia) ($F_{(1, 9)}$=6.310, P=0.0332) were observed in asphyxia-exposed groups, showing

increased fluorescence levels compared to the control groups, but without reaching the statistically significant level evaluated by multiple comparisons (Fig.28).

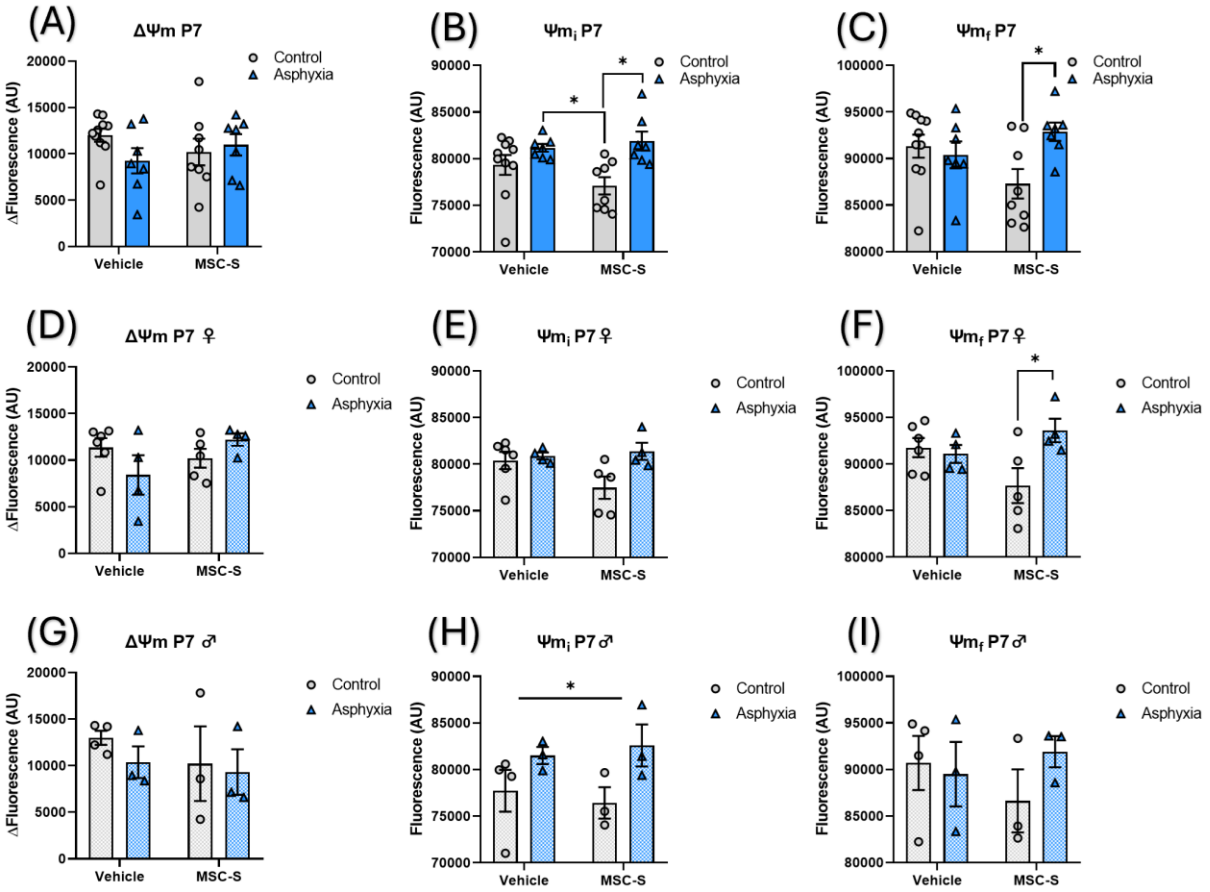

Figure 28: Mitochondrial membrane potential in brain homogenates at P7 following PA and MSC-S treatment. A: Difference between final and initial mitochondrial membrane potential at P7, D: in females and G: males. B: Initial mitochondrial membrane potential at P7, E: in females and H: males. C: Final mitochondrial membrane potential at P7, F: in females and I: males. Data are expressed as mean ± SEM, C.Vhc (n=4-12), A.Vhc (n=4-9). Two-way ANOVA followed by Tukey's post-hoc test was used for statistical analysis, *p<0.05. If sex is not indicated, data contain equal numbers of female and male rats (50/50 ratio).

Chapter 4: Discussion

Perinatal asphyxia induces a hypoxic condition. In the present model of PA, asphyxia induces a decrease in survival by approximately 50%. 40 minutes after birth, asphyxia-exposed and control animals are assessed by an Apgar scale [89]. The results show a clear difference between control and asphyxia animals, respiratory frequency, spontaneous movements of their limbs, skin colour and vocalisation are significantly lower in asphyxia compared to control animals (Fig.5A-E). Moreover, asphyxia animals gasp, unlike control animals, absent apart some few gasping immediately after delivery (Fig.5F). Survival and the different Apgar parameters do not differ between sexes (Annex1), contrary to what is known in humans, where males have a lower survival rate than females [90]. The only observed difference between sexes was the birth weight, males outweighing females, but only in the control cohort (data not shown).

Lactate, primarily known and associated with hypoxia-ischemia, is now recognised for its physiological function. It is predominantly formed by astrocytes from glucose or glycogen and transferred to neurons to meet their energy demands and homeostatic functions [91]. The results indicate a marked increase in lactate levels in asphyxia-exposed animals, compared to control, an increase that is observed from 5 minutes to 4 hours after the insult, confirming the physiological effect induced by asphyxia (Fig.6), in agreement with previous studies [53]. The differences were no longer evident 24 hours after the insult. Elevated lactate levels in blood at 6 hours of age have been shown as a predictor of adverse outcomes in asphyxia-exposed infants undergoing therapeutic hypothermia [92]. This increase in lactate levels is attributed to a shift from aerobic to anaerobic metabolism, which can exacerbate cellular damage by promoting acidosis, oxidative stress, and inflammation, further compromising the mitochondrial redox state and impairing the function of the electron transport chain (ETC) complexes, leading to mitochondrial dysfunction, exacerbating the cellular injury induced by PA [93]. When comparing the results segregating by sex, no differences were observed between females and males in the pattern of lactate levels observed when comparing control and asphyxia-exposed groups, biologically there appears to be no obvious difference in blood lactate levels over time (Annex 2).

To evaluate Nrf2 activation following PA and secretome administration, both total and nuclear Nrf2 levels were measured by immunofluorescence in CA1 and DG of hippocampus, regions known as vulnerable to PA [10]. No differences were observed in total or nuclear Nrf2 levels at P1 and P7. However, at P14, total Nrf2 levels were increased in asphyxia-exposed compared to control groups. In agreement, nuclear Nrf2 was also increased in asphyxia-exposed, compared to control animals in DG and CA1+DG, indicating nuclear Nrf2 translocation. In both cases, the observed increase could be attributed to asphyxia, but not to the treatment.

However when analysing mRNA levels of Nrf2 effectors, a transient and delayed activation of the Nrf2 pathway upon administration of MSC-S was observed, reflecting an increase in mRNA levels of Nrf2 effectors, independently upon their conditions (control or asphyxia). At P1 only prdx showed an increase in the A.MSC-S group, but at P7, all Nrf2 effectors increased with the MSC-S treatment, except for Nrf2 itself. However, at P14, the effect of MSC-S was no longer evident, suggesting that the pathway had returned to baseline levels.

Protein levels of the Nrf2 effectors GSR and NQO1 were elevated in the A.Vhc group at P7, a phenomenon that was reversed to control levels in the A.MSC-S group. However, at P14, contrary to that observed at P7, GSR protein levels were decreased in saline and MSC-S asphyxia-treated groups, compared to the control groups. It is notable that at P14 the asphyxia-exposed groups showed a decrease in GSR levels at protein level, but an increase at mRNA level. A.Vhc showed an increase in gsr levels, in both asphyxia groups, also in gclc levels. At P14 the effect on Nrf2 levels agreed with an increase in Gclc and gsr mRNA levels, independent of the treatment condition, suggesting an upregulation as a response to a decrease in GSR protein levels since Gclc encodes for the glutamate-cysteine ligase catalytic subunit, the first-rate limiting enzyme for glutathione synthesis [94], and gsr encodes for glutathione reductase, which catalyses the reduction of GSSG to GSH [94]. Therefore, further investigation on the role of glutathione metabolism at P14 after PA would be a subject for future studies.

The results concerning Nrf2 activation measured by monitoring mRNA levels of Nrf2 effectors with RT-qPCR did not correlate with those obtained by measuring protein levels with Western blot. This discrepancy may be attributed to various factors, such as different regulatory mechanisms involved in the translation of mRNA to protein, inherent variability between the animals, or variations in the timing of protein and mRNA expression [95]. The differential response between mRNA and protein levels further highlights the complexity of the regulatory mechanisms involved in the Nrf2 pathway. It underscores the need for further investigation to fully understand the underlying processes.

To evaluate whether MSC-secretome targeted the Nrf2 pathway when eliciting antioxidative effects, as suggested by previous findings [76], an ASO against Nrf2 was constructed. This evaluation was performed with asphyxia-exposed animals only, administering the secretome 24 hours after birth, 24 hours were required for ASO to perform transcriptional repression of Nrf2 (Annex3). Thus, caution should be considered when interpreting these results, required to exert an effect. Using RT-qPCR, mRNA levels of selected Nrf2 effectors were measured. Indeed, the ASO-Nrf2 decreased the levels of the effectors (gclc, prdx, ho1). However, no effects of the ASO-Nrf2 were observed in MSC-S treated groups. When measuring the GSSG/GSH ratio, no differences were observed among the groups. However, there was a trend for a decrease, observed in Asphyxia-MSC-S/ASO treated, compared to the A.Vhc group. Nevertheless, it was found

that ASO-Nrf2 decreased the effectors of the Nrf2 pathway, but the effect of MSC-S was maintained. Taken together, these results might imply that the involvement of the Nrf2 pathway is not essential for the antioxidative effects induced by MSC-S. Further investigation is required to understand the underlying mechanisms clarifying the interplay between the Nrf2 pathway and the observed effects of MSC-S treatment.

The results concerning Nrf2 activation and cell death were not segregated by sex initially but considering the relevance of sexual dimorphism in mitochondrial parameters reported in the literature, the data were subsequently analysed accordingly.

Oxidative stress in the PA model has been evaluated before, showing increased and sustained oxidative stress in mesencephalon and hippocampus of rats exposed to PA up to P14 [96]. However in this study it was not possible to replicate the previous results, only finding a significant difference at P1 in the asphyxia-exposed groups, and in A.Vhc females at P7. The impossibility of replicating these results could be attributed to differences in the techniques used to quantify oxidative stress.

Regarding cell death, at P1 and P7, levels of apoptotic cell death were elevated in asphyxia-exposed animals as expected, as delayed cell death is one of the endpoints to be evaluated in PA [89]. Apoptotic cell death was higher in the CA1 versus the DG region. This difference could be explained by the difference in the calcium buffering capacity of the two zones. DG has a higher calcium buffer capacity [97], [98] due to higher levels of calcium-binding protein calbindin, which confers protection against excitotoxicity induced by hypoxic conditions [97]. At P14, apoptotic cell death tended to be higher in the asphyxia-exposed groups, but it did not reach the level of statistical significance (Fig.10) in contrast to previous findings [10], [96]. Necrosis or other types of cell death were not evaluated, since the main type of cell death found in AP models is apoptosis, no alterations were found in histological evaluations, such as shrinkage, swelling and membrane lysis, more typically related to necrosis [89], although it is not ruled out that in the first hours of the insult could occur.

Mitochondrial mass was evaluated in hippocampus at P1 and P7, using qPCR for monitoring D-loop, a non-coding region of the mitochondrial genome, crucial for mtDNA replication and transcription [99], a suitable target for evaluating mitochondrial mass. It was found that there was a decrease in D-loop levels in the hippocampus of asphyxia-exposed rat neonates at P1, but not at P7. The effect of asphyxia was normalised by MSC-S administration 2 hours after birth. This result suggests that PA affects mitochondrial biogenesis and/or accelerates the mitophagy process, decreasing mitochondria density in the hippocampus at an early period after PA.

The mitochondrial biogenesis regulators PGC-1α and TFAM were also monitored by RT-qPCR to verify changes in mitochondrial biogenesis [100], [101]. These regulators of mitochondrial biogenesis were shown to be increased 6 to 24 hours after a HI insult performed at P7 [51]. Nevertheless, no differences were observed here at P1 and P7

(Annex 5), suggesting that the effect of PA on PGC-1α and TFAM has to be explored at shorter times since it has been reported that mitochondrial biogenesis increases at 6 hours and up to 24 hours after an H-I insult as a possible reparatory mechanism in rats at P7 [51].

An increase in Drp1 levels was also observed, a fission mitochondrial protein whose expression is elevated during stress and apoptosis [102]. Drp1 levels were elevated at P1 but not at P7. Interestingly, Fis1, an adaptor for the recruitment of Drp1, was increased at P7 but not at P1. Fis1 has not been shown to affect Drp1 subcellular distribution, but it promotes mitochondrial fragmentation [36]. Evidence suggests that Fis1 may be implicated in stress-induced fission mitophagy [103]. The increase in Fis1 protein levels observed at P7, an effect normalised by MSC-S administration, could indicate increased mitochondrial fission in A.Vhc animals.

The post-translational modifications of Drp1, specifically the phosphorylation at Ser616 and Ser637, were analysed by measuring pDrp1 levels, normalised against total Drp1, at P1 and P7. Phosphorylation of Drp1 at Ser616 is considered as a key indicator of mitochondrial fission [32], [42]. However, no differences were found at P1 or P7 among the two pDrp1 monitored variants. The absence of differences in this marker may suggest a stable fission activity (Annex 8).

OPA1 is a protein found in the inner mitochondrial membrane, whose primary function is to regulate mitochondrial fusion, shaping the morphology of the mitochondrial cristae [42]. Several OPA1 cleavage patterns can be differentiated according to molecular size, mediated by two proteases, the ATP-dependent metalloprotease YME1L and a m-AAA protease, OMA1, yielding fragments that can be differentiated according to molecular size. YME1L cleaves constitutively OPA1 to maintain a balance among the forms, overlapping with OMA1, both proteases are found in rat brain [104]. OPA1 cleavage yields L-OPA1 (higher molecular weight and insoluble), which is, in turn, cleavaged to S-OPA1 (lower molecular weight and soluble) under stress conditions [33], [105].

In the present study, we differentiate among three forms of OPA1 at P1 (a, b and c) and five forms at P7 (a', b', c', d' and e'). It was found that OPA1 "a" (highest molecular weight or L-OPA1) levels were decreased, while OPA "c" (lowest molecular weight at P1 or S-OPA1) levels were increased in hippocampus of asphyxia-exposed neonates at P1. No differences among the groups were observed for the "b" form. The relevance of these changes is not entirely clear. An increase in L-OPA1 has been associated with an increase in mitochondrial fusion, while an increase in S-OPA1 forms has been associated with an increase in mitochondrial fission [29]. At P7, five different OPA1 forms were observed, whose activation could be segregated by sex; it was found that OPA1 " a' " levels were increased, while OPA1 " d' " levels were decreased in female subjects.

Differences in mitochondrial morphology were further evaluated by ExM microscopy. A decrease in mitochondria density was observed at P1 in asphyxia-exposed animals,

whether CA1 and DG regions were analysed together or separately. The effect was magnified when segregating by sex, observing a decreased mitochondria density in CA1 and DG of female asphyxia-exposed subjects evaluated at P1. The decrease in mitochondria density did not imply an increase in the analysed mitochondria area. This result is consistent with the finding of a decrease in mitochondrial mass (D-loop) shown in Fig.19 and agrees with the results of [47], where the mitochondrial mass is decreased in females.

The decrease in mitochondrial density, especially in females, could be related to increased mitophagy, since in postnatally (P7) HI-exposed animals, there was an increase in mitophagy after 24 hours post-insult in female animals, which could be protective. Additionally, the same study suggests that a deficit in mitophagy in males could be related to male vulnerability to HI insults [49]. Furthermore, it has also been reported that mitophagy exhibited dual peaks, both at 3 hours and postnatal day 7 following HI injury. In that study, it was hypothesised that the first peak is related to a secondary energy failure induced by the HI insult. The second peak related to a repair process after HI [106]. Therefore, the decrease in mitochondrial mass and mitochondrial density could be a protective reaction to PA, generated by an increase in mitophagy, which is a parameter that remains to be explored in this model and will be important to address for a better understanding of the phenomenon.

Changes in OPA1 could be related to mitochondrial cristae, as mentioned above, but not due to an increase in mitochondrial fission or fusion, since OPA1 actively participates in the crista junction (CJ) maintenance [31]. Changes in the morphology of the mitochondrial cristae observed in the hippocampus could also be associated with energy production [28], [30]. It was observed that the percentage of OPA1 fragments was different at P1 and P7 in control rats, suggesting that the cristae organisation and dynamics change along with neurodevelopment. Indeed, the observed increase in Drp1 levels at P1 could be related to an increase in mitophagy, since a Drp1-dependent mitophagy is protective [107], [108], [109].

Furthermore, when combined with the expansion microscopy analysis, differential effects were observed in CA1 and DG hippocampal regions, known for their distinct functional roles across development and differential vulnerability [110]. These regional differences in response to PA contribute to the different outcomes observed with the Western blot analysis. Since results from Western blot represent a homogenate of the whole hippocampus, it potentially masks region-specific effects elucidated by ExM. The DG showed a lower mitochondria area than hippocampus's CA1 at P1, indicating that the mitochondria are smaller in DG. At P7, the mitochondrial density of DG was decreased compared to CA1.

In mammals, neurogenesis starts at prenatal stages, and continues throughout adulthood. Indeed, the DG is one of the neurogenic zones that remains active throughout the adult brain [111]. Neuronal stem cells (NSCs) are located in the subgranular zone, producing

new neurons in an outside-in pattern to the granule cell layer (GCL) of the DG. Neurons tend to present a mitochondrial elongated morphology during development and are wider and highly elongated in the adult hippocampus [112]. Maturation of mitochondria has been reported to change during neurogenesis [113], showing a metabolic shift from glycolysis to OXPHOS to enhance bioenergetic capacity [113]. In agreement, it has been shown that mitochondrial mass and mtDNA increase along neuronal maturation [114].

Mitochondrial membrane potential was assessed using safranine O as a functional measure of mitochondria. Interestingly, no difference among the groups or any sex-specific effect was observed at P1. However, a difference was found at P7, where both groups exposed to asphyxia showed an increase in the initial mitochondrial membrane potential fluorescence compared to control groups (Fig.27). This study employed a quenching mode probe approach to measure mitochondrial membrane potential, where a lower membrane potential results in a higher fluorescence intensity. Therefore, the result indicates that asphyxia-exposed male animals have lower mitochondrial membrane potential than controls. This finding suggests that mitochondria in males have a reduced capacity to produce ATP or that it represents a protective mechanism against the consequences of PA. Mitochondria reduce their activity to produce lower ROS levels [115]. This interpretation aligns with previous observations, where asphyxia-exposed females at P7 showed higher oxidative stress, but the males did not (Fig.7).

Clinical studies have indicated that neonatal female brains exhibit greater resistance to the consequences of neonatal hypoxia compared to males, leading to better long-term cognitive outcomes despite similar brain injuries, suggesting a sex-specific mechanism for neuroprotection [116]. However, the molecular mechanism underlying these sex-specific differences remains unclear, with various factors potentially contributing to this phenomenon, including genetics, immunological, and hormonal dynamics [117]. Animal models of HI have shown an upregulated immune response leading to increased microglial activation in males [117], [118]. Additionally, evidence suggests that testosterone can enhance neurotoxicity, while oestrogens protect the brain following HI insults [119]. Testosterone levels peak at gestational weeks 10-20 and remain elevated during the first year of life, which could contribute to the higher mortality observed in males. In a rat model using testosterone propionate (TP), investigators found that both males and females HI-exposed and treated with TP showed impairments in auditory processing [119].

In a mouse postnatal insult (P9) model, the female hippocampus of rodents exposed to HI increased the expression of Oestrogen Receptor alpha (ERα) at mRNA and protein levels, decreasing apoptosis and increasing the phosphorylation of the Tropomyosin receptor kinase B (TrkB), compared to the sham control. Activation of TrkB ligand demonstrates neuroprotective properties against HI, as evidenced by the use of TrkB ligand, whose effect was lost in an ERα-null mouse [120]. Indeed, the apoptotic pathway differs depending on the neonate's sex. The caspase-independent pathway seems to predominate

in males, characterised by decreased NAD levels, PARP-1 activation, AIF, and EndoG release. In females, a caspase-dependent apoptosis pathway seems to predominate, which involves APAF-1 and the formation of an apoptosome, together with caspase activation [116].

Regarding treatment, it has been shown that intracerebroventricular (i.c.v) administration of neuronal stem cells (NSC)-derived secretome improves mitochondrial dysfunction [121]. NSC-S has been shown to normalise levels of mitochondrial dynamics proteins in vitro and in vivo models of 6-OHDA Parkinson's, suggesting a role for the Sirt1 pathway [121]. Notably, secretome from neural-induced human adipose tissue-derived stem cells (NI-ADSC-S) was capable of restoring mitophagy and dynamics basal levels in an in vitro model using rotenone [122]. In the present study, intranasal secretome administration was capable of normalising the levels of D-loop and Drp1 at P1 and Fis1 at P7 but did not affect other parameters affected by asphyxia, such as changes in OPA-1 or mitochondria density, suggesting that the secretome is only capable of restoring certain pathways affected by PA. Interestingly the proteins that were capable of normalising are related to mitochondrial fission proteins. However, many differences in the secretome, from the source of stem cells to the culture condition and preconditioning, can influence the pattern of secreted molecules and, therefore differ in the mechanism of action [66].

The present study has several limitations that should be addressed in future research. In some cases, such as Nrf2 activation and cell death quantification the sample size prevents us from separating the results by sex and assessing a possible sex effect. Additionally, only two periods of time were evaluated in the case of mitochondrial parameters, future work should utilise shorter and/or longer times to evaluate the chronology of the events and determine to what level these parameters are affected by PA. Moreover, about the treatment used in this work, administration at different periods and the administration of more than one dose could also be evaluated. As for the techniques used, although mitochondrial morphology could be evaluated by combining immunofluorescence and ExM, it is known that the best way to evaluate it is through electron microscopy, which could not be used on this occasion, as it is more resolute and the interaction of the mitochondrion with the endoplasmic reticulum (ER) can be evaluated. The ER and mitochondria are closely associated cellular structures forming numerous contact points. These areas where the two organelles interact are known as mitochondria-ER contact sites or MERCSs, these regulate lipid synthesis, calcium homeostasis and mitochondrial dynamics [123]. During hypoxia MERCSs coordinate cellular response, they serve as a platform where constriction events, necessary for mitochondrial fission and subsequent mitophagy occur, ensuring that damaged mitochondria are efficiently removed and that mitochondrial function is preserved, by preventing the accumulation of ROS and cellular damage [123].

Overall, these findings highlight the complexity of the therapeutic effects of secretome derived from preconditioned MSCs and underscore the need for further research to

elucidate its mechanisms of action and to optimise its therapeutic potential in mitigating the effects of perinatal asphyxia.

A.11. Conclusions

The findings show that PA decreases mitochondrial mass in the hippocampus at P1, as evidenced by reduced mtDNA content. Furthermore, we observed changes in mitochondrial dynamics protein levels, observing increases in fission proteins, Drp1 at P1 and Fis1 at P7, and altered fusion protein OPA1 isoform expression at P1 and P7. Also, PA decreased initial mitochondrial membrane potential compared to controls in male animals.

Sex-specific differences were identified in response to PA. Female PA-rats exhibited altered OPA1 expression at P1 and P7, suggesting a potential upregulation of mitochondrial fission at P1 and increased fusion at P7, whose impact on mitochondrial bioenergetics requires further studies. Treatment with secretome-derived from preconditioned human MSCs normalised fission proteins to control levels, but did not modify the effect of PA on OPA1 levels, at P1 or P7, nor on mitochondrial density.

These findings contribute to our understanding of the pathophysiology of PA and emphasise the importance of considering sex as a biological variable. Future research should focus on unravelling the molecular mechanisms behind these sex-specific differences.

Chapter 5: Annex

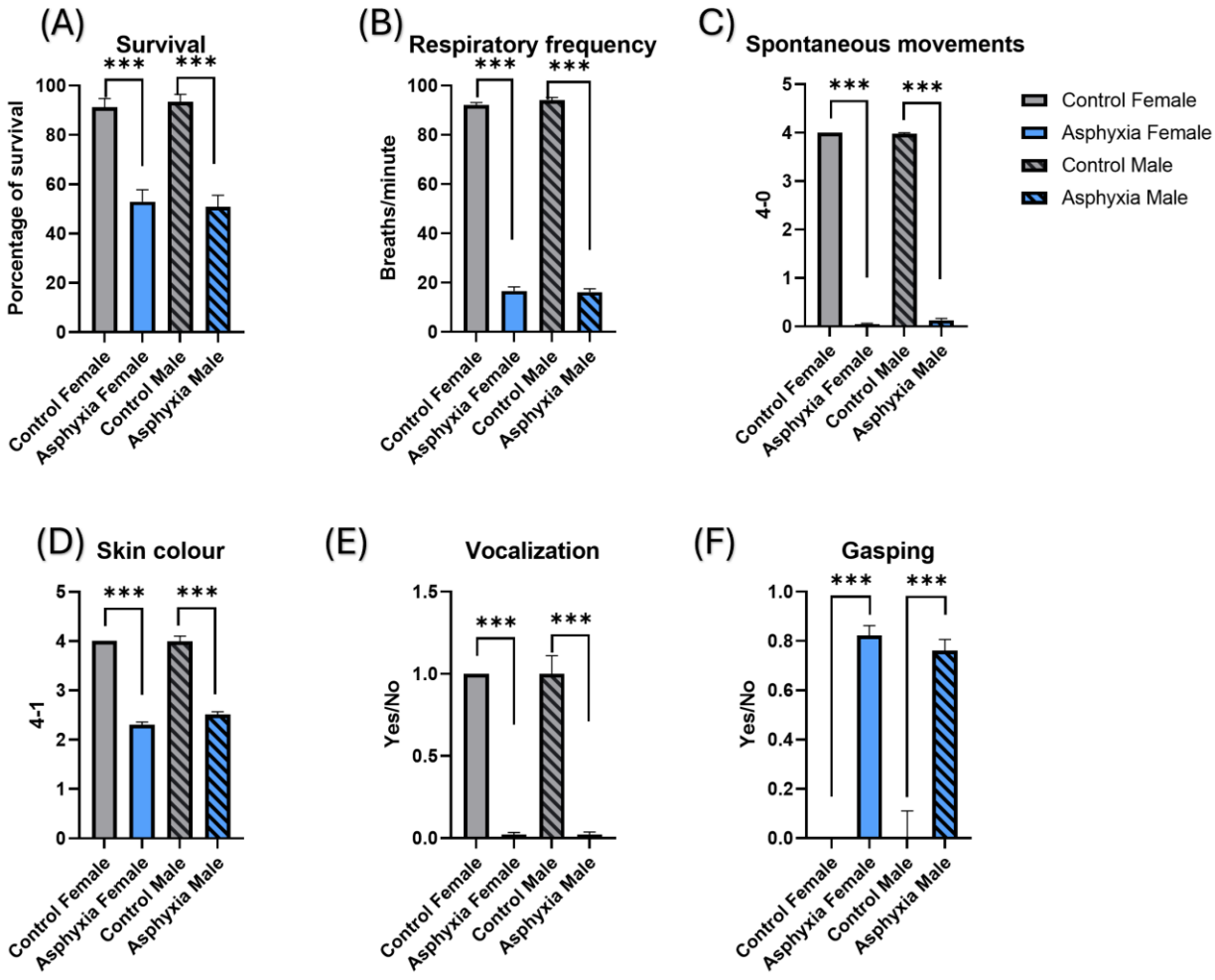

Annex 1: Apgar evaluation after 40 minutes of birth, segregated by sex. A: Survival as a percentage of survival. B: Respiratory frequency in breaths/minute. C: Spontaneous movements (4: movement of the 4 limbs, 0: no movement). D: Skin colour (4: pink, 3: bluish pink, 2: pinkish blue and 1: blue). E: Presence of vocalisation. F: Presence of gasping. Data are expressed as means ± SEM, C.Vhc (n=46-48), A.Vhc (n=50). One-way ANOVA, Tukey's post-hoc test ***p <0.0001.

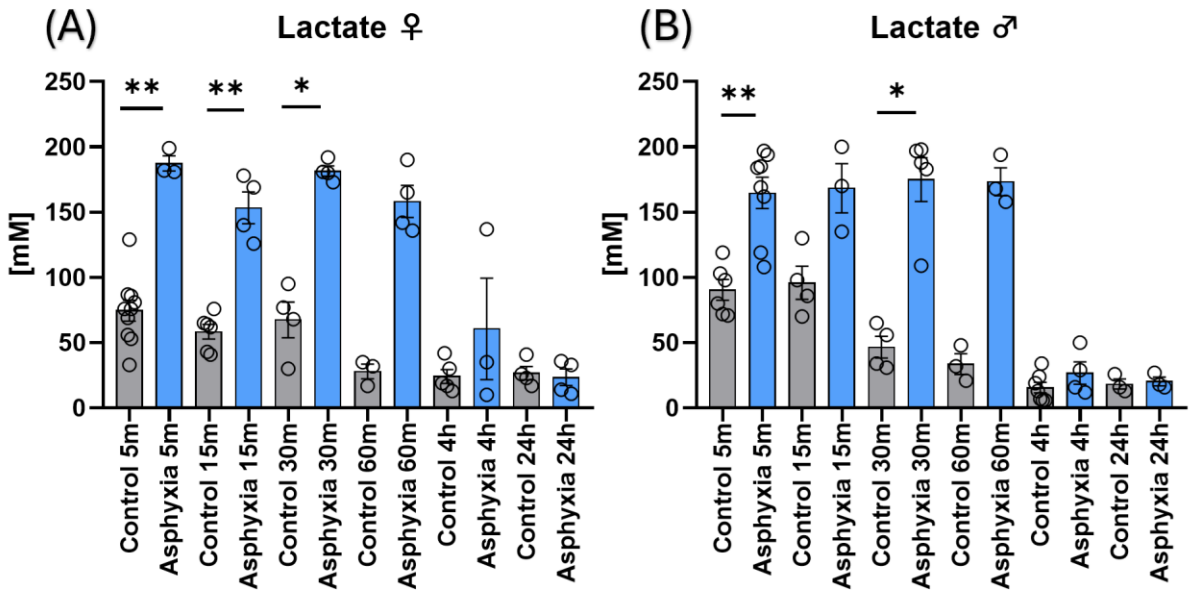

Annex 2: Lactate in blood, segregated by sex. Results are presented as mM. Data are expressed as means ± SEM, C.Vhc (n=3-16), A.Vhc (n=3-10), at different time points, from 5 minutes to 24 hours. Mann-Whitney, *p<0.05, **p<0.01.

Use of an antisense oligonucleotide (ASO) against Nrf2 to inhibit the signalling pathway.

To evaluate the Nfr2 targeting and the action mechanism of intranasal mesenchymal stem cell-derived secretomes, we used an ASO against Nrf2. One hour after birth, an ASO or scrambled sequence (Scr) was administered to neonates by an intracerebroventricular (i.c.v.) injection. 24 hours after delivery, 16 µL of DFX-preconditioned MSC-S or saline were administered intranasally to PA-exposed rats. Annex, the effect of the ASO or scramble sequence on qRT-PCR results is shown. A decrease in gclc (P=0.0002), HO1 (P= 0.0306 and 0.0261) and prdx (P=0.0002) mRNA levels in ASO-groups were found, compared to the Scr-groups, used as controls. The difference in Nqo1 mRNA levels did not reach a significant level (P= 0.0616) compared to the Scr-treated group, although a similar trend was observed for other effectors.

To evaluate the effects of the ASO-Nrf2 on oxidative stress, the GSSG/GSH ratio was analysed. The GSSG/GSH ratio did not reach any significant difference (P=0.0697), although a diminution trend was observed in the MSC-S condition.

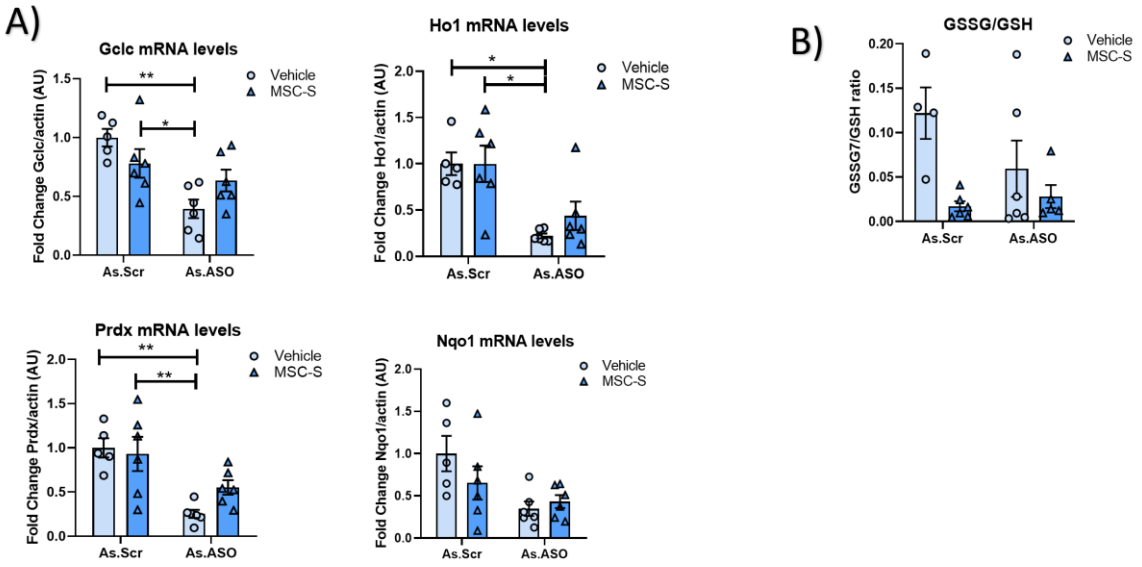

Annex 3: Effects of Nrf2 ASO on PA and MSC-S treatment. A: RT-qPCR analysis of Nrf2 gene effectors Gclc, Ho1, Prdx and Nqo1 at P7 and B: GSSG/GSH ratio. Results are presented as a fold of change relative to A.Scr/Vhc levels. Data are expressed as means ± SEM. A.Scr/Veh (n=4-5), A.Scr/MSC-S (n=6), A.ASO/Vhc (n=6), A.ASO/MSC-S (n=5-6). Two-way ANOVA, followed by Tukey as a post-hoc test, *p<0.05, **p<0.01.

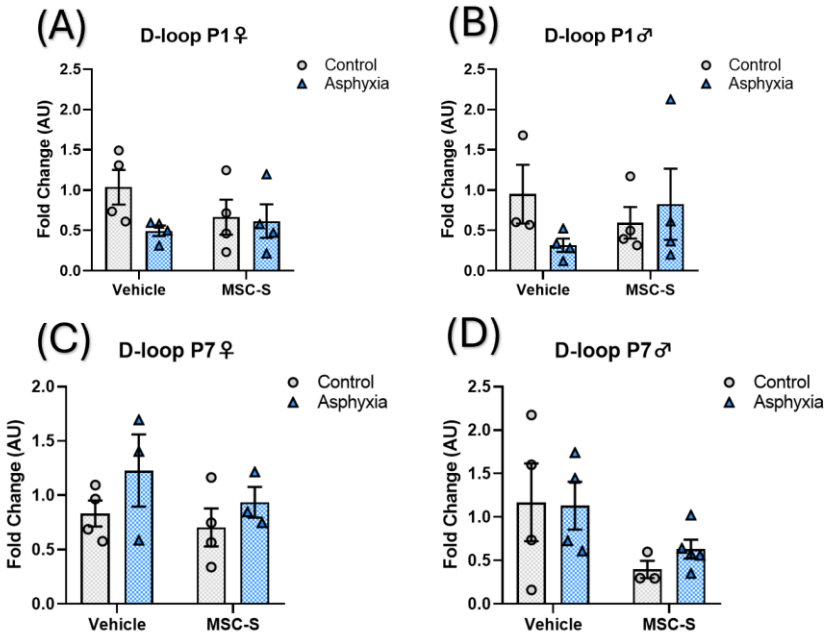

Annex 4: Mitochondrial DNA content in hippocampus at P1 and P7 segregated by sex, following PA and MSC-S treatment. Female D-loop quantification A: at P1 and C: at P7. Male D-Loop quantification B: at P1 and D: at P7. Data are presented as fold change relative to control levels, expressed as mean ± SEM, C.Vhc (n=3-4), C.MSC-S (n=3-4), A.Vhc (n=3-4), A.MSC-S (n=3-5). Two-way ANOVA followed by Tukey's post-hoc test.

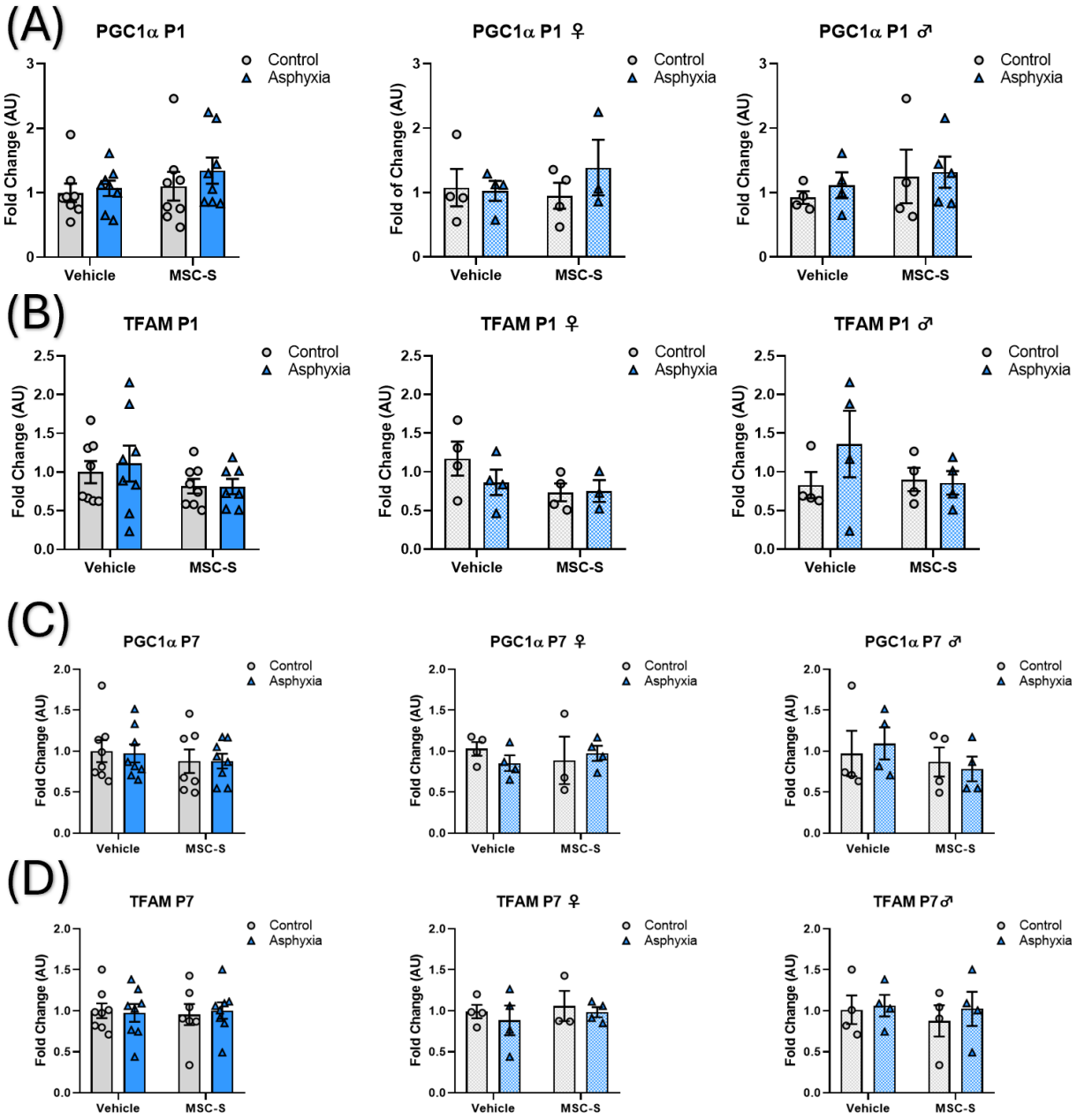

Annex 5: Mitochondrial biogenesis at P1 and P7 following PA and MSC-S treatment. Quantification of PGC1α A: at P1 and C: P7, and TFAM B: at P1 and D: P7, segregated by sex on the right. Data are presented as fold change relative to control levels, expressed as mean ± SEM, C.Vhc (n=4-8), C.MSC-S (n=3-8), A.Vhc (n=4-8), A.MSC-S (n=3-8). Two-way ANOVA followed by Tukey's post-hoc test was used for statistical analysis. If sex is not indicated, data contain equal numbers of female and male rats (50/50 ratio).

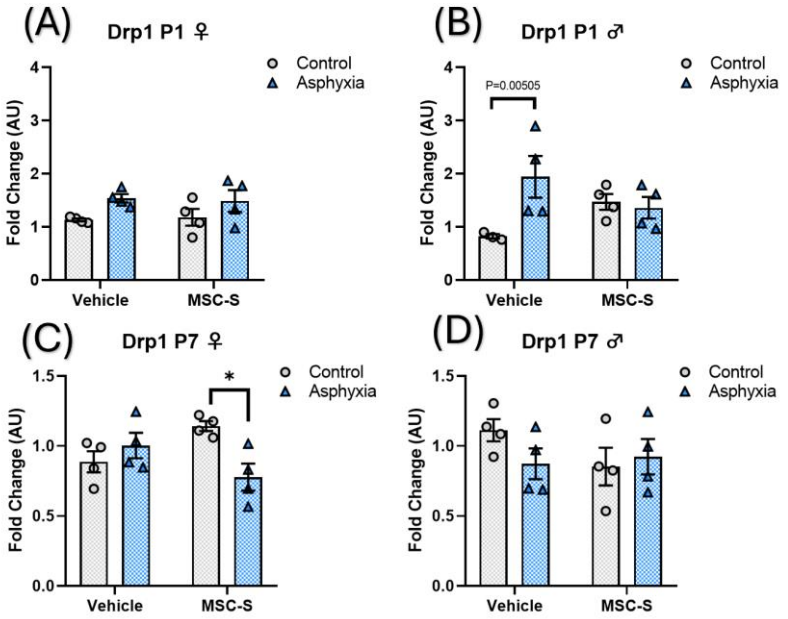

Annex 6: Drp1 levels at P1 and P7 separated by sex, following PA and MSC-S treatment. A: Female and B: male Drp1 protein levels at P1. C: Female and D: male Drp1 protein levels at P7. Data are presented as fold change relative to control levels, expressed as mean ± SEM, C.Vhc (n=4), C.MSC-S (n=4), A.Vhc (n=4), A.MSC-S (n=4). Two-way ANOVA followed by Tukey's post-hoc test was used for statistical analysis.

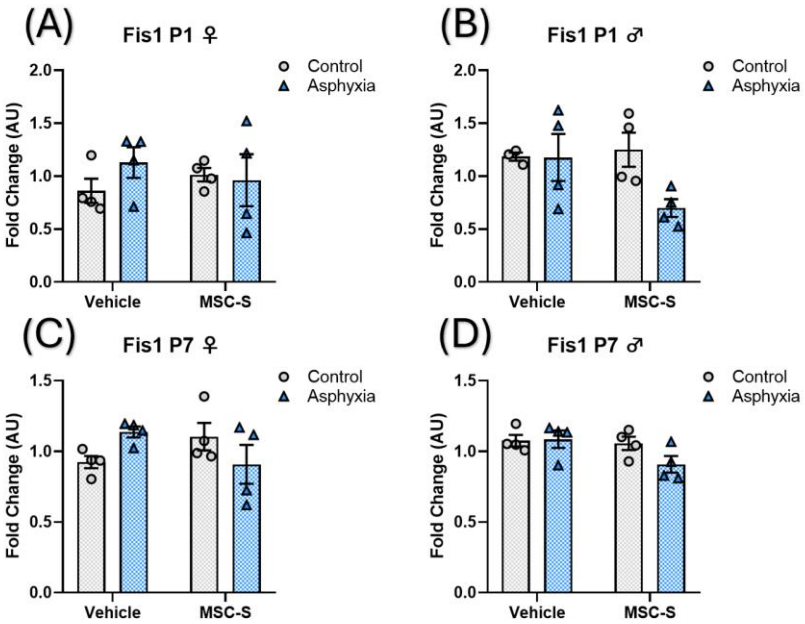

Annex 7: Fis1 levels at P1 and P7 separated by sex, following PA and MSC-S treatment. A: Female and B: male Fis1 protein levels at P1. C: Female and D: male Fis1 protein levels at P7. Data are presented as fold change relative to control levels, expressed mean ± SEM, C.Vhc (n=4), C.MSC-S (n=4), A.Vhc (n=4), A.MSC-S (n=4). Two-way ANOVA followed by Tukey's post-hoc test was used for statistical analysis.

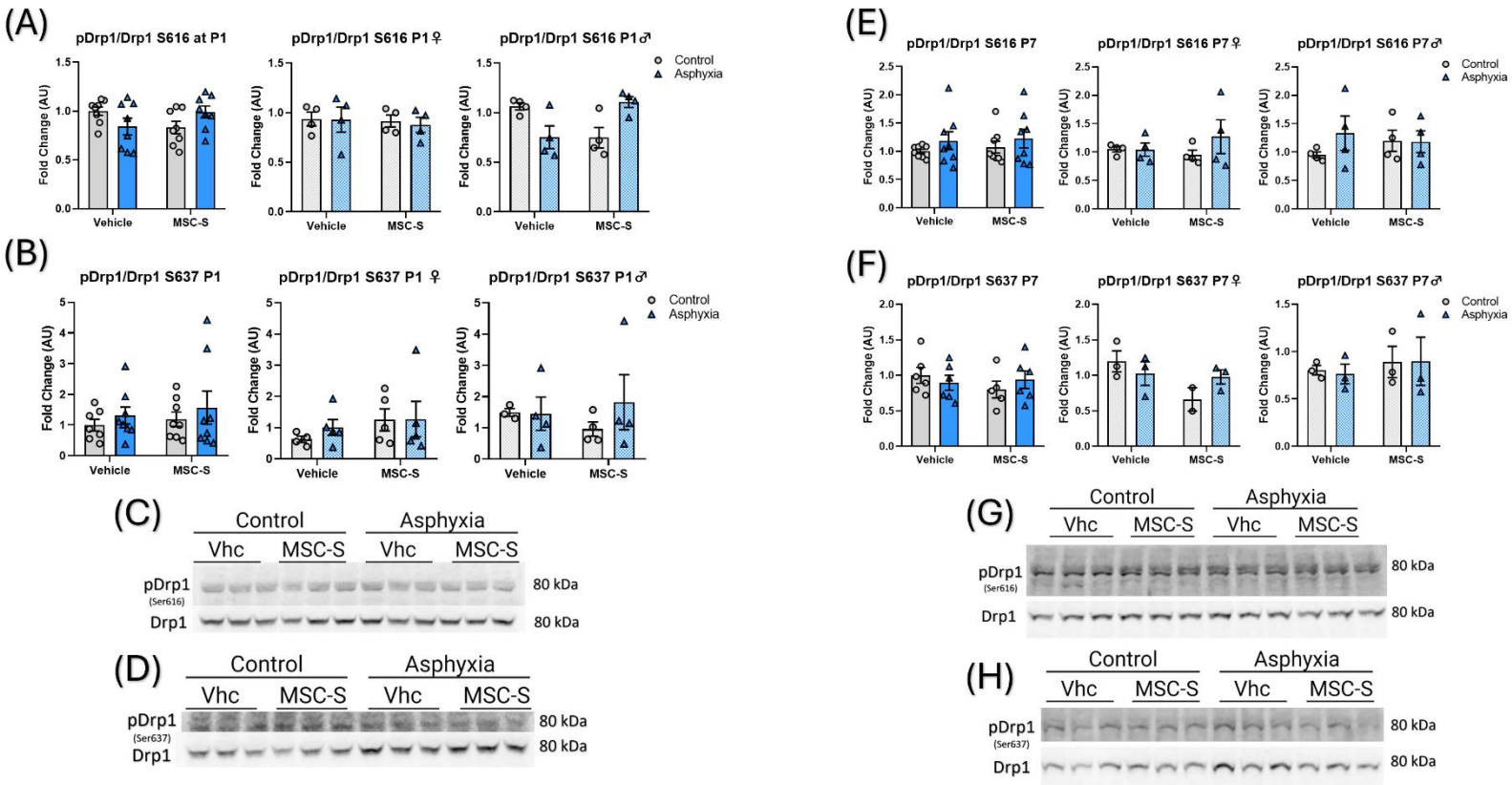

Annex 8: Drp1 phosphorylation at P1 and P7, following PA and MSC-S treatment. A: Quantification of pDrp1 S616 protein levels and segregated by sex at P1. B: Quantification of pDrp1 S637 protein levels and segregated by sex at P1. C: Representative Western blot image of pDrp1 S616 at P1. D: Representative Western blot image of pDrp1 S637 at P1. E: Quantification of pDrp1 S616 protein levels at P7 and segregated by sex. F: Quantification of pDrp1 S637 protein levels, segregated by sex at P7. G: Representative Western blot image of pDrp1 S616 at P7. H: Representative Western blot image of pDrp1 S616 at P7. Data are presented as fold change relative to control levels, normalised to β-actin as the loading control, expressed as mean ± SEM, C.Vhc (n=3-8), C.MSC-S (n=2-8), A.Vhc (n=3-8), A.MSC-S (n=3-8). Two-way ANOVA followed by Tukey's post-hoc test was used for statistical analysis, *p<0.05, **p<0.005. If sex is not indicated, data contain equal numbers of female and male rats (50/50 ratio).

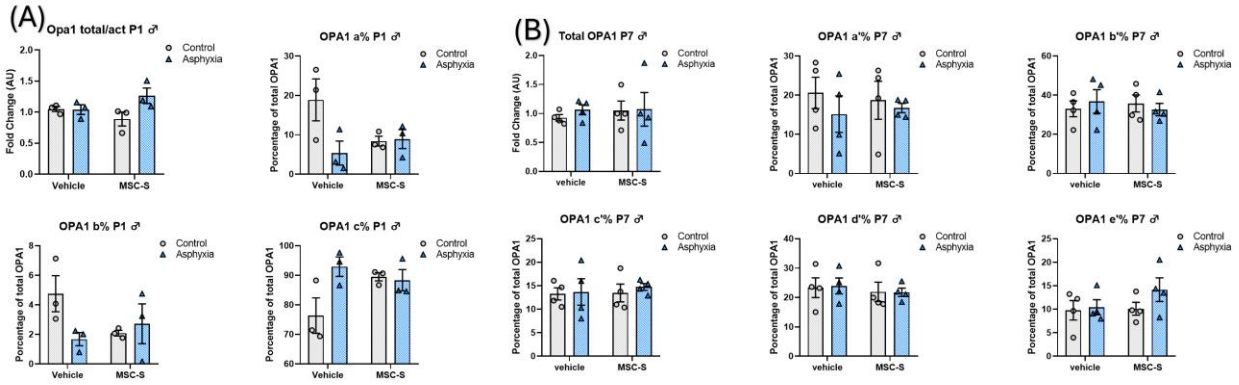

Annex 9: OPA1 males at P1 and P7, following PA and MSC-S. A: Total OPA1 and individual forms (a to c) quantification at P1, only in male animals. B: Total OPA1 and individual forms (a' to e') quantification at P7, only in male animals. Data are presented as fold change relative to control levels and as a percentage of total OPA1, with β-actin as the loading control, expressed as mean ± SEM, C.Vhc (n=3-4), C.MSC-S (n=3-4), A.Vhc (n=3-4), A.MSC-S (n=3-4). Two-way ANOVA followed by Tukey's post-hoc test was used for statistical analysis.

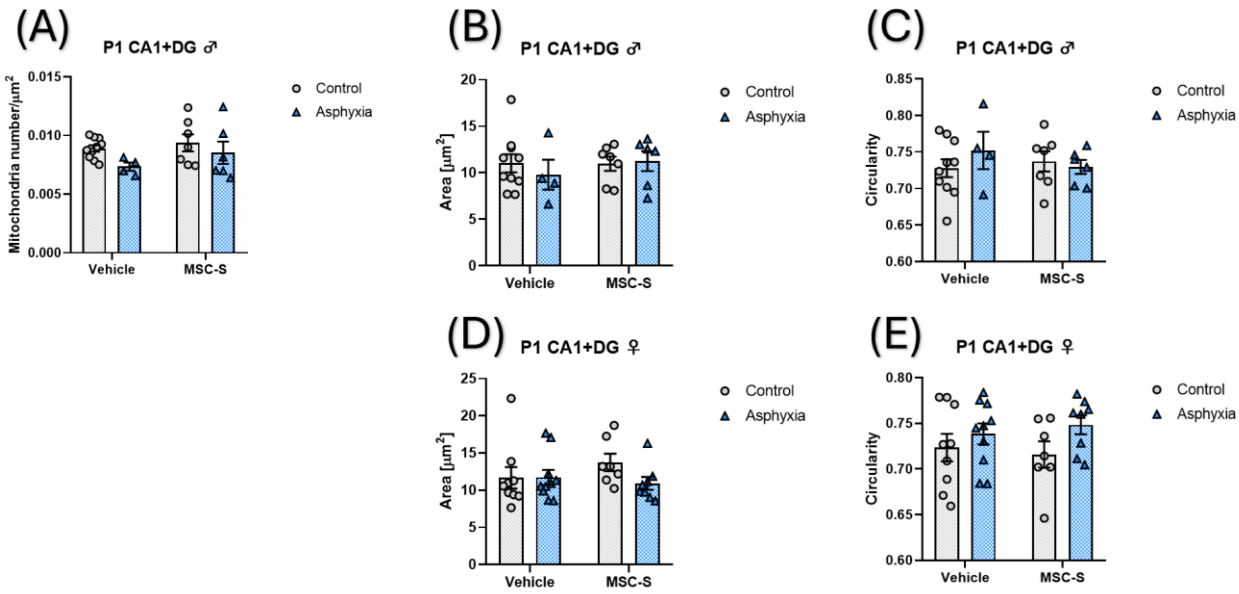

Annex 10: Mitochondria morphology in CA1+DG at P1, segregated by sex, following PA and MSC-S. A: Mitochondrial density in males. Mitochondria area in B: males and D: females. Mitochondria circularity in C: males and E: females. Data are expressed as mean ± SEM, C.Vhc (n=9-10), C.MSC-S (n=7), A.Vhc (n=4-10), A.MSC-S (n=6-8). Two-way ANOVA followed by Tukey's post-hoc test was used for statistical analysis.

A.12. References:

[1] M. A. Rainaldi and J. M. Perlman, 'Pathophysiology of birth asphyxia', *Clin Perinatol*, vol. 43, no. 3, pp. 409–422, 2016.

[2] Jelka. Zupan, Elisabeth. Aȟman, and World Health Organization., *Neonatal and perinatal mortality : country, regional and global estimates 2004*. World Health Organization, 2007.

[3] 'Neonatal Encephalopathy and Neurologic Outcome, Second Edition'.

[4] R. Antonucci, A. Porcella, and M. D. Pilloni, 'Perinatal asphyxia in the term newborn', *Journal of Pediatric and Neonatal Individualized Medicine*, vol. 3, no. 2, 2014, doi: 10.7363/030269.

[5] R. Moshiro, P. Mdoe, and J. M. Perlman, 'A Global View of Neonatal Asphyxia and Resuscitation', *Front Pediatr*, vol. 7, no. November, pp. 1–6, 2019, doi: 10.3389/fped.2019.00489.

[6] I. Milsom, L. Ladfors, K. Thiringer, A. Niklasson, A. Odeback, and E. Thornberg, 'Influence of maternal, obstetric and fetal risk factors on the prevalence of birth asphyxia at term in a Swedish urban population', *Acta Obstet Gynecol Scand*, vol. 81, no. 10, pp. 909–917, Oct. 2002, doi: 10.1034/j.1600-0412.2002.811003.x.

[7] A. L. Solevåg, G. M. Schmölzer, and P. Y. Cheung, 'Novel interventions to reduce oxidative-stress related brain injury in neonatal asphyxia', *Free Radic Biol Med*, vol. 142, no. April, pp. 113–122, 2019, doi: 10.1016/j.freeradbiomed.2019.04.028.

[8] C. Thornton, A. A. Baburamani, A. Kichev, and H. Hagberg, 'Oxidative stress and endoplasmic reticulum (ER) stress in the development of neonatal hypoxic-ischaemic brain injury', *Biochem Soc Trans*, vol. 45, no. 5, pp. 1067–1076, 2017, doi: 10.1042/BST20170017.

[9] P. Morales *et al.*, 'Plasticity of hippocampus following perinatal asphyxia: Effects on postnatal apoptosis and neurogenesis', *J Neurosci Res*, vol. 86, no. 12, pp. 2650–2662, 2008, doi: 10.1002/jnr.21715.

[10] P. Morales *et al.*, 'Plasticity of hippocampus following perinatal asphyxia: Effects on postnatal apoptosis and neurogenesis', *J Neurosci Res*, vol. 86, no. 12, pp. 2650–2662, 2008, doi: 10.1002/jnr.21715.

[11] P. K. Samaiya, S. Krishnamurthy, and A. Kumar, 'Mitochondrial dysfunction in perinatal asphyxia: role in pathogenesis and potential therapeutic interventions', Dec. 01, 2021, *Springer*. doi: 10.1007/s11010-021-04253-8.

[12] E. Rocha-Ferreira and M. Hristova, 'Plasticity in the neonatal brain following hypoxic-ischaemic injury', *Neural Plast*, vol. 2016, 2016, doi: 10.1155/2016/4901014.

[13] K. Plachá, D. Luptáková, L. Bačiak, E. Ujházy, and I. Juránek, 'Neonatal brain injury as a consequence of insufficient cerebral oxygenation', *Neuroendocrinol Lett*, vol. 37, no. 2, pp. 27179569–370216, 2016, [Online]. Available: www.nel.edu

[14] M. V Johnston, W. H. Trescher, A. Ishida, and W. Nakajima, 'The Developing Nervous System: A Series of Review Articles Neurobiology of Hypoxic-Ischemic Injury in the Developing Brain', 2001.

[15] P. Morales *et al.*, 'Pathophysiology of perinatal asphyxia: Can we predict and improve individual outcomes?', Jun. 2011. doi: 10.1007/s13167-011-0100-3.

[16] C. I. Rousset, A. A. Baburamani, C. Thornton, and H. Hagberg, 'Mitochondria and perinatal brain injury', *Journal of Maternal-Fetal and Neonatal Medicine*, vol. 25, no. SUPPL. 1, pp. 35–38, 2012, doi: 10.3109/14767058.2012.666398.

[17] C. Thornton, A. Jones, S. Nair, A. Aabdien, C. Mallard, and H. Hagberg, 'Mitochondrial dynamics, mitophagy and biogenesis in neonatal hypoxic-ischaemic brain injury', *FEBS Lett*, vol. 592, no. 5, pp. 812–830, 2018, doi: 10.1002/1873-3468.12943.

[18] M. Brini, T. Calì, D. Ottolini, and E. Carafoli, 'Neuronal calcium signaling: Function and dysfunction', 2014, *Birkhauser Verlag AG*. doi: 10.1007/s00018-013-1550-7.

[19] M. Akbari, T. B. L. Kirkwood, and V. A. Bohr, 'Mitochondria in the signaling pathways that control longevity and health span', Sep. 01, 2019, *Elsevier Ireland Ltd*. doi: 10.1016/j.arr.2019.100940.

[20] J. Nunnari and A. Suomalainen, 'Mitochondria: In sickness and in health', *Cell*, vol. 148, no. 6, pp. 1145–1159, 2012, doi: 10.1016/j.cell.2012.02.035.

[21] A. Kumar, S. V. K. Ramakrishna, S. Basu, and G. R. K. Rao, 'Oxidative Stress in Perinatal Asphyxia', *Pediatr Neurol*, vol. 38, no. 3, pp. 181–185, 2008, doi: 10.1016/j.pediatrneurol.2007.10.008.

[22] W. Chen, H. Zhao, and Y. Li, 'Mitochondrial dynamics in health and disease: mechanisms and potential targets', *Signal Transduct Target Ther*, vol. 8, no. 1, p. 333, 2023, doi: 10.1038/s41392-023-01547-9.

[23] D. C. Chan, 'Mitochondrial Dynamics and Its Involvement in Disease', 2019, doi: 10.1146/annurev-pathmechdis.

[24] L. Tilokani, S. Nagashima, V. Paupe, and J. Prudent, 'Mitochondrial dynamics: Overview of molecular mechanisms', Jul. 20, 2018, *Portland Press Ltd*. doi: 10.1042/EBC20170104.

[25] H. Chen, J. M. McCaffery, and D. C. Chan, 'Mitochondrial Fusion Protects against Neurodegeneration in the Cerebellum', *Cell*, vol. 130, no. 3, pp. 548–562, 2007, doi: 10.1016/j.cell.2007.06.026.

[26] J. Waddell *et al.*, 'Attenuation of Aβ toxicity by promotion of mitochondrial fusion in neuroblastoma cells by liquiritigenin', *Arch Pharm Res*, vol. 152, no. 6, pp. 1137–1143, 2016, doi: 10.1111/jnc.13590.

[27] N. Ishihara, Y. Eura, and K. Mihara, 'Mitofusin 1 and 2 play distinct roles in mitochondrial fusion reactions via GTPase activity', *J Cell Sci*, vol. 117, no. 26, pp. 6535–6546, Dec. 2004, doi: 10.1242/jcs.01565.

[28] H. Lee and Y. Yoon, 'Mitochondrial Membrane Dynamics—Functional Positioning of OPA1', *Antioxidants*, vol. 7, no. 12, 2018, doi: 10.3390/antiox7120186.

[29] R. Anand *et al.*, 'The i-AAA protease YME1L and OMA1 cleave OPA1 to balance mitochondrial fusion and fission', *Journal of Cell Biology*, vol. 204, no. 6, pp. 919–929, 2014, doi: 10.1083/jcb.201308006.

[30] V. Del Dotto, M. Fogazza, V. Carelli, M. Rugolo, and C. Zanna, 'Eight human OPA1 isoforms, long and short: What are they for?', *Biochimica et Biophysica Acta (BBA) - Bioenergetics*, vol. 1859, no. 4, pp. 263–269, 2018, doi: https://doi.org/10.1016/j.bbabio.2018.01.005.

[31] C. Hu *et al.*, 'OPA1 and MICOS Regulate mitochondrial crista dynamics and formation', *Cell Death Dis*, vol. 11, no. 10, Oct. 2020, doi: 10.1038/s41419-020-03152-y.

[32] A. Jahani-Asl and R. S. Slack, 'The phosphorylation state of Drp1 determines cell fate', Oct. 2007. doi: 10.1038/sj.embor.7401077.

[33] H. Lee and Y. Yoon, 'Mitochondrial fission: Regulation and ER connection', *Mol Cells*, vol. 37, no. 2, pp. 89–94, 2014, doi: 10.14348/molcells.2014.2329.

[34] O. C. Losó n, Z. Song, H. Chen, and D. C. Chan, 'Fis1, Mff, MiD49, and MiD51 mediate Drp1 recruitment in mitochondrial fission', *Mol Biol Cell*, vol. 24, no. 5, pp. 659–667, Mar. 2013, doi: 10.1091/mbc.E12-10-0721.

[35] H. Pradeep, B. Sharma, and G. K. Rajanikant, 'Drp1 in Ischemic Neuronal Death: An Unusual Suspect', *Curr Med Chem*, vol. 21, no. 19, pp. 2183–2189, 2014, doi: 10.2174/09298673216661312282035 13.

[36] R. Yu, S. Jin, U. Lendahl, M. Nistér, and J. Zhao, 'Human Fis1 regulates mitochondrial dynamics through inhibition of the fusion machinery', *EMBO J*, vol. 38, no. 8, Apr. 2019, doi: 10.15252/embj.201899748.

[37] A. R. Fenton, T. A. Jongens, and E. L. F. Holzbaur, 'Mitochondrial dynamics: Shaping and remodeling an organelle network', Feb. 01, 2021, *Elsevier Ltd*. doi: 10.1016/j.ceb.2020.08.014.

[38] J. Grohm *et al.*, 'Inhibition of Drp1 provides neuroprotection in vitro and in vivo', *Cell Death Differ*, vol. 19, no. 9, pp. 1446–1458, 2012, doi: 10.1038/cdd.2012.18.

[39] H. Hagberg, C. Mallard, C. I. Rousset, and C. Thornton, 'Mitochondria: Hub of injury responses in the developing brain', *Lancet Neurol*, vol. 13, no. 2, pp. 217–232, 2014, doi: 10.1016/S1474-4422(13)70261-8.

[40] I. G. Onyango, J. Lu, M. Rodova, E. Lezi, A. B. Crafter, and R. H. Swerdlow, 'Regulation of neuron mitochondrial biogenesis and relevance to brain health', Jan. 2010. doi: 10.1016/j.bbadis.2009.07.014.

[41] L. Zhang *et al.*, 'Altered brain energetics induces mitochondrial fission arrest in Alzheimer's Disease', *Sci Rep*, vol. 6, no. November 2015, pp. 1–12, 2016, doi: 10.1038/srep18725.

[42] C. Hu, Y. Huang, and L. Li, 'Drp1-dependent mitochondrial fission plays critical roles in physiological and pathological progresses in mammals', Jan. 13, 2017, *MDPI AG*. doi: 10.3390/ijms18010144.

[43] J. Gao, L. Wang, J. Liu, F. Xie, B. Su, and X. Wang, 'Abnormalities of mitochondrial dynamics in neurodegenerative diseases', *Antioxidants*, vol. 6, no. 2, 2017, doi: 10.3390/antiox6020025.

[44] K. H. Flippo and S. Strack, 'Mitochondrial dynamics in neuronal injury, development and plasticity', *J Cell Sci*, vol. 130, no. 4, pp. 671–681, 2017, doi: 10.1242/jcs.171017.

[45] Y. Li *et al.*, 'Dynamic Changes of Mitochondrial Fusion and Fission in Brain Injury after Cardiac Arrest in Rats', *Biomed Res Int*, vol. 2017, 2017, doi: 10.1155/2017/1948070.

[46] W. Zuo, S. Zhang, C. Y. Xia, X. F. Guo, W. Bin He, and N. H. Chen, 'Mitochondria autophagy is induced after hypoxic/ischemic stress in a Drp1 dependent manner: The role of inhibition of Drp1 in ischemic brain damage', *Neuropharmacology*, vol. 86, pp. 103–115, 2014, doi: 10.1016/j.neuropharm.2014.07.002.

[47] S. N. Weis *et al.*, 'Neonatal hypoxia-ischemia induces sex-related changes in rat brain mitochondria', *Mitochondrion*, vol. 12, no. 2, pp. 271–279, 2012, doi: 10.1016/j.mito.2011.10.002.

[48] T. G. Demarest, R. A. Schuh, J. Waddell, M. C. McKenna, and G. Fiskum, 'Sex-dependent mitochondrial respiratory impairment and oxidative stress in a rat model of neonatal hypoxic-ischemic encephalopathy', *J Neurochem*, vol. 137, no. 5, pp. 714–729, 2016, doi: 10.1111/jnc.13590.

[49] T. G. Demarest *et al.*, 'Sex-dependent mitophagy and neuronal death following rat neonatal hypoxia–ischemia', *Neuroscience*, vol. 335, pp. 103–113, 2016, doi: 10.1016/j.neuroscience.2016.08.026.

[50] A. A. Baburamani *et al.*, 'Mitochondrial Optic Atrophy (OPA) 1 processing is altered in response to neonatal hypoxic-ischemic brain injury', *Int J Mol Sci*, vol. 16, no. 9, pp. 22509–22526, 2015, doi: 10.3390/ijms160922509.

[51] W. Yin, A. P. Signore, M. Iwai, G. Cao, Y. Gao, and J. Chen, 'Rapidly Increased Neuronal Mitochondrial Biogenesis After Hypoxic-Ischemic Brain Injury', *Stroke*, vol. 39, no. 11, pp. 3057–3063, Nov. 2008, doi: 10.1161/STROKEAHA.108.520114.

[52] L. Jia, J. Wang, H. Cao, X. Zhang, W. Rong, and Z. Xu, 'Activation of PGC-1α and Mitochondrial Biogenesis Protects Against Prenatal Hypoxic–ischemic Brain Injury', *Neuroscience*, vol. 432, pp. 63–72, 2020, doi: 10.1016/j.neuroscience.2020.02.035.

[53] J. P. M. Lima *et al.*, 'Perinatal Asphyxia and Brain Development: Mitochondrial Damage Without Anatomical or Cellular Losses', *Mol Neurobiol*, vol. 55, no. 11, pp. 8668–8679, 2018, doi: 10.1007/s12035-018-1019-7.

[54] C. E. J. Parmentier *et al.*, 'Increased Use of Therapeutic Hypothermia in Infants with Milder Neonatal Encephalopathy due to Presumed Perinatal Asphyxia', *Neonatology*, vol. 117, no. 4, pp. 488–494, Dec. 2020, doi: 10.1159/000508710.

[55] P. Parikh and S. E. Juul, 'Neuroprotective Strategies in Neonatal Brain Injury', *Journal of Pediatrics*, vol. 192, pp. 22–32, 2018, doi: 10.1016/j.jpeds.2017.08.031.

[56] K. J. Hassell, M. Ezzati, D. Alonso-Alconada, D. J. Hausenloy, and N. J. Robertson, 'New horizons for newborn brain protection: Enhancing endogenous neuroprotection', Nov. 01, 2015, *BMJ Publishing Group*. doi: 10.1136/archdischild-2014-306284.

[57] S. Y. Ahn, Y. S. Chang, D. K. Sung, S. I. Sung, and W. S. Park, 'Hypothermia broadens the therapeutic time window of mesenchymal stem cell transplantation for severe neonatal hypoxic ischemic encephalopathy', *Sci Rep*, vol. 8, no. 1, Dec. 2018, doi: 10.1038/s41598-018-25902-x.

[58] J. Herz *et al.*, 'Interaction between hypothermia and delayed mesenchymal stem cell therapy in neonatal hypoxic-ischemic brain injury', *Brain Behav Immun*, vol. 70, pp. 118–130, May 2018, doi: 10.1016/j.bbi.2018.02.006.

[59] D. E. Rodríguez-Fuentes, L. E. Fernández-Garza, J. A. Samia-Meza, S. A. Barrera-Barrera, A. I. Caplan, and H. A. Barrera-Saldaña, 'Mesenchymal Stem Cells Current Clinical Applications: A Systematic Review', *Arch Med Res*, vol. 52, no. 1, pp. 93–101, Jan. 2021, doi: 10.1016/j.arcmed.2020.08.006.

[60] P. K. L., S. Kandoi, R. Misra, V. S., R. K., and R. S. Verma, 'The mesenchymal stem cell secretome: A new paradigm towards cell-free therapeutic mode in regenerative medicine', Apr. 01, 2019, *Elsevier Ltd*. doi: 10.1016/j.cytogfr.2019.04.002.

[61] F. J. Vizoso, N. Eiro, S. Cid, J. Schneider, and R. Perez-Fernandez, 'Mesenchymal stem cell secretome: Toward cell-free therapeutic strategies in regenerative medicine', Sep. 01, 2017, *MDPI AG*. doi: 10.3390/ijms18091852.

[62] D. Z. Sun, B. Abelson, P. Babbar, and M. S. Damaser, 'Harnessing the mesenchymal stem cell secretome for regenerative urology', *Nat Rev Urol*, vol. 16, no. 6, pp. 363–375, 2019, doi: 10.1038/s41585-019-0169-3.

[63] A. González-González, D. García-Sánchez, M. Dotta, J. C. Rodríguez-Rey, and F. M. Pérez-Campo, 'Mesenchymal stem cells secretome: The cornerstone of cell-free regenerative medicine', *World J Stem Cells*, vol. 12, no. 12, pp. 1439–1690, 2020, doi: 10.4252/wjsc.v12.i12.1529.

[64] F. Teixeira and A. Salgado, 'Mesenchymal stem cells secretome: Current trends and future challenges', Jan. 01, 2020, *Wolters Kluwer Medknow Publications*. doi: 10.4103/1673-5374.264455.

[65] M. Mocchi *et al.*, 'Freeze-Dried Mesenchymal stem cell-secretome pharmaceuticalization: Optimization of formulation and manufacturing process Robustness', *Pharmaceutics*, vol. 13, no. 8, Aug. 2021, doi: 10.3390/pharmaceutics13081129.

[66] G. Schepici, A. Gugliandolo, and E. Mazzon, 'Mesenchymal Stromal Cells Preconditioning: A New Strategy to Improve Neuroprotective Properties', Feb. 01, 2022, *MDPI*. doi: 10.3390/ijms23042088.

[67] F. Ezquer *et al.*, 'Activated mesenchymal stem cell administration inhibits chronic alcohol drinking and suppresses relapse-like drinking in high-alcohol drinker rats', *Addiction Biology*, vol. 24, no. 1, pp. 17–27, 2019, doi: 10.1111/adb.12572.

[68] C. Oses *et al.*, 'Preconditioning of adipose tissue-derived mesenchymal stem cells with deferoxamine increases the production of pro-angiogenic, neuroprotective and anti-inflammatory factors: Potential application in the treatment of diabetic neuropathy', *PLoS One*, vol. 12, no. 5, pp. 1–22, 2017, doi: 10.1371/journal.pone.0178011.

[69] S. A. Selim, S. A. A. El-Baset, A. A. A. Kattaia, E. M. Askar, and E. A. Elkader, 'Bone marrow-derived mesenchymal stem cells ameliorate liver injury in a rat model of sepsis by activating Nrf2 signaling', *Histochem Cell Biol*, vol. 151, no. 3, pp. 249–262, 2019, doi: 10.1007/s00418-018-1731-4.

[70] S. Ni, D. Wang, X. Qiu, L. Pang, Z. Song, and K. Guo, 'Bone marrow mesenchymal stem cells protect against bleomycin-induced pulmonary fibrosis in rat by activating Nrf2 signaling', *Int J Clin Exp Pathol*, vol. 8, no. 7, pp. 7752–7761, 2015.

[71] X. Chen *et al.*, 'Adipose-derived mesenchymal stem cells promote the survival of fat grafts via crosstalk between the nrf2 and tlr4 pathways', *Cell Death Dis*, vol. 7, no. 9, pp. e2369-12, 2016, doi: 10.1038/cddis.2016.261.

[72] E. J. Lee *et al.*, 'Mesenchymal stem cells reduce ER stress via PERK-Nrf2 pathway in an aged mouse model', *Respirology*, vol. 25, no. 4, pp. 417–426, 2020, doi: 10.1111/resp.13646.

[73] X. Huang *et al.*, 'Adipose-derived mesenchymal stem cells protect against CMS-induced depression-like behaviors in mice via regulating the Nrf2/HO-1 and TLR4/NF-κB signaling pathways', *Acta Pharmacol Sin*, no. October, pp. 1–8, 2019, doi: 10.1038/s41401-019-0317-6.

[74] G. Zhang *et al.*, 'Mesenchymal stromal cell-derived extracellular vesicles protect against acute kidney injury through anti-oxidation by enhancing Nrf2/ARE activation in rats', *Kidney Blood Press Res*, vol. 41, no. 2, pp. 119–128, 2016, doi: 10.1159/000443413.

[75] F. Ezquer *et al.*, 'Intranasal delivery of mesenchymal stem cell-derived exosomes reduces oxidative stress and markedly inhibits ethanol consumption and post-deprivation relapse drinking.', *Addiction Biology*, 2018, doi: 10.1111/adb.12675.

[76] N. Farfán *et al.*, 'Intranasal Administration of Mesenchymal Stem Cell Secretome Reduces Hippocampal Oxidative Stress, Neuroinflammation and Cell Death, Improving the Behavioral Outcome Following Perinatal Asphyxia', *Int J Mol Sci*, vol. 21, no. 20, 2020, doi: 10.3390/ijms21207800.

[77] K. M. Holmström, R. V. Kostov, and A. T. Dinkova-Kostova, 'The multifaceted role of Nrf2 in mitochondrial function', *Curr Opin Toxicol*, vol. 2, pp. 80–91, 2016, doi: 10.1016/j.cotox.2016.10.002.

[78] R. Zhang, M. Xu, Y. Wang, F. Xie, G. Zhang, and X. Qin, 'Nrf2—a Promising Therapeutic Target for Defensing Against Oxidative Stress in Stroke', *Mol Neurobiol*, vol. 54, no. 8, pp. 6006–6017, 2017, doi: 10.1007/s12035-016-0111-0.

[79] S. Kasai, S. Shimizu, Y. Tatara, J. Mimura, and K. Itoh, 'Regulation of Nrf2 by mitochondrial reactive oxygen species in physiology and pathology', *Biomolecules*, vol. 10, no. 2, 2020, doi: 10.3390/biom10020320.

[80] N. Esteras and A. Y. Abramov, 'Nrf2 as a regulator of mitochondrial function: Energy metabolism and beyond', *Free Radic Biol Med*, vol. 189, pp. 136–153, Aug. 2022, doi: 10.1016/j.freeradbiomed.2022.07.013.

[81] I. geun Ryoo and M. K. Kwak, 'Regulatory crosstalk between the oxidative stress-related transcription factor Nfe2l2/Nrf2 and mitochondria', *Toxicol Appl Pharmacol*, vol. 359, pp. 24–33, Nov. 2018, doi: 10.1016/j.taap.2018.09.014.

[82] A. T. Dinkova-Kostova and A. Y. Abramov, 'The emerging role of Nrf2 in mitochondrial function', 2015, *Elsevier Inc.* doi: 10.1016/j.freeradbiomed.2015.04.036.

[83] S. Kovac, P. R. Angelova, K. M. Holmström, Y. Zhang, A. T. Dinkova-Kostova, and A. Y. Abramov, 'Nrf2 regulates ROS production by mitochondria and NADPH oxidase', *Biochim Biophys Acta Gen Subj*, vol. 1850, no. 4, pp. 794–801, 2015, doi: 10.1016/j.bbagen.2014.11.021.

[84] K. M. Holmström, R. V. Kostov, and A. T. Dinkova-Kostova, 'The multifaceted role of Nrf2 in mitochondrial function', Dec. 01, 2016, *Elsevier B.V.* doi: 10.1016/j.cotox.2016.10.002.

[85] R. Sabouny *et al.*, 'The Keap1-Nrf2 Stress Response Pathway Promotes Mitochondrial Hyperfusion Through Degradation of the Mitochondrial Fission Protein Drp1', *Antioxid Redox Signal*, vol. 27, no. 18, pp. 1447–1459, Dec. 2017, doi: 10.1089/ars.2016.6855.

[86] C. De Gregorio *et al.*, 'Human adipose-derived mesenchymal stem cell-conditioned medium ameliorates polyneuropathy and foot ulceration in diabetic BKS db/db mice', *Stem Cell Res Ther*, vol. 11, no. 1, May 2020, doi: 10.1186/s13287-020-01680-0.

[87] G. C. Tu, Q. N. Cao, F. Zhou, and Y. Israel, 'Tetranucleotide GGGA motif in primary RNA transcripts: Novel target site for antisense design', *Journal of Biological Chemistry*, vol. 273, no. 39, pp. 25125–25131, Sep. 1998, doi: 10.1074/jbc.273.39.25125.

[88] F. Chen, P. W. Tillberg, and E. S. Boyden, 'Expansion microscopy', *Science (1979)*, vol. 347, no. 6221, pp. 543–548, Jan. 2015, doi: 10.1126/science.1260088.

[89] E. Dell'Anna *et al.*, 'Delayed neuronal death following perinatal asphyxia in rat', *Exp Brain Res*, vol. 115, no. 1, pp. 105–115, 1997, doi: 10.1007/PL00005670.

[90] R. L. Naeye, L. S. Burt, D. L. Wright, W. A. Blanc, and D. Tatter, 'NEONATAL MORTALITY, THE MALE DISADVANTAGE', *Pediatrics*, vol. 48, no. 6, pp. 902–906, Dec. 1971, doi: 10.1542/peds.48.6.902.

[91] P. J. Magistretti and I. Allaman, 'Lactate in the brain: From metabolic end-product to signalling molecule', Apr. 01, 2018, *Nature Publishing Group*. doi: 10.1038/nrn.2018.19.

[92] Y. F. Tu *et al.*, 'Lactate predicts neurological outcomes after perinatal asphyxia in post-hypothermia era: A prospective cohort study', *Life*, vol. 11, no. 11, Nov. 2021, doi: 10.3390/life11111193.

[93] M. Z. Jovandaric and S. J. Milenkovic, 'Neurological impairments in hypoxic neonates and lactate levels', *Neurol Res*, vol. 40, no. 10, pp. 822–827, Oct. 2018, doi: 10.1080/01616412.2018.1484589.

[94] G. Wu, Y.-Z. Fang, S. Yang, J. R. Lupton, and N. D. Turner, 'Recent Advances in Nutritional Sciences Glutathione Metabolism and Its Implications for Health 1', 2004.

[95] A. P. Wingo *et al.*, 'Sex differences in brain protein expression and disease', *Nat Med*, vol. 29, no. 9, pp. 2224–2232, Sep. 2023, doi: 10.1038/s41591-023-02509-y.

[96] C. Lespay-Rebolledo, R. Perez-Lobos, A. Tapia-Bustos, V. Vio, P. Morales, and M. Herrera-Marschitz, 'Regionally Impaired Redox Homeostasis in the Brain of Rats Subjected to Global Perinatal Asphyxia: Sustained Effect up to 14 Postnatal Days', *Neurotox Res*, vol. 34, no. 3, pp. 660–676, Oct. 2018, doi: 10.1007/s12640-018-9928-9.

[97] K. A. Alkadhi, 'Cellular and Molecular Differences Between Area CA1 and the Dentate Gyrus of the Hippocampus', Sep. 15, 2019, *Humana Press Inc.* doi: 10.1007/s12035-019-1541-2.

[98] R. H. S. Westerink, J. P. Beekwilder, and W. J. Wadman, 'Differential alterations of synaptic plasticity in dentate gyrus and CA1 hippocampal area of Calbindin-D28K knockout mice', *Brain Res*, vol. 1450, pp. 1–10, Apr. 2012, doi: 10.1016/j.brainres.2012.02.036.

[99] T. J. Nicholls and M. Minczuk, 'In D-loop: 40 years of mitochondrial 7S DNA', *Exp Gerontol*, vol. 56, pp. 175–181, 2014, doi: 10.1016/j.exger.2014.03.027.

[100] Z. Wu *et al.*, 'Mechanisms Controlling Mitochondrial Biogenesis and Respiration through the Thermogenic Coactivator PGC-1', *Cell*, vol. 98, no. 1, pp. 115–124, Jul. 1999, doi: 10.1016/S0092-8674(00)80611-X.

[101] I. Kang, C. T. Chu, and B. A. Kaufman, 'The mitochondrial transcription factor TFAM in neurodegeneration: emerging evidence and mechanisms', Mar. 01, 2018, *Wiley Blackwell*. doi: 10.1002/1873-3468.12989.

[102] M. Zerihun, S. Sukumaran, and N. Qvit, 'The Drp1-Mediated Mitochondrial Fission Protein Interactome as an Emerging Core Player in Mitochondrial Dynamics and Cardiovascular Disease Therapy', Mar. 01, 2023, *Multidisciplinary Digital Publishing Institute (MDPI)*. doi: 10.3390/ijms24065785.

[103] Q. Shen *et al.*, 'Mutations in Fis1 disrupt orderly disposal of defective mitochondria', *Mol Biol Cell*, vol. 25, no. 1, pp. 145–159, 2014.

[104] V. Di Pietro *et al.*, 'Fusion or fission: The destiny of mitochondria in traumatic brain injury of different severities', *Sci Rep*, vol. 7, no. 1, Dec. 2017, doi: 10.1038/s41598-017-09587-2.

[105] R. Gilkerson, P. De La Torre, and S. St. Vallier, 'Mitochondrial OMA1 and OPA1 as Gatekeepers of Organellar Structure/Function and Cellular Stress Response', *Front Cell Dev Biol*, vol. 9, 2021, [Online]. Available: https://www.frontiersin.org/articles/10.3389/fcell.2021.626117

[106] S. Nair *et al.*, 'Induction of Mitochondrial Fragmentation and Mitophagy after Neonatal Hypoxia–Ischemia', *Cells*, vol. 11, no. 7, 2022, doi: 10.3390/cells11071193.

[107] C. Zhao *et al.*, 'Drp1-dependent mitophagy protects against cisplatin-induced apoptosis of renal tubular epithelial cells by improving mitochondrial function', 2017. [Online]. Available: www.impactjournals.com/oncotarget/

[108] N. Li, H. Wang, C. Jiang, and M. Zhang, 'Renal ischemia/reperfusion-induced mitophagy protects against renal dysfunction via Drp1-dependent-pathway', *Exp Cell Res*, vol. 369, no. 1, pp. 27–33, Aug. 2018, doi: 10.1016/j.yexcr.2018.04.025.

[109] Y. S. Park, S. E. Choi, and H. C. Koh, 'PGAM5 regulates PINK1/Parkin-mediated mitophagy via DRP1 in CCCP-induced mitochondrial dysfunction', *Toxicol Lett*, vol. 284, pp. 120–128, Mar. 2018, doi: 10.1016/j.toxlet.2017.12.004.

[110] K. A. Alkadhi, 'Cellular and Molecular Differences Between Area CA1 and the Dentate Gyrus of the Hippocampus', Sep. 15, 2019, *Humana Press Inc.* doi: 10.1007/s12035-019-1541-2.

[111] K. M. Christian, G. li Ming, and H. Song, 'Adult neurogenesis and the dentate gyrus: Predicting function from form', Feb. 03, 2020, *Elsevier B.V.* doi: 10.1016/j.bbr.2019.112346.

[112] M. Khacho and R. S. Slack, 'Mitochondrial dynamics in the regulation of neurogenesis: From development to the adult brain', *Developmental Dynamics*, vol. 247, no. 1, pp. 47–53, 2018, doi: 10.1002/dvdy.24538.

[113] S. Mandal, A. G. Lindgren, A. S. Srivastava, A. T. Clark, and U. Banerjee, 'Mitochondrial Function Controls Proliferation and Early Differentiation Potential of Embryonic Stem Cells', *Stem Cells*, vol. 29, no. 3, pp. 486–495, Mar. 2011, doi: 10.1002/stem.590.

[114] W. Wang *et al.*, 'Mitochondrial DNA Damage Level Determines Neural Stem Cell Differentiation Fate', *The Journal of Neuroscience*, vol. 31, no. 26, p. 9746, Jun. 2011, doi: 10.1523/JNEUROSCI.0852-11.2011.

[115] L. D. Zorova *et al.*, 'Mitochondrial membrane potential', *Anal Biochem*, vol. 552, pp. 50–59, Jul. 2018, doi: 10.1016/j.ab.2017.07.009.

[116] S. Murden, V. Borbélyová, Z. Laštůvka, J. Mysliveček, J. Otáhal, and V. Riljak, 'Gender differences involved in the pathophysiology of the perinatal hypoxic-ischemic damage', 2019, *Czech Academy of Sciences*. doi: 10.33549/physiolres.934356.

[117] L. A. Kelly, A. Branagan, G. Semova, and E. J. Molloy, 'Sex differences in neonatal brain injury and inflammation', 2023, *Frontiers Media SA*. doi: 10.3389/fimmu.2023.1243364.

[118] A. Al Mamun, H. Yu, S. Romana, and F. Liu, 'Inflammatory Responses are Sex Specific in Chronic Hypoxic–Ischemic Encephalopathy', *Cell Transplant*, vol. 27, no. 9, pp. 1328–1339, Sep. 2018, doi: 10.1177/0963689718766362.

[119] C. A. Hill, S. W. Threlkeld, and R. H. Fitch, 'Early testosterone modulated sex differences in behavioral outcome following neonatal hypoxia ischemia in rats', *International Journal of Developmental Neuroscience*, vol. 29, no. 4, pp. 381–388, Jun. 2011, doi: 10.1016/j.ijdevneu.2011.03.005.

[120] U. Cikla *et al.*, 'ERα signaling is required for TrkB-mediated hippocampal neuroprotection in female neonatal mice after hypoxic ischemic encephalopathy', *eNeuro*, vol. 3, no. 1, pp. 99–114, 2016, doi: 10.1523/ENEURO.0025-15.2015.

[121] W. Ni *et al.*, 'Neural stem cell secretome exerts a protective effect on damaged neuron mitochondria in Parkinson's disease model', *Brain Res*, vol. 1790, Sep. 2022, doi: 10.1016/j.brainres.2022.147978.

[122] M. Ramalingam *et al.*, 'Neuroprotective Effects of the Neural-Induced Adipose-Derived Stem Cell Secretome against Rotenone-Induced Mitochondrial and Endoplasmic Reticulum Dysfunction', *Int J Mol Sci*, vol. 24, no. 6, Mar. 2023, doi: 10.3390/ijms24065622.

[123] S. Wang, J. Tan, Y. Miao, and Q. Zhang, 'Mitochondrial Dynamics, Mitophagy, and Mitochondria–Endoplasmic Reticulum Contact Sites Crosstalk Under Hypoxia', Feb. 25, 2022, *Frontiers Media S.A.* doi: 10.3389/fcell.2022.848214.

UNIVERSIDAD DE CHILE

Paola Morales R <pmorales@uchile.cl>

BBAMCR-24-337 - Confirming your submission to BBA - Molecular Cell Research

1 mensaje

BBA - Molecular Cell Research (ELS) <em@editorialmanager.com> 23 de abril de 2024, 18:03
Responder a: "BBA - Molecular Cell Research (ELS)" <support@elsevier.com>
Para: Paola Morales <pmorales@uchile.cl>

Article Title: Mitochondrial Dynamics and Sex-Specific Responses in the Developing Rat Hippocampus: Effect of Perinatal Asphyxia and Mesenchymal Stem Cell Secretome Treatment.
Article Type: Regular Paper

Dear Prof. Dr. Morales:

This is to confirm that the above-mentioned manuscript has been received for consideration in BBA - Molecular Cell Research.

It has been assigned the following manuscript number: **BBAMCR-24-337**.

You will be able to check on the progress of your manuscript by logging on to the Editorial Manager as an author:
https://www.editorialmanager.com/bbamcr/

Soon your paper will be given a manuscript number, at which point you will receive an e-mail for your reference.

No additional authors will be added post submission unless editors receive agreement from all authors and detailed information is supplied as to why the author list should be amended.

Thank you for submitting your work to BBA - Molecular Cell Research. Please feel free to contact our office if you have any questions.

Kind regards,

BBA - Molecular Cell Research

This journal uses the Elsevier Article Transfer Service. This means that if an editor feels your manuscript is more suitable for an alternative journal, then you might be asked to consider transferring the manuscript to such a journal. The recommendation might be provided by a Journal Editor, a dedicated Scientific Managing Editor, a tool assisted recommendation, or a combination. For more details see the journal guide for authors.

At Elsevier, we want to help all our authors to stay safe when publishing. Please be aware of fraudulent messages requesting money in return for the publication of your paper. If you are publishing open access with Elsevier, bear in mind that we will never request payment before the paper has been accepted. We have prepared some guidelines (https://www.elsevier.com/connect/authors-update/seven-top-tips-on-stopping-apc-scams) that you may find helpful, including a short video on Identifying fake acceptance letters (https://www.youtube.com/watch?v=o5l8thD9XtE). Please remember that you can contact Elsevier s Researcher